

**APPLICATION OF PARALLEL IMAGING TO MURINE  
MAGNETIC RESONANCE IMAGING**

A Dissertation

by

CHIEH-WEI CHANG

Submitted to the Office of Graduate Studies of  
Texas A&M University  
in partial fulfillment of the requirements for the degree of

DOCTOR OF PHILOSOPHY

Approved by:

Chair of Committee,	Mary P. McDougall
Committee Members,	John C. Criscione
	Steven M. Wright
	Jim X. Ji
Head of Department,	Gerard L. Cote

December 2012

Major Subject: Biomedical Engineering

Copyright 2012 Chieh-Wei Chang

## ABSTRACT

The use of parallel imaging techniques for image acceleration is now common in clinical magnetic resonance imaging (MRI). There has been limited work, however, in translating the parallel imaging techniques to routine animal imaging. This dissertation describes foundational level work to enable parallel imaging of mice on a 4.7 Tesla/40 cm bore research scanner.

Reducing the size of the hardware setup associated with typical parallel imaging was an integral part of achieving the work, as animal scanners are typically small-bore systems. To that end, an array element design is described that inherently decouples from a homogenous transmit field, potentially allowing for elimination of typically necessary active detuning switches. The unbalanced feed of this “dual-plane pair” element also eliminates the need for baluns in this case. The use of the element design in a 10-channel adjustable array coil for mouse imaging is presented, styled as a human cardiac top-bottom half-rack design. The design and construction of the homogenous transmit birdcage coil used is also described, one of the necessary components to eliminating the active detuning networks on the array elements. In addition, the design of a compact, modular multi-channel isolation preamplifier board is described, removing the preamplifiers from the elements and saving space in the bore. Several additions/improvements to existing laboratory infrastructure needed for parallel imaging of live mice are also described, including readying an animal preparation area and developing the ability to maintain isoflurane anesthesia delivery during scanning. In

addition, the ability to trigger the MRI scanner to the ECG and respiratory signals from the mouse in order to achieve images free from physiological motion artifacts is described. The imaging results from the compact 10-channel mouse array coils are presented, and the challenges associated with the work are described, including difficulty achieving sample-loss dominance and signal-to-noise ratio (SNR) limitations. In conclusion, *in vivo* imaging of mice with cardiac and respiratory gating has been demonstrated. Compact array coils tailored for mice have been studied and potential future work and design improvements for our lab in this area are discussed.

## **DEDICATION**

To my father and mother  
Kuang-Chu Chang and Li-Chun Ho

## ACKNOWLEDGEMENTS

I gratefully thank my parents for their support and encouragement to pursue my Ph.D. degree. They endeavored to educate me in as good a way as possible and always reminded me to keep moving forward whenever I faced difficulties and obstacles. I would also like to thank my uncle, Dr. Gordon Chang, who inspired me to study in the United States, and especially at his beloved Texas A&M University.

I acknowledge the invaluable assistance and guidance my advisor, Dr. Mary McDougall, provided me with during my Ph.D. studies and research. She not only encouraged me to accomplish specific goals but also helped me solve problems. I learned research techniques from her and obtained a numerous of perspectives on my living experience, value of family, and life balancing, which enriched the word “advisor” to me. I also appreciate the time and support from all of my committee members, Dr. Steven Wright, Dr. Jim Ji, and Dr. John Criscione.

I would also like to thank all of my friends in College Station, especially my colleagues in MRSL. Their assistance and humor made my life amazing and happy during the years of my graduate study.

Finally, I want to thank Wendy for supporting me and our family during these years. I could not have achieved anything without her help and consideration. I also thank Wendy for bringing Vivian into our family. Vivian is the best thing ever happened in my life. Her naïve smile makes everyday my shining day and reminds me of the little boy inside of my heart.

## NOMENCLATURE

CV	Cardiovascular
RF	Radio Frequency
MRI	Magnetic Resonance Imaging
SEA	Single Echo Acquisition
LV	Left Ventricular
TVA	Tennessee Valley Authority
DPP	Dual-Plane Pair
PP	Plane Pair
SEMS	Spin Echo Sequence
SAR	Specific Absorption Rate
TR	Repetition Time
TE	Echo Time
FLASH	Fast Low-Angle Shot Sequence
EPI	Echo Planar Imaging
fMRI	Functional Magnetic Resonance Imaging
MRSL	Magnetic Resonance System Lab
SNR	Signal-to-Noise Ratio
ECG	Electrocardiography or EKG from German
FOV	Field Of View
VSWR	Voltage Standing Wave Ratio

T	Tesla
NEX	Number of Average
N <sub>pe</sub>	Phase Encoding Number
PILS	Partially Parallel Imaging with Localized Sensitivity
B <sub>1t</sub>	Transverse B <sub>1</sub> Field

## TABLE OF CONTENTS

	Page
ABSTRACT .....	ii
DEDICATION .....	iv
ACKNOWLEDGEMENTS .....	v
NOMENCLATURE .....	vi
TABLE OF CONTENTS .....	viii
LIST OF FIGURES .....	xi
LIST OF TABLES .....	xv
CHAPTER	
I INTRODUCTION .....	1
1.1 Challenges and Current State of Parallel Imaging of Mice .....	2
1.2 Dissertation Objectives .....	3
1.3 Dissertation Outline .....	4
II BACKGROUND .....	9
2.1 Basic MRI Theory .....	9
2.1.1. Main Magnetic Field $B_0$ .....	9
2.1.2. Voxel Imaging Size .....	9
2.1.3. Averaging .....	10
2.1.4. RF Array Coils .....	10
2.2 Parallel Imaging Technology .....	11
2.3 64-channel RF Arrays for SEA Imaging and Wide-Field-of-View Microscopy .....	13
III DEVELOPMENT OF PARALLEL MRI HARDWARE .....	15
3.1 Element Design for 64-Channel Planar Imaging .....	15
3.1.1 Introduction .....	15
3.1.2 Hardware and Instrumentation .....	19
3.1.3 Imaging and Reconstruction .....	21
3.1.4 Result and Discussion .....	23



3.2	RF Front-End Improvement for 64-Channel System .....	32
3.2.1	64-Channel Active T/R Switch .....	33
3.2.2	Experimentally Measuring the Switching Time .....	37
IV	DEVELOPMENT OF <i>In Vivo</i> SMALL ANIMAL MRI CAPABILITY .....	42
4.1	Introduction .....	42
4.2	Anesthesia Units .....	44
4.3	Gating System .....	46
4.4	Small Animal Holders .....	51
4.5	Standard Operation Procedure of Anesthesia and Gating Setting .....	52
V	TAILORING PARALLEL IMAGING METHODOLOGY AND HARDWARE FOR <i>In Vivo</i> MOUSE MRI .....	53
5.1	Introduction .....	53
5.2	Ten-Channel Array Coil Design .....	55
5.2.1	Advantages of Element Design for Compact-Volume Array Coil Construction .....	56
5.2.2	Array Construction and Configuration .....	59
5.3	Modular Low-Input Impedance Preamplifier Board .....	63
5.4	Transmit Coils .....	68
5.4.1	Homogenous Transmit-Only Linear Coil for Parallel Imaging ..	68
5.4.2	Description of Additional Volume Coils Constructed and Applications .....	71
5.5	Compact Mouse Coil System Integration .....	76
VI	INITIAL RESULT, CONCLUSION AND FUTURE WORK .....	78
6.1	<i>In vivo</i> Mouse Imaging with 35mm Volume Coil .....	78
6.2	Ten-Channel DPP Arrays with Volume Coil Imaging .....	87
6.3	Euthanized Mouse Imaging with Array .....	101
6.4	Limitations and Future Work .....	110
6.4.1	<i>In vivo</i> experiments .....	110
6.4.2	Element Design for Different Coil Length .....	110
6.4.3	Changing Distance between Signal Trace and Ground Leg of DPP Element .....	110
6.4.4	Tuning and Matching Network .....	112
6.4.5	Element Outsourcing for Better Stability .....	112
6.4.6	Better RF Connection on Preamplifier Board and Additional Functions .....	112
6.4.7	Better Actively Detuned of Linear Birdcage .....	113
6.5	Conclusion .....	113

REFERENCES .....	115
APPENDIX I .....	125
APPENDIX II.....	130

## LIST OF FIGURES

	Page
<p>Figure 2.1. Footprints of the original planar pair element and the RF current path. The bold arrows indicate the current path, and the circles show the location of the feed point. The planar pair coil design is shown in left picture. The current travels up the center conductor and returns along the two traces with half equal current.....</p>	14
<p>Figure 3.1. Illustrations of the planar pair element (a, left) and the dual-plane pair element (a, right) and simulated relative field sensitivity patterns of both elements (b). The dual-plane pair element has higher sensitivity than the planar pair due to the dropped traces for current return and thus decreased field cancellation that enables greater imaging depth. ....</p>	18
<p>Figure 3.2. (a) Front (imaging side) of the 64-channel dual-plane pair element array on a multi-layer board. The imaging side of the coil is free of all components and consists only of 64 signal (center conductor) traces. (b) Back (component side) of the 64-channel array. The geometric decoupling loops are fabricated at the end of the dual-plane pair element, opposite the feed point. A zoomed view of the decoupling loop is shown using circuit-board drawing software for clarity. The current path is denoted by yellow arrows. The center conductor of the dual-plane pair element on the top (imaging) layer is shown in red. It connects through a via to the bottom layer (shown in blue). At the end of the segment, the center conductor connects to the middle layer (shown in pink) through a via, and the coil is geometrically decoupled from its adjacent neighbors by overlap between the middle and bottom layers, spaced 0.012” apart. On the far right inset, the zoomed match and tune region is shown with, from top to bottom, the fixed capacitor for full-wave effect compensation, the varactor diode for tuning, and the tunable match capacitor. ....</p>	20
<p>Figure 3.3. Decoupling matrix indicated by measured S21 values [dB] for the 64-channel dual-plane pair element array. The average nearest neighbor coupling is measured as <math>S_{21} = 19.9\text{dB}</math>, and average next-nearest neighbor coupling is measured at <math>S_{21} = -25.7\text{dB}</math>. The “bulges” visible in the matrix are most likely explained by coupling within the four ribbon cables used to interface to the array.....</p>	24

Figure 3.4.	Single-channel images of both the dual plane pair (A) and planar pair (B), with plots of the relative field intensity at depths above the elements (C). At all sampled points, the raised leg has greater field intensity than the planar pair, enabling greater penetration into the phantom with sufficient sensitivity. ....	27
Figure 3.5.	Fully encoded transmit-receive reference image taken with the volume coil (left). The red rectangle outlines the zoomed region selected to demonstrate the relative capabilities of the planar pair and dual-plane pair element arrays. The sum-of-squares comparison images on the right show the dual-plane pair element to have a five-fold increase in SNR at depth over the planar pair element – equivalent to that of the volume coil. In addition, the wider and deeper sensitivity pattern of the dual-plane pair element improves the “striping artifact” seen when using the planar pair element close to the array. ....	29
Figure 3.6.	Single echo acquisition (SEA) images reconstructed retrospectively from the fully-encoded data sets from the planar pair and the dual-plane pair arrays. The dual-plane pair array enables SEA imaging at depths not previously possible. The array also shows significant improvements in SNR close to the coil due to an increase in the effective voxel size due to the wider and deeper sensitivity pattern – a fact which can adversely affect the achievable resolution, as described in the text. ....	30
Figure 3.7.	Diagram of active transmit-receive (T/R) switch. ....	34
Figure 3.8.	Photograph of 200 MHz active T/R Switch. The PCB board is sharing grounded with an RF shielding box that also common ground three connected ports with board and RF shielding. The port number also represents the S parameter channel number on bench measurement from network analyzer. ....	35
Figure 3.9.	S-parameter measurement of active T/R switch during transmit stage. ....	36
Figure 3.10.	S-parameter measurement of active T/R switch during receive stage. ....	37
Figure 3.11.	Switching time measurement configuration. ....	38
Figure 3.12.	Time of switching on at transmit stage. ....	39

Figure 3.13. Time of switching off at receive stage. ....	40
Figure 3.14. Configuration of RF front end components in 64 channel experiment setting. ....	41
Figure 4.1. Flowchart of anesthesia and gating system for 4.7T/40cm scanner at the MRSL .....	43
Figure 4.2. Small animal is initially knocked down here and mounted with sensors on the animal preparation table.....	45
Figure 4.3. MR-compatible units are located inside of the shielding room to support long-term anesthesia gas.....	45
Figure 4.4. Cardiac gating modules include of the respiratory, ECG/temperature, main control, and heater. ....	47
Figure 4.5. Small animal monitoring software with gradient on .....	48
Figure 4.6. Small animal monitoring software with gradient off .....	49
Figure 4.7. Baseline noise of ECG waveform with gradient on before fixing both ECG cables on holder. ....	50
Figure 4.8. Corrected baseline noise of ECG waveform with gradient on and ECG cables secured on holder.....	51
Figure 4.9. Small animal holder with sensors—(A) anesthesia gas inlet and outlet, (B) nose cone from 3D printer, (C) main body of animal holder with array coils, (D) animal cradle with ECG, temperature, and respiratory sensors, (E) warm-air tubing, and (F) adaptor plate to connect with rat-size birdcage. ....	52
Figure 5.1. DPP and loop element configuration—The left side is the loop structure and the right side is DPP element at both sides of the PCB.....	57
Figure 5.2. Position vs. normalized field strength plot across the DPP and loop element. (B) Coupling measurement between transmitting and receiving elements. Number 1 to 16 denotes the position of 16 rungs of transmitting birdcage coil. Radius distance represents the S21 coupling in dB. Blue represents the loop coil and red is DPP element. ....	58

Figure 5.3.	Array configuration with animal holder—(A) 1.5-inch OD animal holder with nose cone inside and warm air tubing connection at the back. The nose cone will be applied with the anesthesia units; (B) Top five-channel DPP arrays; (C) ATC 15-pF back-distributed capacitors for a homogeneous field pattern; (D) Matching network; (E) Warm-air tubing; (F) Semirigid coaxial cable to the preamplifiers; (G) Small animal cradle with respiratory, temperature, and ECG sensors; (H) Inlet and outlet for the anesthesia gas .....	60
Figure 5.4.	Decoupling matrix of 10 channel dual plane pair elements. The color bar indicates the S21 value as decibels. ....	62
Figure 5.5.	An compressible animal holder are designed and constructed to hold the arrays with squeezing mechanism that adapt animal tightly against RF coil. (A) The ring shape plates could allocate holders with array inside the birdcage with precise rotation angle. (B) Squeezing mechanism helps each element adapt diverse animal shape. (C) Four rods locks the moving mechanism after all to stabilize the coil with holder. ....	63
Figure 5.6.	16 channel modular preamplifier board supports low-input impedance preamplifiers to provide high impedance on the coil end as a decoupling method and amplify the MR signal to the receivers. The SNA connectors with semirigid coaxial cable connect the I/O of the low-input preamplifiers. The RF arrays could also be replaced quickly by means of the semirigid cable with specific electrical phase length. ....	65
Figure 5.7.	The decoupling value of low-input impedance preamplifier. The S31 drop from field strength of double pick up loop indicates the performance of preamplifier decoupling. ....	66
Figure 5.8.	The copper shielding of our linear transmit-only coil is removed to show the internal structure. The custom-made hexagonal former housed the 16-rung transmit trombone coil, including the frequency-tuning mechanism. The hexagonal former also served as the support of the copper shielding. The PETG tube (ID/OD: 2.438 in/2.5 in.; VisiPak, Arnold MO, USA) is installed inside of the transmit coil to prevent direct contact with specimens. The Nylon screw rod shown on the left side of the figure is used to tune the length of the rungs. The matching network shown on the right side of the figure is installed outside of the hexagonal form	

and at 90° to the main axis to reduce coupling to the receiving coil (not shown here). .....	69
Figure 5.9. The custom-made plug is made by two 1-in. long copper tubes, which are the same as the ones used for the mobile pipes of the transmit coil, one small piece laser-cut ¼-in.-thick acrylic sheet, and one 1.5 in. RG-58 cable. The openings of the two fixed copper tubes are mechanically treated to serve as the socket with a tight fitting. This design allowed us to quickly exchange different types of matching networks without sacrificing the transmit power. ....	71
Figure 5.10. Quad mode trombone birdcage for mice imaging. ....	72
Figure 5.11. The 60 mm quadrature mode birdcage for rat imaging applications. ....	74
Figure 5.12. A sagittal scan of a rat for brain slice planning. ....	75
Figure 5.13. A multi-slice diffusion weighted imaging set of a rat brain. ....	75
Figure 5.14. A sagittal and transverse imaging sheep brain from 23.5cm birdcage coil. ....	76
Figure 5.15. The image setting of compact RF arrays configuration with small-animal anesthesia and gating system. ....	77
Figure 5.16. The image setting of compact RF arrays system with volume coil, RF array coils, modular preamplifier board, balanced coaxial cable, biased-tee for actively detuned volume coil and flange plate shielding with multiple RF adaptors for scanner. ....	77
Figure 6.1. ECG gated in vivo imaging without respiratory gating in the abdominal region of the mouse. ....	80
Figure 6.2. Respiratory gated in vivo imaging without ECG gating in the cardiac region of mouse. Parameters are set for high resolution with thin slice thickness for fine cardiac structure with 1000/13.2 TR/TE, FOV 4x4 cm with matrix size 512x256, and slice thickness 0.3 mm with 2 mm imaging gap. ....	81
Figure 6.3. An ECG and respiratory gating image of cardiac region shows free motion artifact .....	81
Figure 6.4. A sagittal scan of a mouse for abdominal aorta slice planning .....	83

Figure 6.5. In vivo multislice spin echo imaging for abdominal aorta with cardiac gating. The red circle indicates the abdominal aorta and the yellow circle indicates the pump to release medicine gradually into the mouse. The imaging gap is 2 mm with a slice thickness of 0.8mm.....	84
Figure 6.6. Sagittal slice with cardiac gating to plane slice offsets. The red lines display the 1 cm imaging span to determine the abdominal aorta indicated by the blue arrow. ....	85
Figure 6.7. Abdominal aorta with 1000/13.2 ms TR/TE, NEX = 4, 0.5-mm slice thickness, 36 x 24- cm FOV with 512 x 256 matrix size (resolution 70 $\mu$ m x 94 $\mu$ m), 100,000-Hz spectral width, and 5.12 ms acquisition time. The red circle indicates the abdominal aorta region and the yellow circle represents the pump-inducing aneurysm inside the mouse. The slice offset by imaging number is 0, 2, 2.5, 4, 6, 7.5, and 1 mm, which directs scanning from the kidney toward the diaphragm. ....	86
Figure 6.8. A set of multislice spin-echo images along the coil length. The offset in the transverse direction is 1 cm span from the matching network toward long end of the coil. The imaging set indicates the coil profile along the frequency encoding direction.....	89
Figure 6.9. This image set represents the field pattern and localization of every coil as cylindrical arrays. ....	90
Figure 6.10. The birdcage images as reference indicate the higher SNR from the sum-of-square of 10-channel array imaging. The top row is the original images and SNR maps in bottom row show the same color bar level to display intensity difference among the imaging modalities. The corner number of each volume coil indicates average SNR at the center of images. The same number in array imaging presents maximum SNR value .....	92
Figure 6.11. This image set represents the field pattern and localization of every coil of the compressible array elements. ....	93
Figure 6.12. The birdcage images as reference indicate the higher SNR from the sum-of-square of 10-channel array imaging. The top row is the original images in gray scale and SNR maps in bottom row show the same color bar level with array image to display intensity difference among the imaging modalities.....	94



Figure 6.13. Gain of SNR map as cylindrical array and compressible array against mouse birdcage coil. ....	96
Figure 6.14. Original profile slice before applying normalization indicate the immense element variation between channels .....	96
Figure 6.15. The top DPP element indicated the yellow loop structure might induce transmit power and bottom DPP element represent the loop opened to avoid induced power. ....	98
Figure 6.16. Transmitting and receiving from birdcage with original DPP element inside. The images were obtained from spin-echo multislice imaging set with 1 cm slice offset in axial. ....	98
Figure 6.17. Transmitting and receiving from birdcage with DPP element inside as loop structure opened. These axial images were obtained from spin-echo multislice imaging set with 1 cm slice offset. ....	99
Figure 6.18. DPP element with loop structure indicated as yellow rectangular demonstrated the loop mode issue exaggerated from microarray into mouse element design. ....	100
Figure 6.19. Cylindrical 10-channel array imaging is obtained with 1000/30 TR/TE, 256 x 256 with 4 x 4cm FOV, and 2-mm thickness. ....	102
Figure 6.20. Compressible 10-channel array imaging profiles are obtained with 1000/30 TR/TE, 256 x 256 with 3 x 3cm FOV, and 2-mm thickness. ....	103
Figure 6.21. Left: Volume coil imaging with NEX = 3. Right: Reconstructed SOS imaging with NEX = 3. FOV = 3 x 3 cm with 26x256 points, 1000/30 msec TR/TE. ....	104
Figure 6.22. Single channel profile images of 10 DPP elements as compressible arrays from an euthanized mouse. Average number is eight. The ten profile indicate the sensitivity benefits of euthanized mouse from array element. ....	105
Figure 6.23. Comparison of the transmit volume coil image and the sum-of-square image from the array. The intensity of the sum-of-square image was normalized to the intensity of the volume coil image for visualization. ....	107

Figure 6.24	Illustration of indirect method to obtain the map of SNR gain between compressible arrays reconstructed image and quad mode mouse birdcage image. ....	108
Figure 6.25.	The map of SNR gain offered by the array coil as compared to a 35 mm quad mode birdcage mouse coil. Sum-of-squares reconstruction was used with NEX = 1, 2, 4, 8 for the array and compared to NEX = 8 with the mouse coil. ....	109
Figure 6.26.	Quasi-static simulation on different thickness of DPP element. ....	111

## LIST OF TABLES

	Page
Table 5.1 Decoupling value of every element from low-input impedance preamplifier. Each value is S parameter measurement from network analyzer and the unit is decibel [dB]. .....	67
Table 5.2 Decoupling S21 parameters between linear birdcage and 10 channel arrays.....	68
Table 5.3 SNR comparison between in house rat birdcages and commercial Varian coil. ....	73

# CHAPTER I

## INTRODUCTION

Genetically engineered (transgenic and knockout) mice offer a tremendous tool to medical research [1, 2], with the accompanying need to access *in vivo* information concerning the animals – a task typically accomplished with imaging techniques in humans that remains challenging in mice. The issues will be described here in the context of the particularly challenging task of imaging the cardiovascular (CV) system of the small animal – an area which benefits largely from the use of parallel imaging techniques for acceleration and resolution and is therefore particularly relevant to motivating the work described.

Magnetic resonance imaging (MRI) has established itself as a valuable tool to quantify both the structure and function in human CV research [3-7]. However, *in vivo* MRI of mice in cardiovascular applications has remained challenging as a practical tool, requiring enormous technical resources, primarily because mice have dramatically faster-than-human heart rates and smaller-than-human dimensions. Parallel imaging techniques (using multiple receivers and sensors) in MRI provides the capability to reduce scan time based on the partial or entire removal of phase-encoding steps [8], offering a natural benefit to cardiovascular magnetic resonance imaging (CV-MRI) of the murine model. Our research group invented single echo acquisition (SEA) MR imaging, based on massively parallel (64 channel) sensor and receiver technology[8]. The unique design of the sensor allows for imaging with either extremely high temporal

resolution and low spatial resolution (“fast mode”) or with high spatial resolution and lower temporal resolution (“hi-res mode”) [9], and this work represents our initial efforts to translate this capability to the mouse model. *This work describes the development of the foundational level tools to be able to apply the benefits of parallel imaging to high spatial and temporal resolution acquisitions in MR imaging of the murine system.*

### **1.1 Challenges and Current State of Parallel Imaging of Mice**

Applying the advances offered to humans by parallel imaging to CV-MRI applications in mice is challenging, given their vastly smaller dimensions and higher heart rates. Specifically, the LV inner chamber diameter of a mouse is approximately 3.1 mm, and the carotid artery diameter is approximately 0.5 mm (compared to a human, who has an average systolic inside diameter of 8.6 mm). The heart rate of the mouse is 450 to 600 beats/min (as compared to the average adult human heart rate of 60 to 80 beats/min). That said, several groups routinely image the CV system of the mouse [10-12], and a move toward parallel imaging is beginning to be reported. The time required for a standard cardiac-gated MRI of a rat generally requires 30 to 40 minutes, while an MRI of a mouse takes on the order of hours [13]. Several groups have applied parallel imaging technology to mice and small rodent imaging, although not necessarily targeted at the CV system. Schneider et al. reported a four-channel phased array design for cardiac imaging of mice at 9.4 T [14]. Eight-channel volumetric coils, designed for renal imaging, have been used to obtain an acceleration factor of four [15]. Keil

developed a 20-channel phased array body coil for mouse imaging at 3T [16]. Bankson's group developed a three-element phase-array coil at 7T for high-resolution MRI of both thoracic and cervical segments of a rat's spinal cord, achieving acceleration factors of two and three [17]. The group also developed a dual-mouse system with a pair of two-element phased-array coils, which can simultaneously scan two mice and achieve a three-fold acceleration [18]. The following section outlines the description of this work towards achieving routine parallel imaging of live mice in our lab.

## **1.2 Dissertation Objectives**

The early stages of my research focused on RF array element design to improve SNR, imaging depth, and artifacts for highly parallel imaging and microscopy. The extension and application of the designs to mouse imaging followed. The specific objectives of the work are described below:

**Objective 1—Develop parallel MRI hardware capable of traversing spatio-temporal resolution extremes**

**Objective 2—Develop *in vivo* small animal MRI capability**

**Objective 3— Tailor parallel imaging methodology and hardware for *in vivo* MRI of mice**

### **1.3 Dissertation Outline**

#### CHAPTER I - INTRODUCTION

The importance, requirements, and challenges of acquiring MR images of the laboratory mouse were addressed in this chapter. This was done in the context of discussing imaging of the murine cardiovascular system and the motivation to use parallel imaging techniques. Finally, this chapter outlines the aims and goals of this research.

#### CHAPTER II - BACKGROUND

An overview of phased array MRI technology is introduced as used to overcome the limitations of gradient based methods for accelerating the imaging speed. Previous 64-channel work in the Magnetic Resonance System Lab at Texas A&M University is described to demonstrate the potential power obtained by using parallel imaging.

#### CHAPTER III – DEVELOPMENT OF PARALLEL MRI HARDWARE

The development of hardware to permit imaging at the “extreme” of parallel imaging is described. These 64 channel planar array coils and RF front end additions were not specifically tailored for use with mice, but provided two building blocks: 1) the investigation of a microcoil array element design of potential benefit to mouse arrays and 2) RF front end work that aided in the effort to perform highly parallel transmit-

receive imaging, which our group has shown is necessary to image at the extremes of acceleration on a curved surface (as would be necessary to image mice)

a. *64-channel planar array coils with improved imaging depth*

An element design named a “dual-plane pair” is described. The element was used in 64-channel array coils designed to demonstrate the ability to view the full range of spatio-temporal data. These receive-only array elements were required to be decoupled from one another so as to not require isolation preamplifiers, as our existing 64-channel channel system uses 50Ω preamplifiers. In addition, 64-channel transmit/receive coils were built for use with the 64-channel transmit system recently built in-house[19].

b. *RF front-end improvements for the 64-channel receiver system*

64-channel T/R switches and low-noise 50Ω preamplifiers were built for use with the 64-channel transmit-receive system[20].

#### CHAPTER IV – DEVELOPMENT OF *In Vivo* SMALL ANIMAL MRI CAPABILITY

To apply the benefits of parallel imaging to *in vivo* mouse imaging, we needed the capability to quickly anesthetize the animal, load and position it in the RF coil and in the scanner, maintain anesthesia during the lengthy scan, and communicate the physiological signals from the mouse to the scanner for gating purposes. The development of these capabilities is discussed in CHAPTER IV.

a. *Anesthesia units*



Multiple isoﬂurane evaporators and an air/gas flow systems are incorporated into the animal tables and MR-compatible carts to allow for knocking out the animals and maintaining anesthesia in the scanner. This setup takes into account the high-magnetic fields with small bore scanner and need for repeatable procedures.

b. *Cardiac gating units*

A respiratory and electrocardiogram (ECG) gating system from Small Animal Instruments was incorporated with the 4.7T/40-cm scanner supported by a Varian Inova console. This arrangement allowed for triggering the MR scanner with the cardiac and respiratory cycles of the animal and monitoring the animal's physiological signals in the magnet (temperature and heart rate).

c. *Animal holder*

A small animal holder was designed and built for easy loading and accommodating mice in the 4.7T/40-cm horizontal magnet with ECG/respiratory sensors, the anesthesia delivery and gas scavenging.

## CHAPTER V – TAILORING PARALLEL IMAGING METHODOLOGY AND HARDWARE FOR *In Vivo* MOUSE MRI

The 64 channel planar array coils described in CHAPTER III were not tailored for mice due to their element size and form factor, but instead for traversing the extremes of spatio-temporal resolution capabilities with parallel imaging. This chapter describes increasing the element size to image deeper into the mouse, the adjustable

form factor used to fit to the mouse's body, and the implications of those two changes with respect to coupling, channel count, associated hardware etc.

a. *Array coil design and construction*

Dual-plane pair (DPP) and loop elements were investigated with respect to their benefits for parallel imaging in the form factor for mice. Previous experience with the DPP element and ease of implementation lead to that element being the element of choice for initial array work for mice. The construction of 10 channel array coils to perform mouse imaging with low-input impedance preamplifiers for isolation is described.

b. *Modular 16-channel isolating preamplifiers board*

Isolation preamplifiers allow for freedom in array coil design, removing to a large extent concerns regarding element-to-element coupling and suppress the induced current on different type of element design. While isolation preamplifiers are usually "hard wired" to the array elements, this design is modular and capable of being used with any array coil to facilitate investigation of various configurations in the future.

c. *Volume coil transmission with active decoupling*

Quadrature transmit volume coils in various sizes are described, all are actively decoupled to allow for freedom in the receive-only array coil geometries.

d. *Compact mouse coil system integration*

The integration of the RF arrays, volume coil, preamplifiers, and anesthesia is described.

## CHAPTER VI – INITIAL RESULTS, CONCLUSION, AND FUTURE WORK

\*\*\*\*\*The results are summarized and discussed in this chapter to demonstrate the  
equipment"of this work and future work is discussed.

- a. In vivo Mouse Imaging with 35mm Volume Coil*
- b. Phantom Imaging with Array*
- c. Euthanized Mouse Imaging with Array*
- d. Limitations and Future Work*
- e. Conclusions*

## **CHAPTER II**

### **BACKGROUND**

#### **2.1 Basic MRI Theory**

Before introducing the work and results of this research, several basic principles of MRI will be explained in this chapter as applied to the imaging theory and tradeoffs between imaging parameters. There are several parameters that affect the SNR, imaging speed, and resolution of the imaging.

##### **2.1.1. Main Magnetic Field $B_0$**

Generally, the main magnetic field strength is proportional to the signal level. The SNR can be improved by scanning at high-field strength MRI; however, the high cost of a superconductive magnet and other issues such as longer T1 relaxation time, RF penetration depth with shorter wavelength, specific absorption rate (SAR) limitation, and chemical shift effects should be well thought-out within the strategy plans when considering the higher field strength for SNR. High field scanners generally have smaller bore size which make space-demanding critical for small animal hardware design.

##### **2.1.2. Voxel Imaging Size**

The larger imaging voxel size contributes to a higher SNR. There are more hydrogen protons inside the larger voxel and that generates a stronger resonant MR signal. Consequently, the 3D voxel size is determined by slice thickness and in-plane matrix size or imaging resolution. The larger the slice thickness is, the higher the SNR.

Also, the higher the resolution is, the lower the SNR. If we scan the image with resolution down from 256 x 256 to 128 x 128 with same slice thickness, the SNR is supposed to decrease by a factor of four if other parameters are remained same. Based on this MRI principle, the SNR issue is critical at microscopy imaging levels when the resolution is being pushed beyond its limit. Another approach generally applied to compensate for SNR loss in high resolution situation is increasing the averaging number.

### **2.1.3. Averaging**

Averaging MR scans leads to higher SNR: although the signal intensity adds coherently by averaging, the noise level is uncorrelated and adds as the root mean square. Therefore the SNR improves as the square root of number of scans. For example, the SNR doubles in value when averaging four times. The averaging technique is commonly used in MRI to boost the SNR level. However, the time-consuming scanning leads to other issues such as efficiency, cost, or even motion artifacts in long-term *in vivo* imaging.

### **2.1.4. RF Array Coils**

By using multichannel RF array coils to obtain images, the sensitivity can be improved or equaled as compared to single element with same size covering same region of interest (assuming sample loss dominance) and the improvement in SNR can be exploited to reduce scan times (accelerating imaging) and/or to achieve improved resolution.

## 2.2 Parallel Imaging Technology

Conventional MRI is time consuming; achieving spatial resolution in the phase encoding direction requires multiple iterations of the pulse sequence. The number of pulse sequence iterations is equal to the number of phase encoding points, typically 128 or 256. The repetition time (TR) defines the time required for each phase encoding step. The repetition time (TR) is longer than the echo time (TE), allowing for the net transverse magnetization to decay toward equilibrium for each iteration. Signal acquisition for the frequency encoding direction is accomplished by sampling throughout the acquisition window, which is generally 1 to 20 milliseconds. Thus, the scan time is mostly determined by number of averages (NEX), repetition time (TR) and phase encoding points ( $N_{pe}$ ).

The scan time is equal to the number of scanning average ( $nt$ ) x phase encoding number ( $N_{pe}$ ) x repetition time (TR). There are several simple and straightforward methods to reduce TR and therefore reduce scan time. For example, the FLASH imaging sequence applies the lower tip angle and spoiled gradient to destroy any residual magnetization on the transverse x-y plane after each echo [21]. By doing so, the shorter TR values in the milliseconds range could relieve the need for long scanning times in the magnet for the patient. However, there are still some tradeoffs such as simply using FLASH imaging, which is very sensitive to static magnetic fields. The homogeneous  $B_0$  field is required to obtain high-quality FLASH imaging by the fine shimming technique.

Instead of repeating TR, Peter Mansfield suggested a fast switching gradient method called echo planar imaging (EPI) to rapidly repeat the reverse frequency encoding gradient that eliminates TR [22, 23]. The phase encoding gradient could be turned on continuously at low levels or blipped to stack up one line to fill up the k-space immediately after a single 90- and 180-degree excitation pulse. The famous EPI is widely used in diverse imaging applications such as diffusion imaging [24-26], perfusion imaging [27, 28], cardiac imaging [5, 29], and functional MRI [30-35]. Sir Peter Mansfield who invented EPI has also been honored by being a recipient of the Nobel Prize in physiology or medicine at 2003. EPI has shown the feasibility of using fast MRI in diverse applications. However, EPI requires a very strong gradient magnitudes and fast switching gradient rates to obtain the echo before the T2 effect decay signal. This can induce eddy currents and also requires stabilization of the gradient coil and reduced vibrations. Fast gradient switch times can also lead to peripheral nerve stimulation, a very real clinical concern[36]. Primarily, further decreasing imaging speed by switching gradients faster is limited from the standpoint of hardware development.

“Parallel imaging” refers to using multichannel receivers and RF array coils to share the burden filling the k-space matrix and reducing phase encoding steps. Insufficient sampling of k-space lines could lead to aliasing of imaging but the missing k-space lines can be compensated by the data from multichannel RF array coils in reconstruction. Hyde et al. reported quadrature detection using surface coils with a hybrid combiner in 1987 [37] for multi-channel array detection. Hutchinson et al. also proposed fast MRI data acquisition using multiple detectors in 1988 [38]. Wright et al.

submitted the theory and application in 1987 for using multiple decoupled arrays for spine imaging reconstruction [39, 40]. Roemer et al. demonstrated compact classic and straightforward methods to decouple arrays and obtain MRI data for reconstructed spine imaging from arrays [41]. Based on the parallel imaging contributions from these pioneers in the late 1980s, multichannel receivers and RF array coils have been designed and constructed for all types of applications in MR imaging.

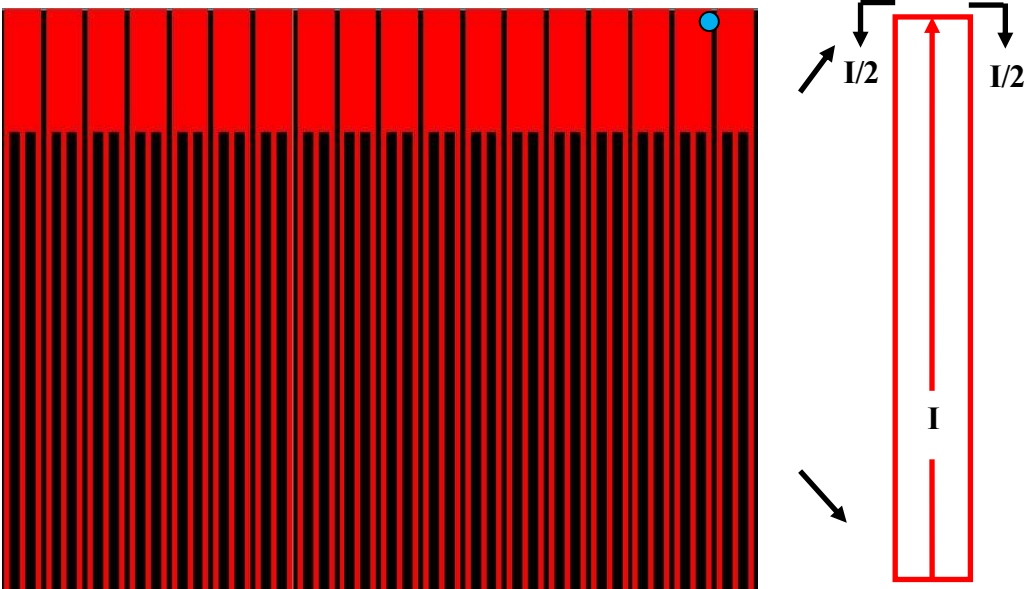
For instance, Schmitt et al. has implemented 128 channel arrays (in the research arena) for human cardiac imaging at 3 Tesla [42]. Hardy et al. also demonstrated full body MRI with 128-channel high density receive coil arrays[43]. Wiggins et al. presented a 96-channel receive-only head coil for clinical MRI at 3 Tesla[44]. 32-channel human cardiac arrays for 1.5 Tesla and head arrays for 3T clinical scanning have also been presented [45, 46]. Parallel imaging has also substantially benefited non-cardiac clinical applications, including perfusion and diffusion imaging as well as functional MRI [25, 47, 48].

### **2.3 64-channel RF Arrays for SEA Imaging and Wide-Field-of-View Microscopy**

The TAMU group was the first to introduce a “massively parallel” system using 64 receiver channels[49]. The 64-channel planar arrays used could operate in either an extremely fast mode for acquiring images in a single echo or high resolution imaging over a large field of view with fully encoded k-space collection from each coil[50]. This work in parallel imaging that entirely removed the need of changing the phase encoding



gradient was called Single Echo Acquisition (SEA) imaging[8]. Both SEA imaging and wide-field-of-view microscopy demonstrated the potential to use parallel imaging technology to expand to even more diverse applications [51]. The planar pair element design rather than common loop coil for 64-channel arrays is displayed in Figure 2.1, both functionally and in its array environment. Extending this massively accelerated capability to deeper imaging depths by the development of a new element design, the use of that element design for mouse imaging, and the extension of the 64-channel hardware to have the capability to image on a curved surface as would be needed for mice will be described in the following chapters.



**Figure 2.1.** Footprints of the original planar pair element and the RF current path. The bold arrows indicate the current path, and the circles show the location of the feed point. The planar pair coil design is shown in left picture. The current travels up the center conductor and returns along the two traces with half equal current.

## CHAPTER III

### DEVELOPMENT OF PARALLEL MRI HARDWARE\*

The development of hardware to permit imaging at the “extreme” of parallel imaging is described in this chapter. These 64 channel planar array coils and RF front end additions were not specifically tailored for use with mice, but provided two building blocks: 1) the investigation of a microcoil array element design of potential benefit to mouse arrays and 2) RF front end work that aided in the effort to perform highly parallel transmit-receive imaging, which our group has shown is necessary to image at the extremes of acceleration on a curved surface [52, 53](as will be necessary to apply to mice).

#### 3.1 Element Design for 64-Channel Planar Imaging

The dual-plane pair element described below was eventually the element chosen to construct the prototype mouse array coils. The following sections describe the element in the context of its contribution to highly accelerated planar imaging, originally presented in the following manuscript [54].

##### 3.1.1 Introduction

---

\* Part of the data reported in this chapter is reprinted with permission from “An Improved Element Design for 64-Channel Planar Imaging” by Chieh-Wei Chang, 2011. *Concepts in Magnetic Resonance Part B*, 39B, p159-165, Copyright [2011] by John Wiley & Sons.

Some of the earliest visions of accelerated MRI proposed parallelization to a high enough degree to allow for the complete elimination of phase encoding [38, 55, 56]. Fittingly, the investigation of increased channel counts has progressed in recent years far beyond what is considered “standard” in the clinic, with Sodickson even coining the term “massively parallel” [57]. *In vivo* implementations of parallel imaging with 32 channels [46], 96 channels [44], and 128 channels [42, 43] even suggest the possibility of the eventual translation of massively parallel reception into certain more standard clinical applications.

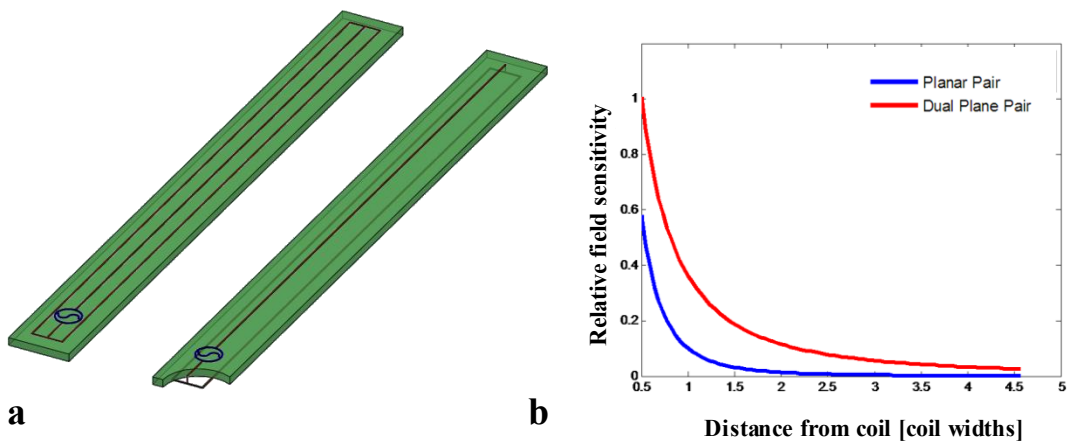
Our research group has maximized acceleration in one dimension, acquiring a complete  $64 \times N_{\text{Readout}}$  image in a single echo [58, 59], using a 64 channel receiver [49] and a 64-channel array of long and narrow planar pair elements [8]. The highly localized field patterns from the 64 planar pair elements are entirely responsible for providing the localization in one dimension, eliminating the need for phase encoding in a manner reminiscent of the earliest concept work. This imaging technique is called Single Echo Acquisition (SEA) imaging, and has been applied to image flow [60], tag tracking [61], motion [62], and 2D RF pulse formation at up to 1000 frames per second [63]. SEA imaging as currently reported, however, is a low resolution technique with shallow imaging depth – both on the order of millimeters – and it is desirable to investigate methods for improving both. Improved resolution can be achieved in a straightforward manner at the expense of imaging time by acquiring more than a single echo from each element, and phase encoding even to the point that the planar pair array is used as an array of microcoils to accelerate microscopy imaging using PILS-like reconstruction

methods [64-66]. Increasing imaging depth is less a methodological issue, instead requiring a modification to the array element itself. The constrained sensitivity pattern of the original element adequately accommodates the needs of SEA imaging well, providing the “resolution” of the image in what would be the phase encoding direction, but suffering from a concomitant limited imaging depth. A 64-element planar array constructed within the same 8 x 13cm total footprint as the original SEA array, still enabling full acceleration in one dimension, but with an element design modified to increase the imaging depth, is described in this chapter. This is accomplished by lowering the outer conducting legs of the planar pair with respect to the center conductor and adding a geometric decoupling configuration away from the imaging field of view. The element has been called a dual-plane pair in that the current carrying rungs in the imaging FOV function exactly as the planar pair, but are simply placed in two separate planes (sides of the printed circuit board (PCB) in this case).

### **3.1.2 Hardware and Instrumentation**

The primary objective of the new element design is to achieve a substantial increase in SNR at depth (distance from the surface of the planar array coil) greater than the currently used planar pair element capability in addition to maintaining the original 2mm x 8cm element footprint that afforded the highly localized imaging patterns necessary for SEA and PILS-like acceleration and reconstruction. To achieve objectives, the current return paths (two outer legs of the planar pair) are fabricated on the back side of 0.062" FR-4 laminate PC board, reducing the field canceling interactions with the

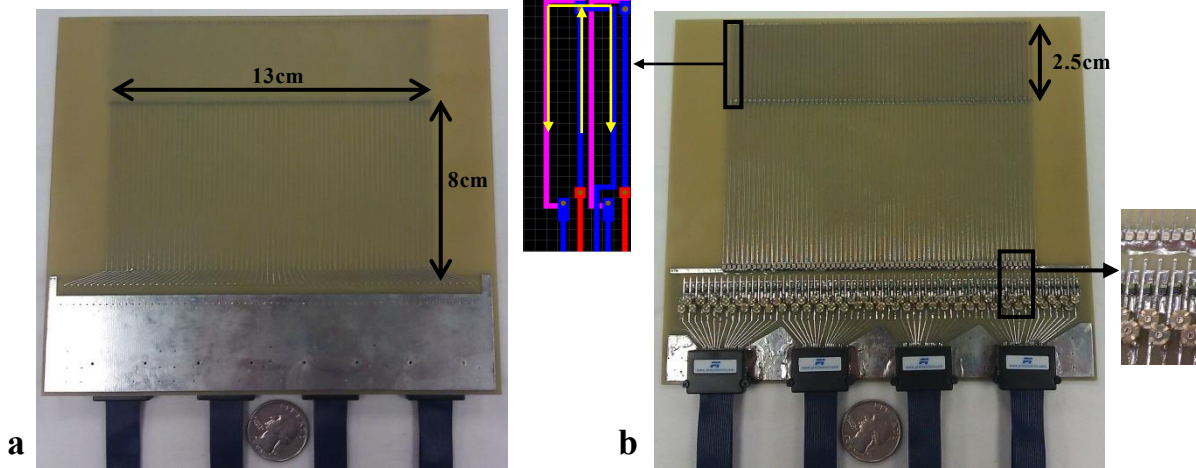
center current carrying conductor. For clarity, Figure. 3.1 shows the planar pair element and the dual-plane pair element diagrams, with their expected relative field sensitivity patterns as predicted by quasi-static modeling.



**Figure 3.1** Illustrations of the planar pair element (**a, left**) and the dual-plane pair element (**a, right**) and simulated relative field sensitivity patterns of both elements (**b**). The dual-plane pair element has higher sensitivity than the planar pair due to the dropped traces for current return and thus decreased field cancellation that enables greater imaging depth.

Each element of the 64-channel dual-plane pair array is matched and tuned at the coil by using a nonmagnetic single-sided varactor diode (BB639; Infineon, Milpitas California USA) for tuning and a variable capacitor (9702-1; Johanson Manufacturing Corporation, Boonton NJ USA ) for matching. The use of varactor diodes for tuning provides very small component packaging in a space-limited situation, and also provides the ability to tune the 64 coils somewhat “in bulk” by controlling the main biasing

voltage. The coils are biased over the RF lines by adding a 10K  $\Omega$  resistor in parallel with the matching capacitor to prevent it from acting as a DC block. Four ultrasound cables, each containing twenty 50 $\Omega$  coaxial lines (Precision Interconnect “Blue Ribbon,” Wilsonville, OR, USA), are used to connect the coil to two 32-channel “digital tuning boards” built in house [53]. The boards allow for individual control of the bias voltage on each line by using digital potentiometers (AD7376; Analog Devices, Inc., Norwood MA USA) with 7-bits of resolution on each channel and a USB interface managed by a National Instruments USB digital Input-Output (I/O) board (USB-6501; National Instruments Corporation., Austin TX USA). The ribbon cables are preassembled with low-profile header connectors, and matching surface-mount receptacles (QSE/QTE series; Samtec, Inc., New Albany IN USA) are installed on the array and digital tuning boards. A single 15pF fixed capacitor (A series; American Technical Ceramics, Huntington Station NY USA), is used at the feed end of each element to increase the homogeneity over the length of the element, with the optimal capacitor value and position on the element determined by using a full-wave modeling program developed in-house.



**Figure 3.2** (a) Front (imaging side) of the 64-channel dual-plane pair element array on a multi-layer board. The imaging side of the coil is free of all components and consists only of 64 signal (center conductor) traces. (b) Back (component side) of the 64-channel array. The geometric decoupling loops are fabricated at the end of the dual-plane pair element, opposite the feed point. A zoomed view of the decoupling loop is shown using circuit-board drawing software for clarity. The current path is denoted by yellow arrows. The center conductor of the dual-plane pair element on the top (imaging) layer is shown in red. It connects through a via to the bottom layer (shown in blue). At the end of the segment, the center conductor connects to the middle layer (shown in pink) through a via, and the coil is geometrically decoupled from its adjacent neighbors by overlap between the middle and bottom layers, spaced 0.012" apart. On the far right inset, the zoomed match and tune region is shown with, from top to bottom, the fixed capacitor for full-wave effect compensation, the varactor diode for tuning, and the tunable match capacitor.

With the increased sensitivity of the dual-plane pair came the need for a coil-to-coil decoupling mechanism that is unnecessary when using planar pair elements. In order to maintain the localization of the sensitivity patterns over each element, geometric decoupling is achieved through adding an overlapping region between coils at the end of the elements only, outside of the (8cm long) imaging region. Overlapping the conductors located on two different sides of the PCB required a design implementation using three layer PCB fabrication in order to maintain straightforward, repeatable, and reliable

production of the 64 elements. Fabrication of the board is outsourced to PCBexpress, (E4 4- layers; PCBexpress/Sunstone Circuits., Mulino OR USA, [www.pcbexpress.com](http://www.pcbexpress.com)), using the first (top), third, and fourth (bottom) layers of a standard four-layer FR-4 board with a separation distance between layers of 0.012". A photograph of the front and back of the populated coil and, more efficaciously, the PCB layout detailing the decoupling overlap is shown in Figure. 3.2. As detailed in the Figure 3.2., the current paths are connected through vias on the multi-layered board that allow for geometric decoupling between adjacent coils. Coupling is evaluated by collecting the upper diagonal half of the 64x64 matrix of  $S_{21}$  values using an Agilent E5071 Network Analyzer and the full matrix is filled based on reciprocity/symmetry theory.

### **3.1.3 Imaging and Reconstruction**

The 64-channel dual-plane pair array is used to acquire fully encoded high spatial resolution images, with retrospectively reconstructed SEA images, and the results are compared to the original 64-channel planar pair array performance. All imaging is performed in a 4.7 T/33cm magnet supported by a Varian Unity Inova console. The system is modified by interfacing a 64 channel receiver constructed in-house and described elsewhere [67]. Since adequate element-to-element decoupling, the 50 ohm low noise preamplifiers were chosen rather than the low-input impedance preamplifiers. Sixty-four conventional 50 $\Omega$  preamplifiers are used, constructed using commercial monolithic RF amplifiers (Model Gali-74+; Mini-Circuits., Brooklyn NY USA). The array coil is placed inside a volume coil for transmitting, consisting of two parallel plates

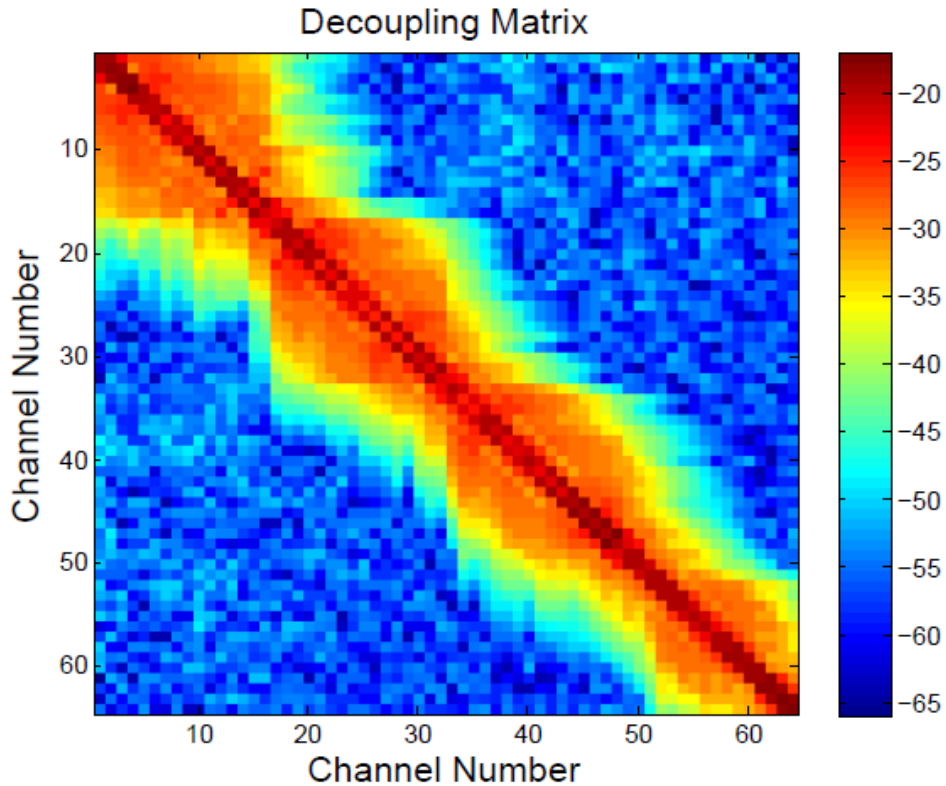


shorted at one end and impedance matched at the other end. The volume coil and array are placed on an acrylic positioning former with a flush fit to the magnet bore to eliminate variations in height when switching between the planar pair array and the dual-plane pair array. A resolution phantom built in-house is used for all 64-channel experiments. Fully encoded images are acquired from each channel simultaneously with the following imaging parameters: TR/TE=500/35ms, FOV=13×13cm,  $N_{phase\ enc} \times N_{readout} = 512 \times 1024$ , rendering a total acquisition time of 4.26 minutes with a spatial resolution of 254×126 microns. Coronal images with a slice thickness of 1.5mm are taken (in the plane parallel to the plane of the arrays) at distances of 0.5 coil widths (1mm) and 3 coil widths (6mm) away from the array, and compared quantitatively with regard to SNR. The images are reconstructed using a sum-of-squares method, with the highly localized individual coil images (2mm wide coil in a 13cm wide FOV) initially masked at six times their width before the sum-of-squares operation, at least partially indicative of the potential ability to perform accelerated higher resolution imaging with the array.

SEA images were created retrospectively from a single k-space line per coil as an evaluative process regarding imaging at the extreme of temporal resolution with the coil, not as a true exercise in the acquisition of accelerated images. Therefore, the effective SEA image acquisition time is TR (500 milliseconds), with TE=35ms, FOV=13×13cm, and  $N_{phase\ enc} \times N_{readout} = 1 \times 1024$  (for each of the 64 coils). SEA image reconstruction is performed by “stacking” the 1D Inverse Fourier Transformation of the single 1024 point echo from each coil into a 64 x 1024 matrix. The imaging processing code had been accomplished and demonstrated via Matlab code[8].

### 3.1.4 Result and Discussion

The  $64 \times 64$  matrix of S21 values between the elements of the geometrically decoupled dual-plane pair array is shown in Figure. 3.3. The average nearest neighbor S21 value is -19.9 dB, with maximum decoupling of S21 = -23 dB and minimum of S21 = -17 dB. The average decoupling between next nearest neighbors is measured as S21 = -25.7 dB, with maximum decoupling of S21 = -30.4 dB and minimum of S21 = -22.5 dB. The variability that exists in the measurements despite the repeatable PCB fabrication can likely be explained by coupling within the four blue ribbon cables, the effect of which is evident in the four “bulges” in the S21 matrix shown in Figure. 3.3. The coupling between the ribbon cables could also be reduced by attaching clipping-on baluns to eliminate the induced RF current on the cables.



**Figure 3.3** Decoupling matrix indicated by measured  $S_{21}$  values [dB] for the 64-channel dual-plane pair element array. The average nearest neighbor coupling is measured as  $S_{21} = 19.9\text{dB}$ , and average next-nearest neighbor coupling is measured at  $S_{21}=-25.7\text{dB}$ . The “bulges” visible in the matrix are most likely explained by coupling within the four ribbon cables used to interface to the array.

The decoupling achieved with the overlapped region is not without cost in this case. The elements are copper loss dominated by their “microcoil” nature. Therefore, it must be noted that the addition of a geometric decoupling region approximately half the length of the imaging region undoubtedly incurred significant losses; however, the ability to easily fabricate repeatable coil-to-coil decoupling and achieve such significant improvements in imaging depth made the added loss (at least for the time being) insignificant compared to the benefit. An analysis of the degree of degradation in SNR induced by the geometric decoupling network is presented below:

The coil signal-to-noise ratio (SNR) can be expressed by the following equation:

$$SNR_C = \frac{|V_{signal}|}{V_{noise}} = \frac{\sqrt{2}w_0\Delta VM_{xy}|B_{1t}|}{\sqrt{4kT\Delta fR_{coil}}}$$

If we assume the same temperature, voxel size, frequency span, center frequency of coil and tip down magnetization, we could remove the constant terms for comparison. The formula becomes as follows[41]:

$$SNR_C = \frac{|V_{signal}|}{V_{noise}} = \frac{|B_{1t}|}{\sqrt{R_{coil}}}$$

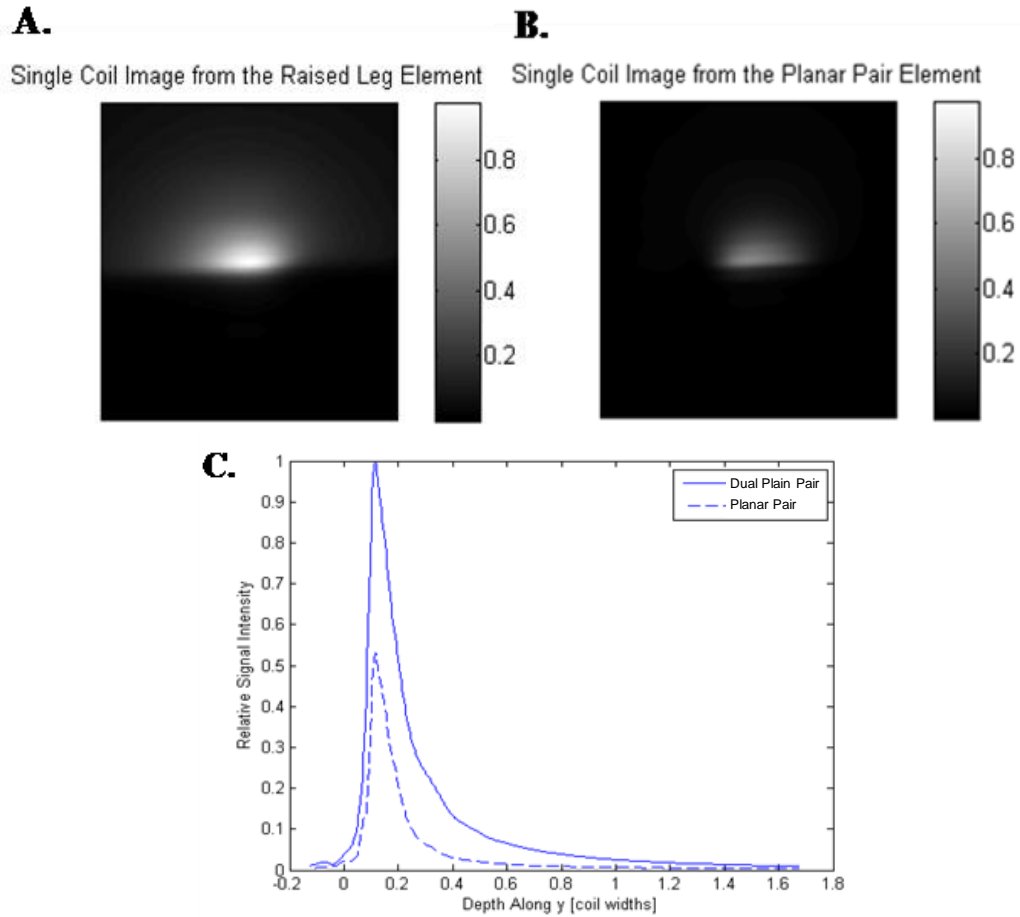
Thus, the evaluation of two different coils could be expressed based on transverse flux density and resistance of the coil. For example, we can obtain the flux magnitude at a given height from the coil from the quasi-static simulation result shown in Figure 3.1(b). For instance, the magnitude of the  $B_1$  field from the planar pair element is 0.1 and is 0.39 from the dual plane pair element at one coil width height. Because the decoupling loop length is 31.25% of the signal trace, the resistance ratio should be proportional to the length. The dielectric constant, trace width, trace height and subtract height are all same in this situation. Only the length of decoupling loop are added and extended 31.25% more.

$$\frac{SNR_{Planar\ pair}}{SNR_{Dual\ Plane\ Pair}} = \frac{|B_{1t\_PP}| \sqrt{R_{Dual\ Plane\ pair}}}{\sqrt{R_{Planar\ pair}} |B_{1t\_DPP}|} = \frac{0.1 \times \sqrt{1.3125}}{\sqrt{1} \times 0.39} = 0.29$$

The SNR of the planar pair element is only 29% of the dual plane pair element. Therefore, the loss resulting from adding geometric decoupling to the DPP element is justified by the overall improvement in SNR at depth.

The unloaded/loaded Q value of the DPP element is 68.804/64.612 which is equal to 1.065. The Q value ratio of unloaded/loaded on the PP element is 73.366/71.908 which is equal to 1.02. We can see that the Q value ratio of both elements indicates copper loss dominance, though the Q value ratio of the DPP element is slightly higher, indicating that the DPP coil loads more to the sample than the planar pair element. All of the Q values are obtained by VSWR measurements with a 2:1 bandwidth as measured by the Agilent Network Analyzer.

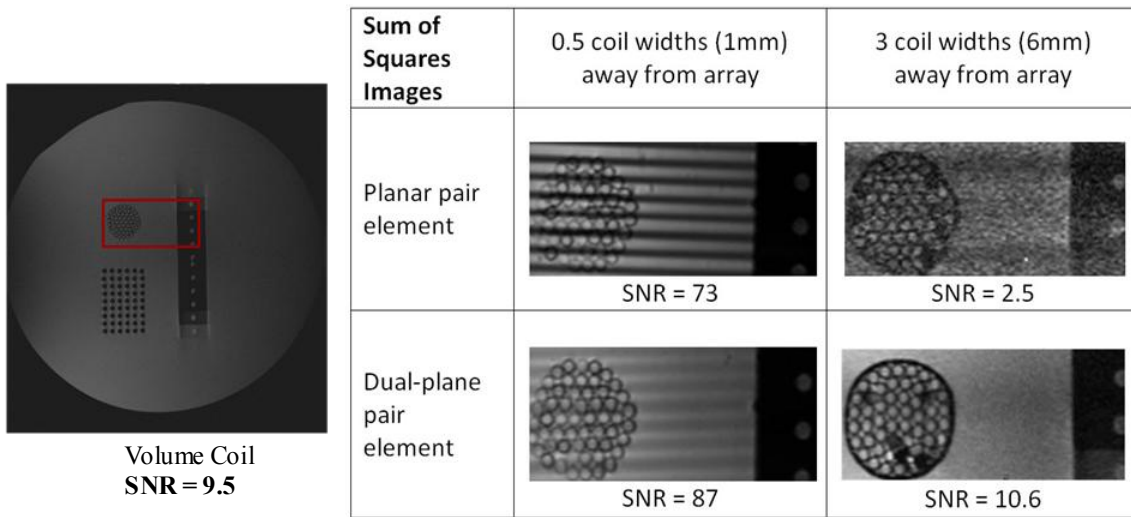
In order to illustrate the expected improvement in SNR of the DPP element over the planar pair element, single-channel images were obtained and are shown with profiles in Figure. 3.4.



**Figure 3.4** Single-channel images of both the dual plane pair (A) and planar pair (B), with plots of the relative field intensity at depths above the elements (C). At all sampled points, the raised leg has greater field intensity than the planar pair, enabling greater penetration into the phantom with sufficient sensitivity.

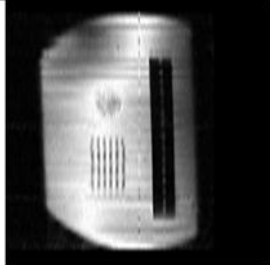
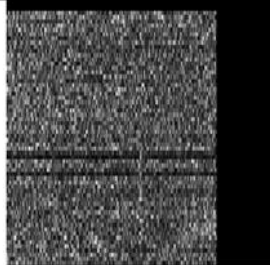
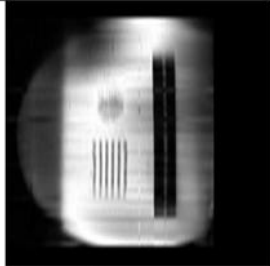
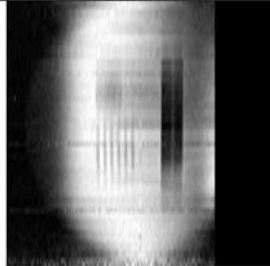
The images presented in Figures. 3.5 and 3.6 demonstrate the SNR improvement at depth offered by the dual-plane pair element. Figure 3.5 shows a reference transmit-receive image collected with the volume coil, with a 4.26 minute acquisition time,  $254 \times 126$  micron spatial resolution, and an SNR of 9.5. The red box outlines the area of the phantom zoomed to indicate the imaging capability and improvement in the SNR

provided by the new array. Comparative sum-of-squares images are shown, with the dual-plane pair offering a five-fold improvement over the planar pair array at increasing depths and an SNR equivalent to the volume coil at up to three coil widths above the plane of the array. Another notable benefit of the dual-plane pair element, at least for higher resolution (fully or partially encoding with each coil) applications, can be seen in the increased uniformity of the image acquired with the dual-plane pair elements. The highly constrained field sensitivity patterns of the original planar pair elements suit the needs of SEA imaging well, where the “resolution” of the image in what would be the phase encoding direction is instead determined by the width of the coil patterns. This narrow pattern, however, leads to a significant loss of sensitivity between elements, particularly close to the coil. This “striping artifact”, clearly evident in Figure. 3.5, is greatly reduced by the increased sensitivity (wider and deeper) of the dual-plane pair element.



**Figure 3.5** Fully encoded transmit-receive reference image taken with the volume coil (left). The red rectangle outlines the zoomed region selected to demonstrate the relative capabilities of the planar pair and dual-plane pair element arrays. The sum-of-squares comparison images on the right show the dual-plane pair element to have a five-fold increase in SNR at depth over the planar pair element – equivalent to that of the volume coil. In addition, the wider and deeper sensitivity pattern of the dual-plane pair element improves the “striping artifact” seen when using the planar pair element close to the array.



SEA Images	0.5 coil widths (1mm) away from array	3 coil widths (6mm) away from array
Planar pair element	 SNR = 39	 SNR : not measurable
Dual-plane pair element	 SNR = 97	 SNR = 19

**Figure 3.6** Single echo acquisition (SEA) images reconstructed retrospectively from the fully-encoded data sets from the planar pair and the dual-plane pair arrays. The dual-plane pair array enables SEA imaging at depths not previously possible. The array also shows significant improvements in SNR close to the coil due to an increase in the effective voxel size due to the wider and deeper sensitivity pattern – a fact which can adversely affect the achievable resolution, as described in the text.

SEA images were retrospectively reconstructed from the fully encoded sets, and the comparative SEA images are shown in Figure. 3.6. The SNR improvement offered by the dual plane pair is evident, particularly demonstrated by the fact that SEA imaging at a distance of three coil widths (6mm) from the array is achievable with the dual-plane pair elements and was not previously possible with the original planar pair elements. The SNR close to the array (1mm, 0.5 coil widths) when SEA imaging is notably increased to a degree not observed when fully encoding. The SNR behavior is explained by the same wider and deeper sensitivity of the dual-plane pair that mitigated the “striping artifact” in the higher spatial resolution sum of squares imaging. Because the “voxel

size” when SEA imaging is determined in one direction by the width of the coil sensitivity pattern, the SNR of the SEA images acquired close to the dual-plane pair is higher than the planar pair with its highly constrained sensitivity pattern because the dual-plane pair element integrates a wider region into its “voxel”. This SNR increase close to the array is not seen in the sum of squares images in Figure. 3.5 because the voxel size of the two arrays is equivalent, determined in the standard manner by phase encoding. While higher SNR typically provides an unquestionable advantage, integrating a larger region into the signal received per coil, or voxel, will actually degrade the effective spatial resolution when performing SEA imaging. Therefore, the array element of choice is, to some extent, application-dependent, affected by the desired imaging depth and spatial and temporal resolutions.

In addition to the primary goal of obtaining improved sensitivity at depth achieved by the dual-plane pair element, other advantageous factors in the design are worth mentioning. The need to decouple only nearest neighbors (straightforwardly with overlap) allowed us to maintain a lack of complexity with regard to decoupling networks. This is of particular advantage as decoupling preamplifiers at our frequency of interest (4.7T) in the number that would be needed (64) are expensive, not ubiquitous, and would require a (philosophically) undue amount of real estate compared to the 2mm x 8cm elements. In addition, the need for decoupling preamplifiers would prevent us from straightforwardly using the array design in future transmit-receive applications (after switching the varactor diodes for tuning capacitors) [68]. In addition, the unbalanced feed of the dual-plane pair (and the original planar pair) element reduces the

need for a balun, and in this case of particularly small elements, baluns are not needed at all. This condition is not the case with, for instance, balanced fed loop elements, even of this small size, with the metric being observational bench data regarding stability and tunability as the blue ribbon cables to the coils are moved.

In summary, this work has resulted in an element design for 64-channel planar imaging that offers a significant improvement in sensitivity over previous designs, maintains the ability to fully accelerate in the manner of Single Echo Acquisition imaging by keeping overlapped areas for decoupling out of the imaging region, and maintains simplicity and repeatability of design with multilayer PC board fabrication of the element and decoupling overlaps.

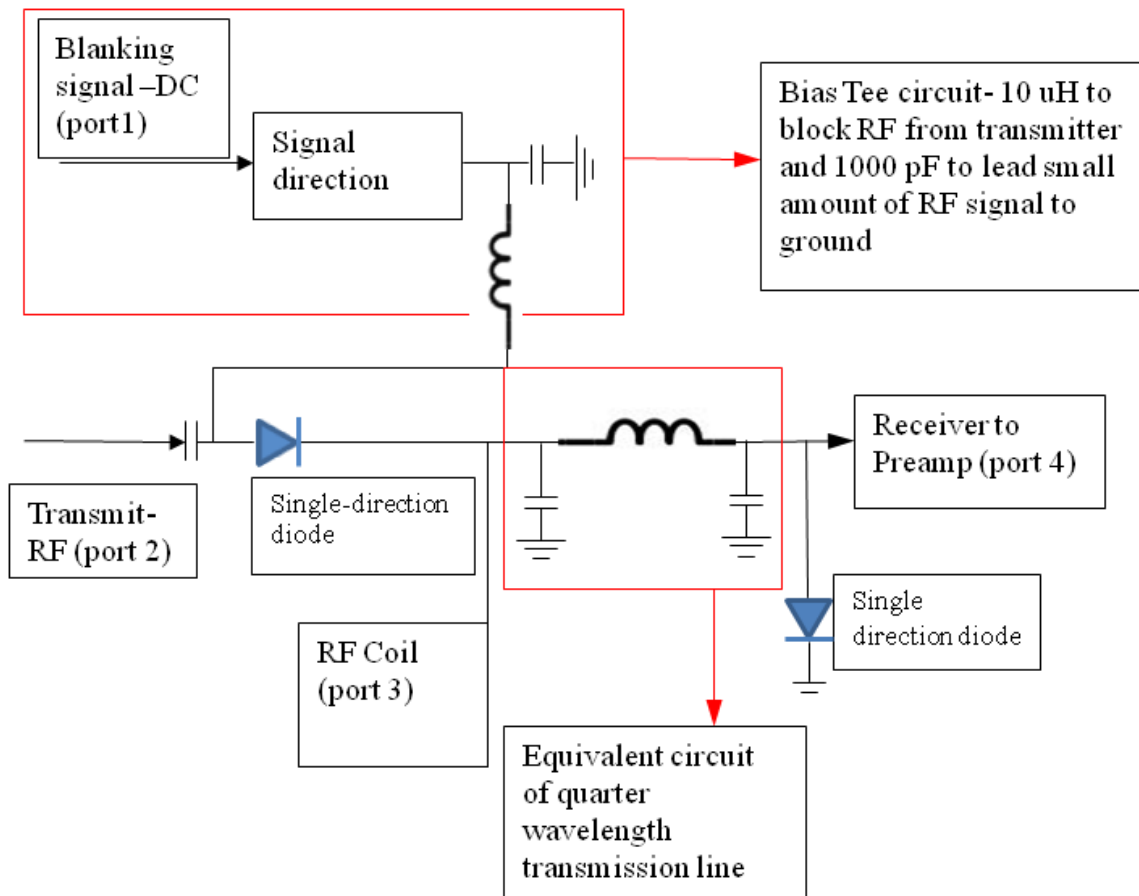
### **3.2. RF Front-End Improvement for 64-Channel System**

As with the element design described above, the RF front end work for parallel imaging that is described below was not directly applied to mouse imaging in this work. Our group has extensively studied the complexities associated with applying highly accelerated imaging – specifically SEA imaging – on curved surfaces as well as the planar surfaces shown above. Due to complications with the phase impressed by the coil when the coil size is on the order of the size of a voxel, it is not possible to use receive-only arrays on curved surfaces (such as would be needed for mice) for SEA imaging [20, 52, 53, 69]. Using coils in transmit-receive mode instead does enable this, but requires significant hardware infrastructure, such as a 64-channel transmitter, developed by a

fellow lab member and described here ([20]), 64 channel transmit-receive switches, and coils designed for transmit-receive mode. The work on the switches and arrays are described below.

### **3.2.1. 64-Channel Active T/R Switch**

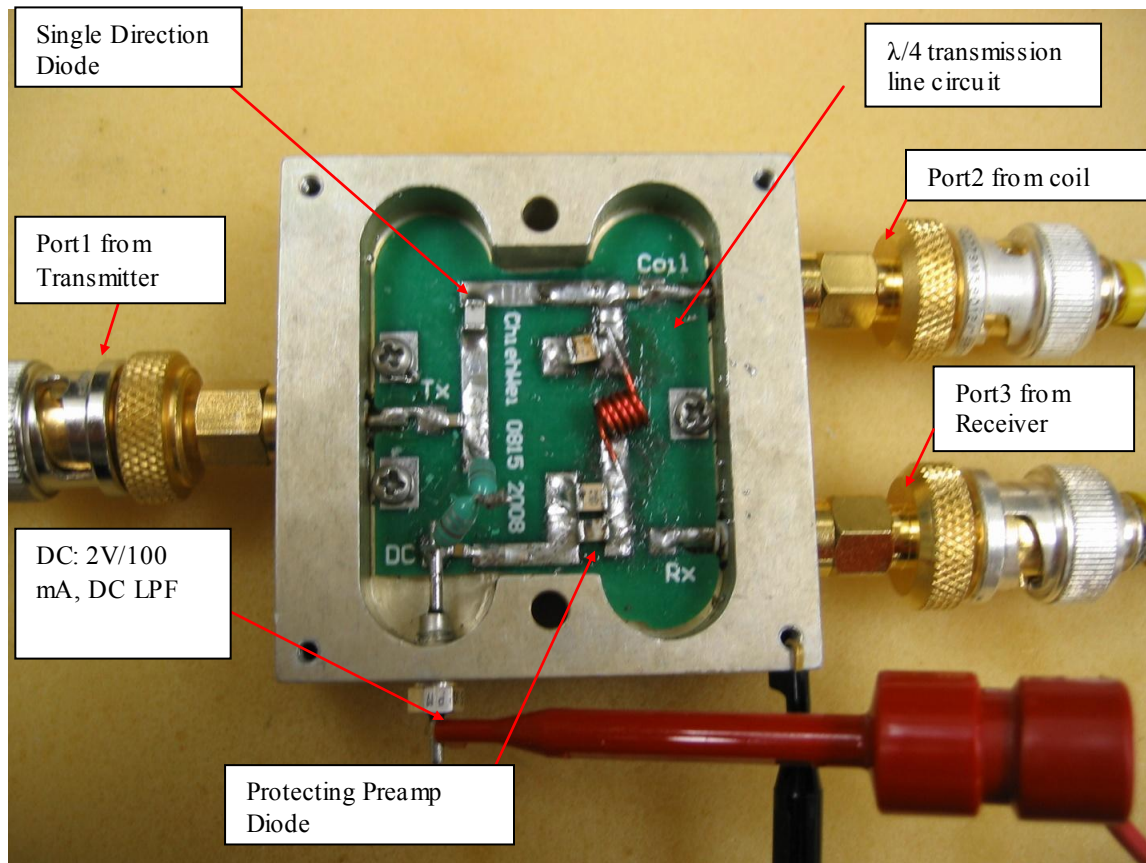
In order to integrate the 64 channel Transmit/Receive array coils with 64 channel transmitters and receivers, the RF front end was modified by the construction of 64 channel active T/R switches and  $50\Omega$  low noise preamplifiers [19, 20, 68]. The diagram of an active T/R switch is displayed in Figure 3.7, showing a lumped element transmission line to create a high impedance and a bias tee circuit to actively control single direction diodes. The switch was designed and manufactured on FR-4 PCB with an RF shielding box as shown in Figure 3.8. The circuit board is grounded to the RF shielding box and the DC is delivered through a low-pass filter. Surface mount fast switching diodes (um9401, Microsemi Corp, Aliso Viejo CA, USA) were used to actively control the stages between the transmitter and receiver.



**Figure 3.7** Diagram of active transmit-receive (T/R) Switch

In the transmit stage, the diodes are biased forward to short and pass the transmitting pulse from transmitter to coil. The other diodes after the quarter wavelength transmission line short to ground, causing a high impedance or an open circuit at the other end of the transmission line that stops the RF pulse from entering the receiver during transmit. The short circuit also protects the preamplifier by passing residual RF power to ground instead of allowing it to enter the receive port. In the receiving stage,

the diodes are reverse biased to act an open circuit. The power only flows from RF coil to receiver.



**Figure 3.8** Photograph of 200 MHz active T/R Switch. The PCB board is sharing grounded with an RF shielding box that also common ground three connected ports with board and RF shielding. The port number also represents the S parameter channel number on bench measurement from network analyzer.

From Figure 3.9, the matching of the transmitter and coil port are all below -22 dB and receiver port is -0.25 dB during transmit stage. The isolation between transmit or coil ports and receiver are both below -26 dB at transmit stage. While receiving, the S11 parameter of the coil and receiver ports are both below -21 dB and transmit port has -

0.38 dB, indicating strong power reflection with impedance mismatch. The isolation between transmitter and coil or receiver ports are both below -26 dB. The low S21 number in Figure 3.9 and S32 value in Figure 3.10 indicate the low return loss of SMA connectors with PCB circuit sharing ground with RF shielding box.

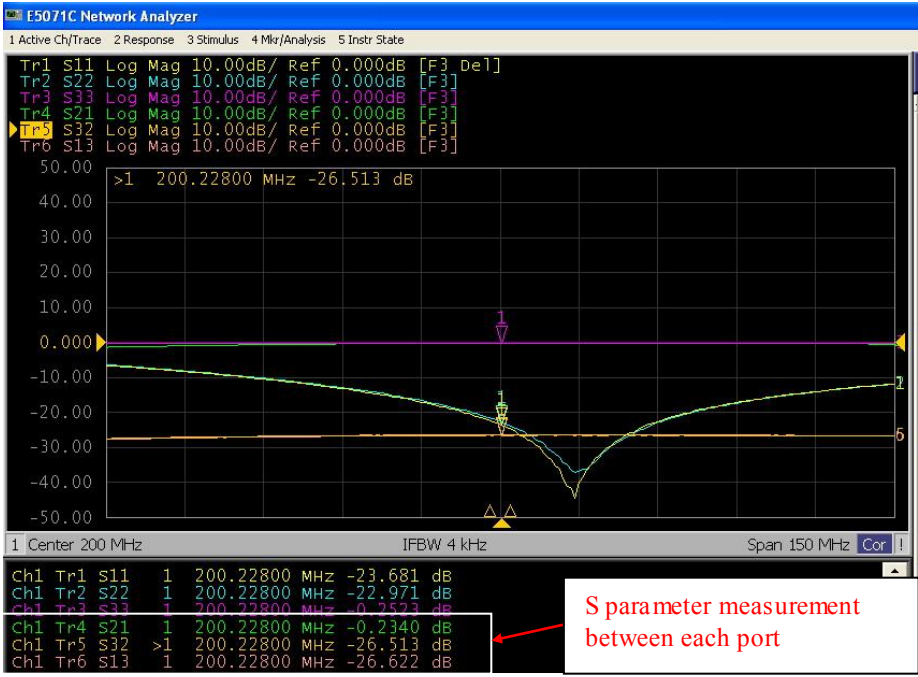
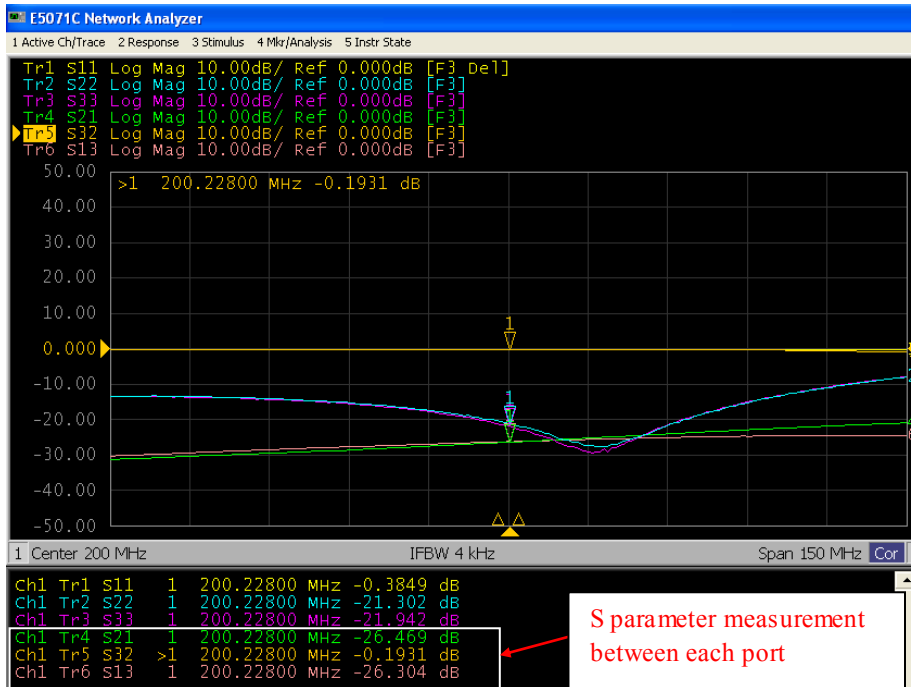


Figure 3.9 S-parameter measurement of active T/R switch during transmit stage.



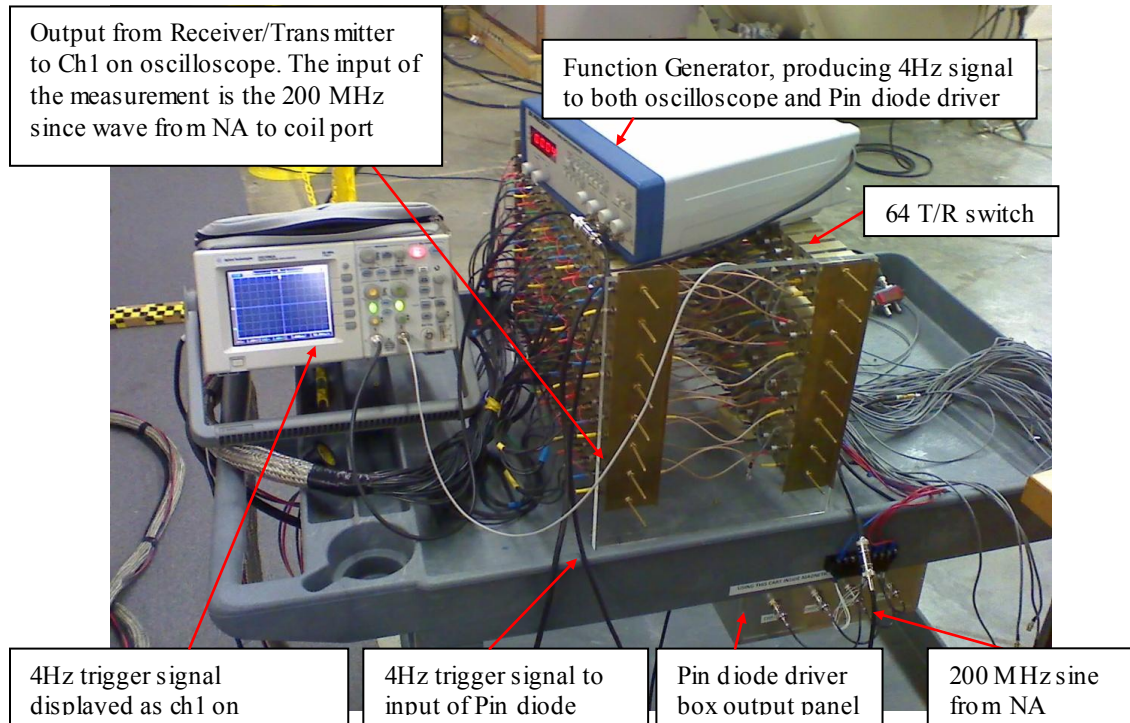
**Figure 3.10** S-parameter measurement of active T/R switch during receive stage.

### 3.2.2. Experimentally Measuring the Switching Time

The switching time of the T/R switch is also a critical issue to determine if switching is sufficiently fast to deliver the transmit pulse. The common 90/180 excitation pulse in spin echo sequence is the milliseconds range and could be shorter to several hundred microsecond for short TE experiments such as the black blood detection. The 4 Hz square trigger signal from the function generator is delivered to an oscilloscope and one of the 64 channel active T/R switch systems. The pin diode driver receives a trigger signal to generate 10 volt/100 mA per channel into the T/R switch system with -10 volts reverse bias. A high-pass filter is applied to monitor the 200 MHz

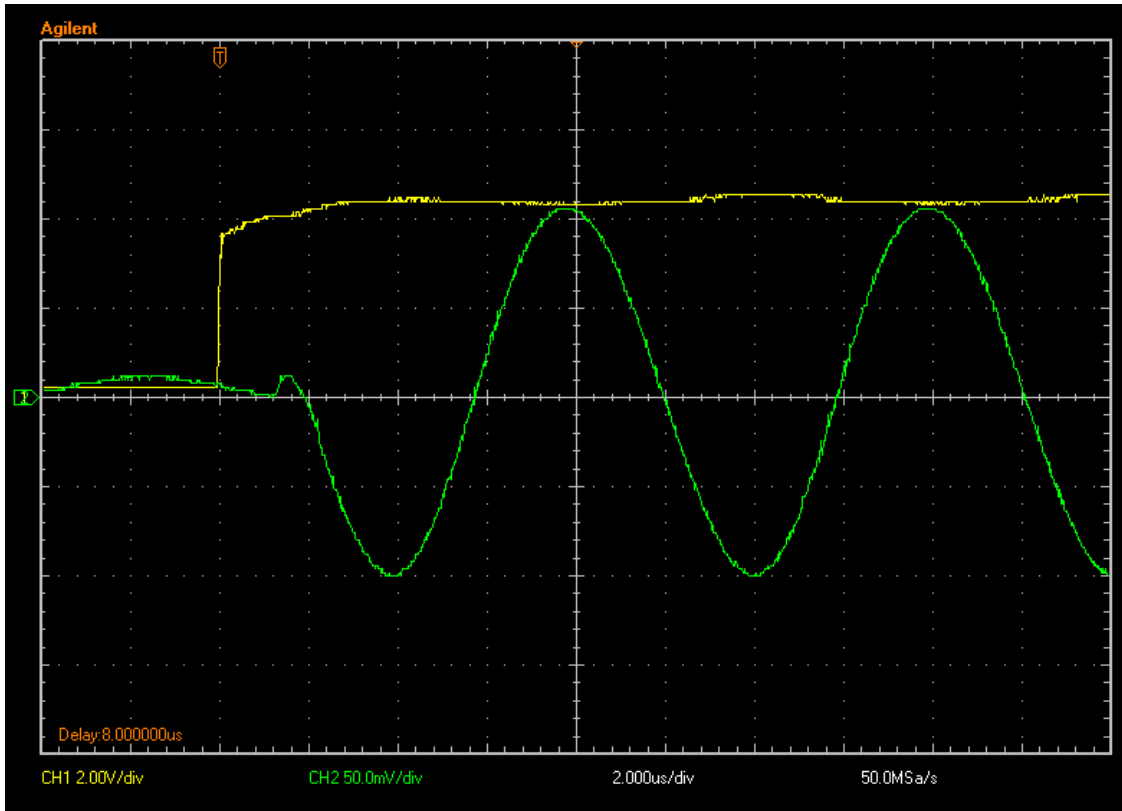


signal from the T/R switch. The configuration of switching time measurement was posted as Figure 3.11.



**Figure 3.11** Switching time measurement configuration.

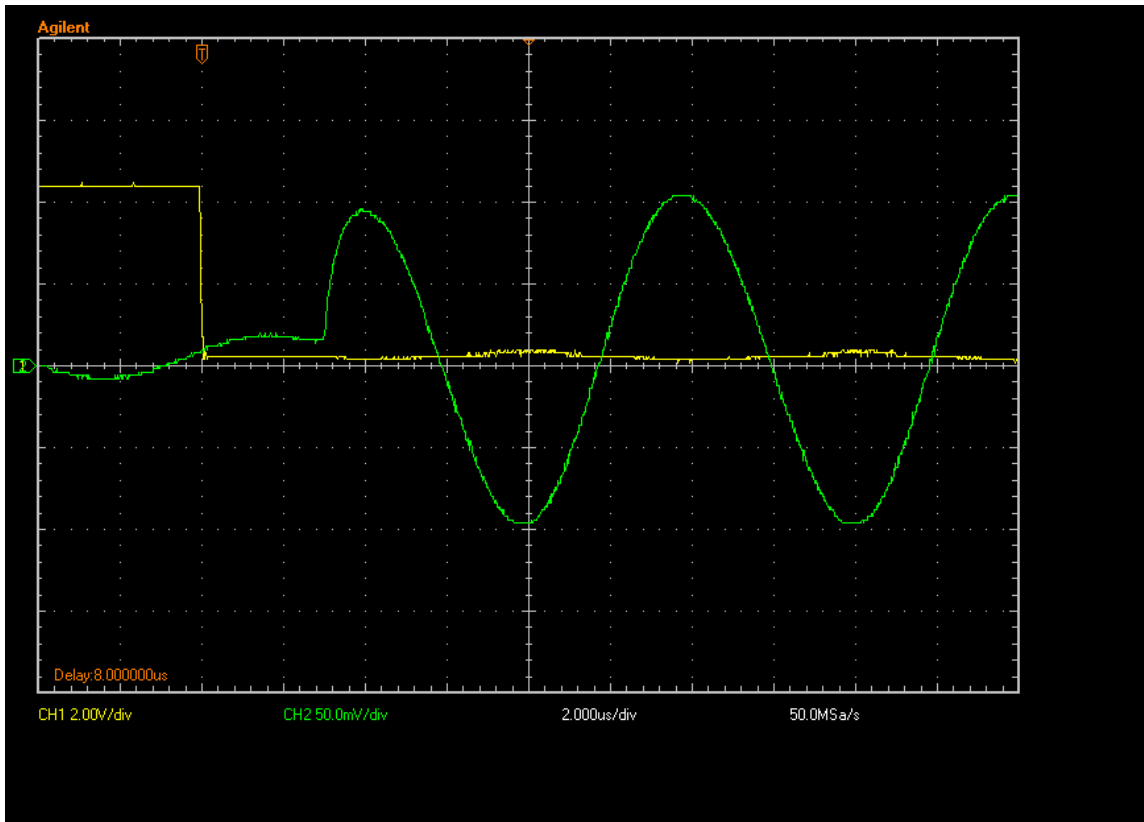
In the transmitting stage, the switching on time was  $1.9 \mu\text{s}$  from the oscilloscope measurements. The RF input was connected to the transmit port and the coil port is linked to Agilent oscilloscope. Figure 3.12 indicates the time difference between the trigger (yellow: channel 1) and output of RF pulse (green: channel 2). The x scale of channel 1 is  $2 \mu\text{s}$  per division. Similarly, the switch off time was measured as  $3 \mu\text{s}$ , obtained by reversing the trigger level.



**Figure 3.12** Time of switching on at transmit stage.

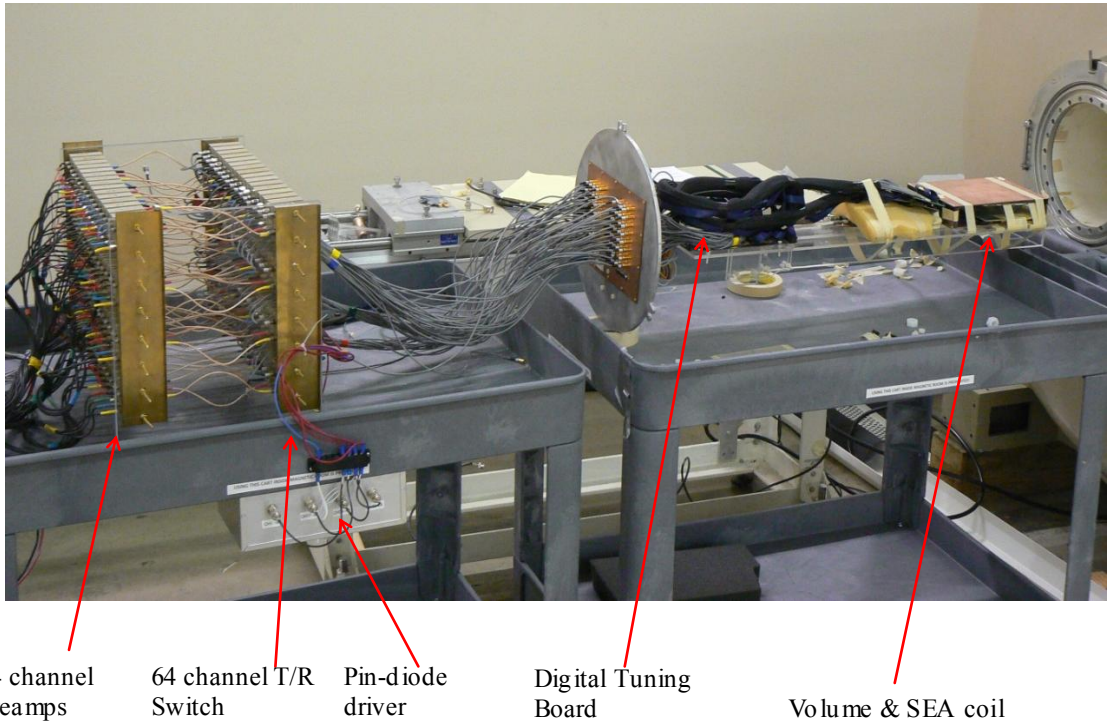
In the receiving stage, the RF pulse is connected to the coil port from the network analyzer and the output from the receiver is linked to an oscilloscope. The switching off time is within  $3.2 \mu\text{s}$  as shown in Figure 3.13. After switching off, the power is picked up from the receiver port; meanwhile, the switching on time is measured in the same way and found to be  $2.24 \mu\text{s}$  in the receiving stage.

The switching on/off times during transmit and receive stage were measured as within several microsecond range that was quick enough to trigger transmit pulse or starting acquisition window for receiving.



**Figure 3.13** Time of switching off at receive stage.

The receiving chain of RF front end improvement for imaging setting is displayed in Figure 3.14 for 64 channel experiments.



**Figure 3.14** Configuration of RF front end components in 64 channel experiment setting.

## CHAPTER IV

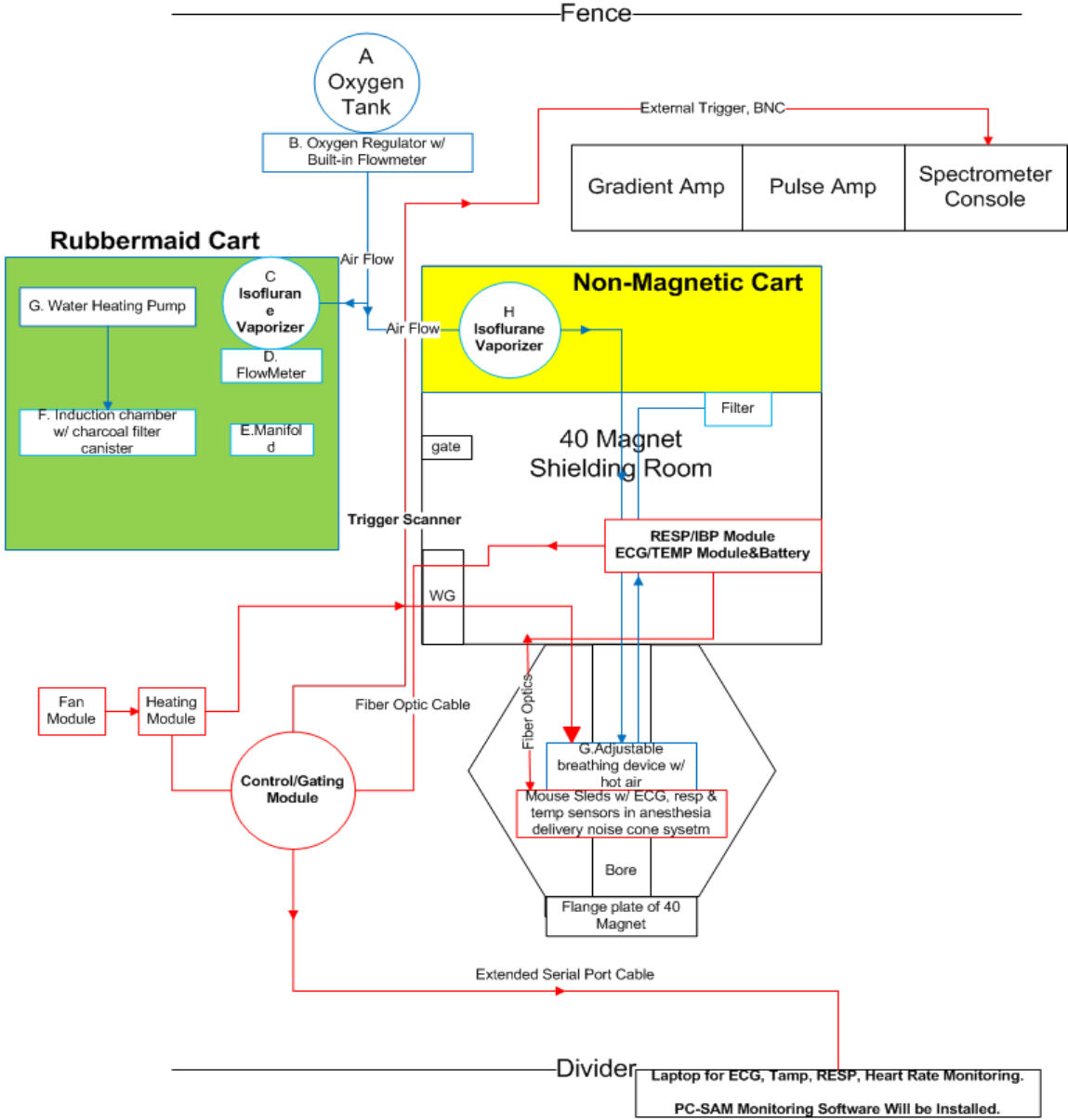
### DEVELOPMENT OF *In Vivo* SMALL ANIMAL MRI CAPABILITY

The description of tailoring the parallel imaging hardware described in the previous chapter – specifically the array coils – for use on mice will be described in Chapter V. This chapter, however, describes the specific adaptations of the facilities to support the physiological aspects of *in vivo* MRI – the anesthesia delivery as well as the monitoring of and triggering to the physiological signals of the mouse.

#### 4.1 Introduction

To deliver anesthesia continuously for several hours in the scanner, the air anesthesia method is widely used to stabilize the small animal for MRI imaging. Isoflurane is the common medicine to mix with pure oxygen as the anesthesia gas. Two units of anesthesia gas are applied to the small animal for long term scanning inside of the magnet. A nonmagnetic isoflurane vaporizer on the animal and coil loading cart is located inside of the RF shielding room and all components within the shielding room are nonmagnetic and MR-compatible. Another vaporizer is located at the animal preparation table to initially knock down the animal and allow for mounting sensors for cardiac gating. The anesthesia units together with with the gating system are the two critical components for *in vivo* animal experiments. The arrangement of the air-flow system, ECG-gating system, and anesthesia units is shown in Figure 4.1. Additionally,

small animal holders were designed and built in house to easily load and accommodate mice in the 40-cm horizontal magnet with all of the physiological sensors and routing for anesthesia gas delivery and scavenging.

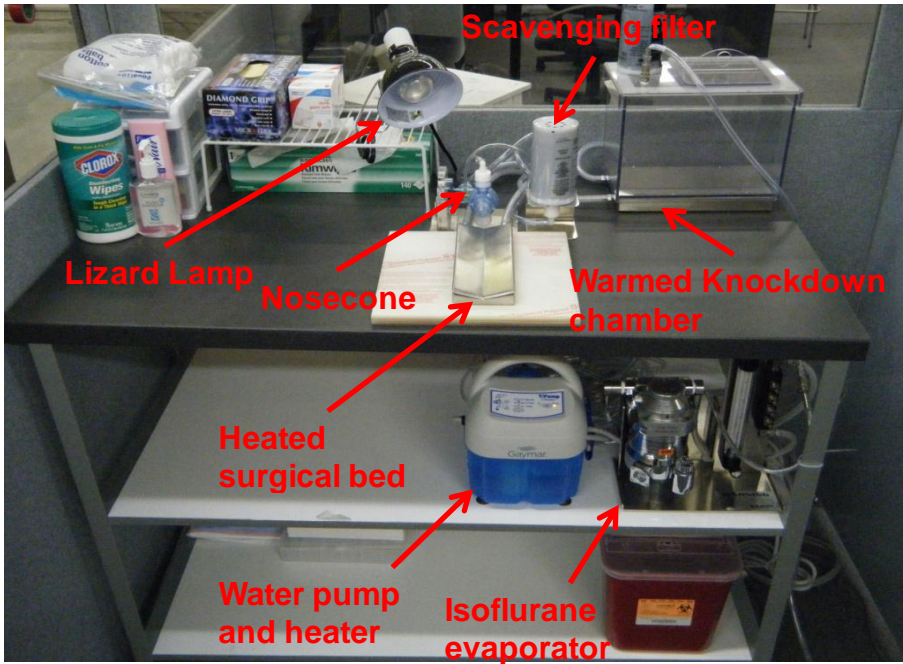


**Figure 4.1** Flowchart of anesthesia and gating system for 4.7T/40cm scanner at the MRSL

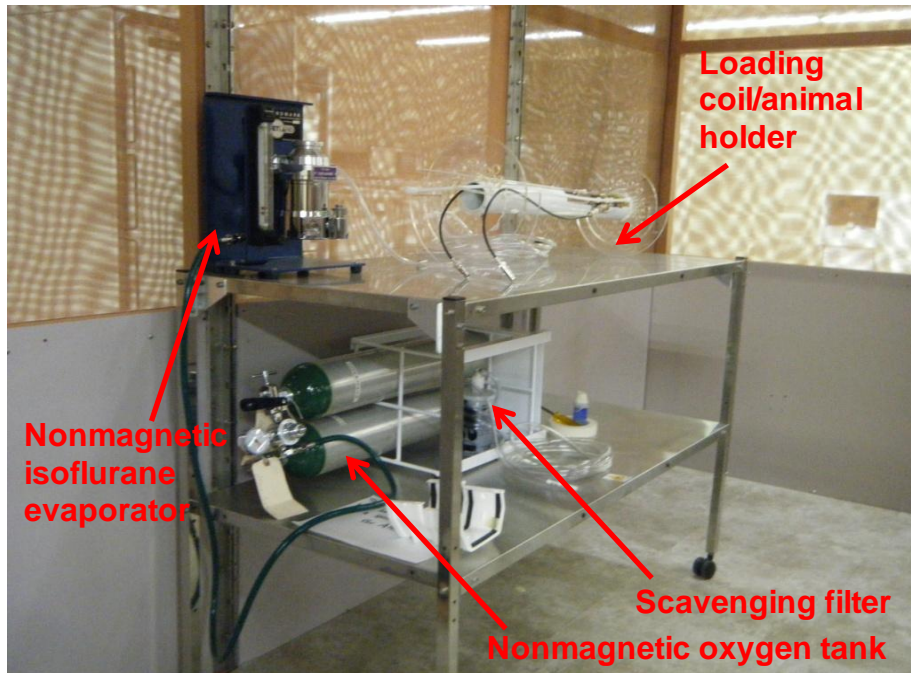
## **4.2 Anesthesia Units**

An animal preparation table holds the isoflurane vaporizer (EZ-1500; EZ systems, Palmer PA USA) that initially knocks down the mouse inside a chamber. The anesthesia gas is then routed to the surgical bed as shown in Figure 4.2. A water warming system and lizard lamp helped to maintain the animal body temperature on the bed. On the warming surgical bed, the nose cone supports anesthesia delivery to keep the animal down while mounting the ECG, temperature, and respiratory sensors on the animal. Please see Appendix I for more information on this. This process is greatly expedited by the use of a “mouse sled” (Dazai Research Instruments) with incorporated sensors. The sled and animal are placed inside the animal holder and moved to the RF shield room to load in the coil, connect optical cables to the gating system, and load in the magnet. Another MR-compatible isoflurane vaporizer (VSA-2100; Vetland, Louisville KY USA) inside the shield room handles the anesthesia needs during scanning. The unit is movable on a cart inside of the shield room and shown in Figure 4.3.





**Figure 4.2** Small animal is initially knocked down here and mounted with sensors on the animal preparation table.

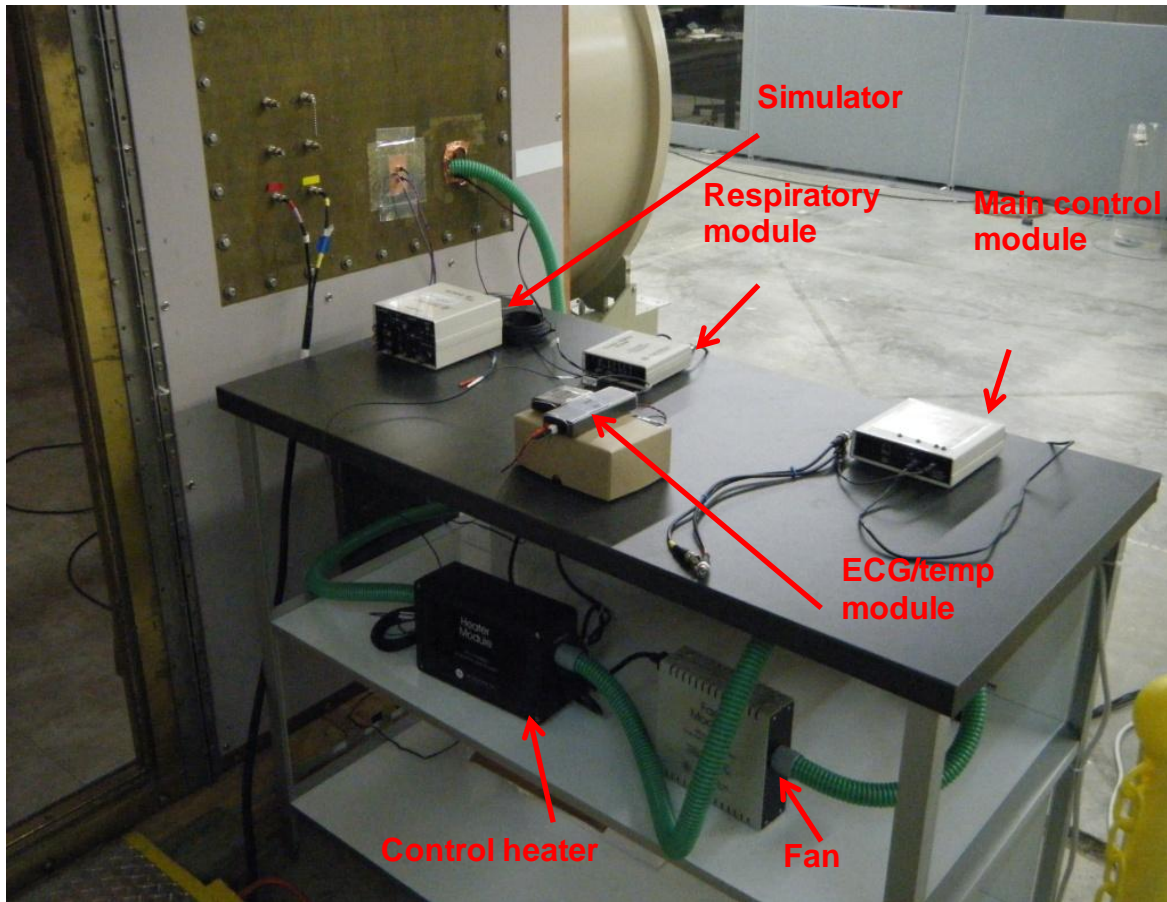


**Figure 4.3** MR-compatible units are located inside of the shielding room to support long-term anesthesia gas.



### **4.3 Gating System**

A cardiac gating system (Small Animal Instruments, Inc., Stony Brook NY, USA) is used to gate to the cardiac function as an external trigger for the scanner. The system includes the main control module, respiratory module, ECG/temp module, and heater module. These modules are physically located outside the shield room, as shown in Figure 4.4. The trigger signal is sent to the scanner and monitored on a laptop located next to the main Varian control console. The communication between the main control module and each sensor module are via several optic fibers that pass through the waveguide on the panel of RF shielding room and perform as non-magnetic cables without coupling current. A simulator module provides ECG, temperature, and gradient waveforms to help users debug the issues associated with obtaining physiological signals from the small animal.

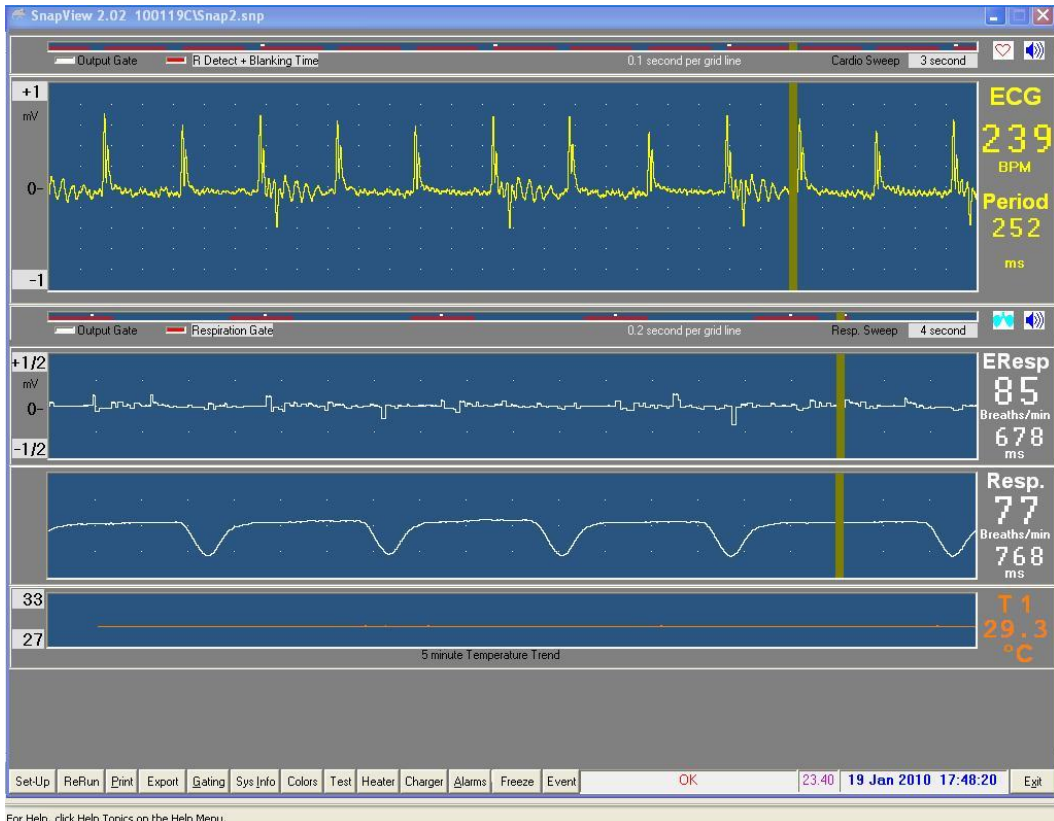


**Figure 4.4** Cardiac gating modules include of the respiratory, ECG/temperature, main control, and heater.

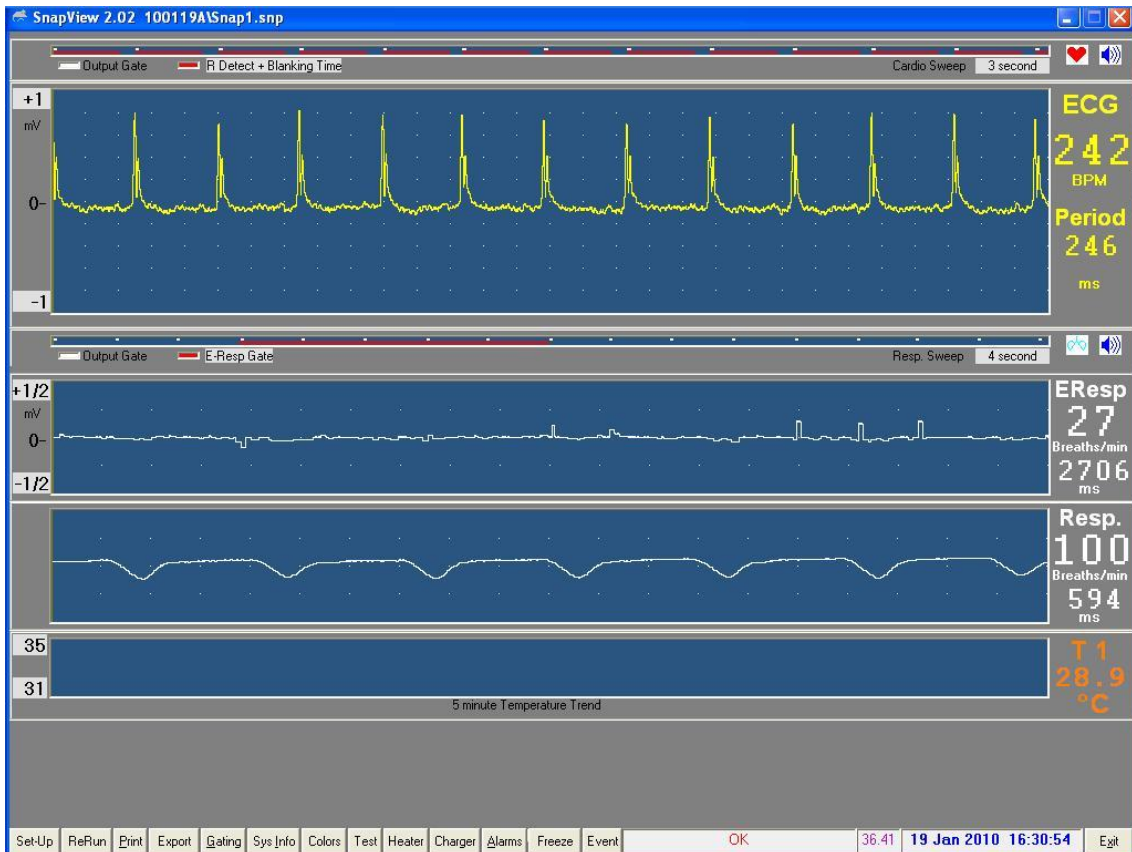
An example of a screen capture from the small animal gating software is shown in Figure 4.5. The software monitors the ECG, temperature, and respiratory signals for the researcher operating on the Varian console. The trigger signal can be gated with the R wave and breathing cycle to initiate the spin echo (SEMS) sequence to remove motion artifacts. On the scanner side, the external trigger option in the SEMS sequence must be chosen on the VNMRJ software panel. The trigger output is controlled by software that determines the threshold of the R-wave, blanking period of the trigger signal, trigger source options, and even a body temperature or cardiac alarm for animal cardiac and

breathing cycle. The body temperature of the animal should be monitored during anesthesia gas as the warm air is applied by the fan and heater. The combination of the gating and anesthesia system maintains comfortable and monitored conditions for the mouse to allow for 5 or 6 hours of imaging inside the magnet.

The act of actually imaging once everything is in place is not totally straightforward. In the Figures 4.5 and 4.6, the ECG triggering signals are compared in and out of the presence of imaging gradients, respectively. The baseline noise of the ECG waveform is greatly increased in the presence of gradients and is reduced when the pulse sequence is stopped.

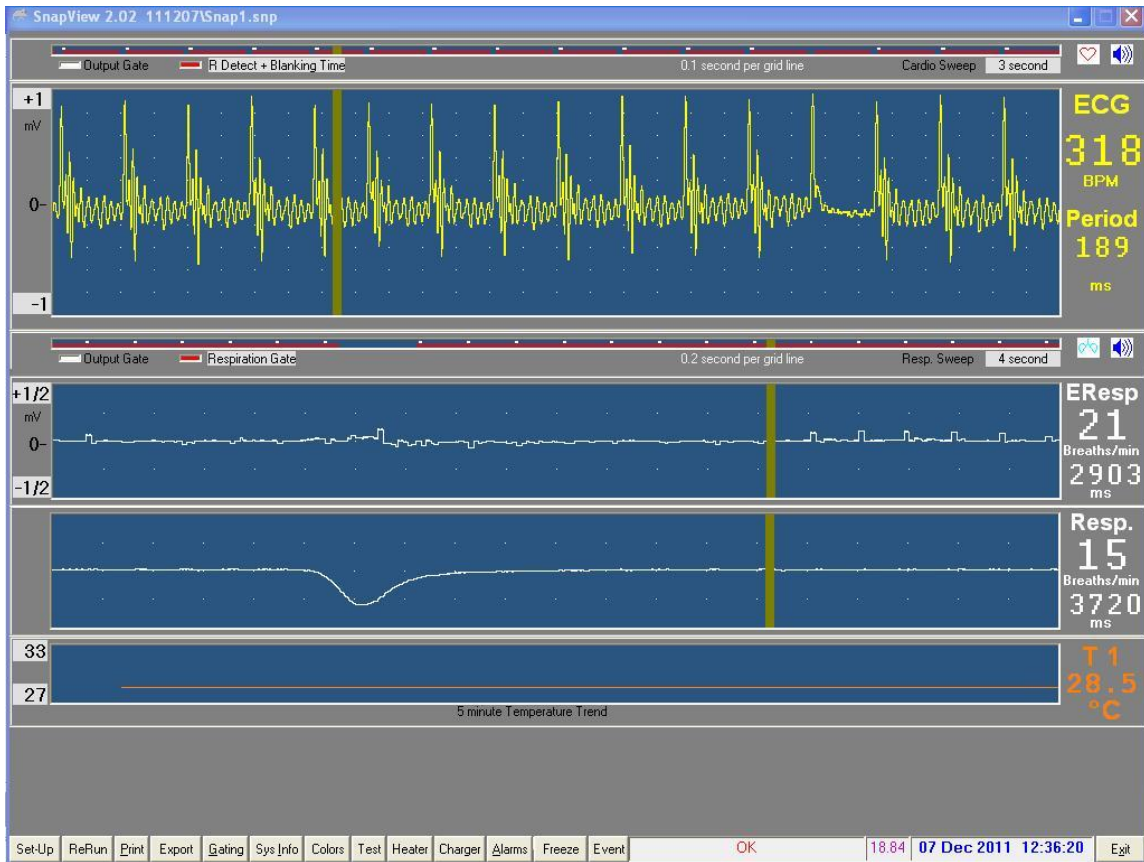


**Figure 4.5** Small animal monitoring software with gradient on

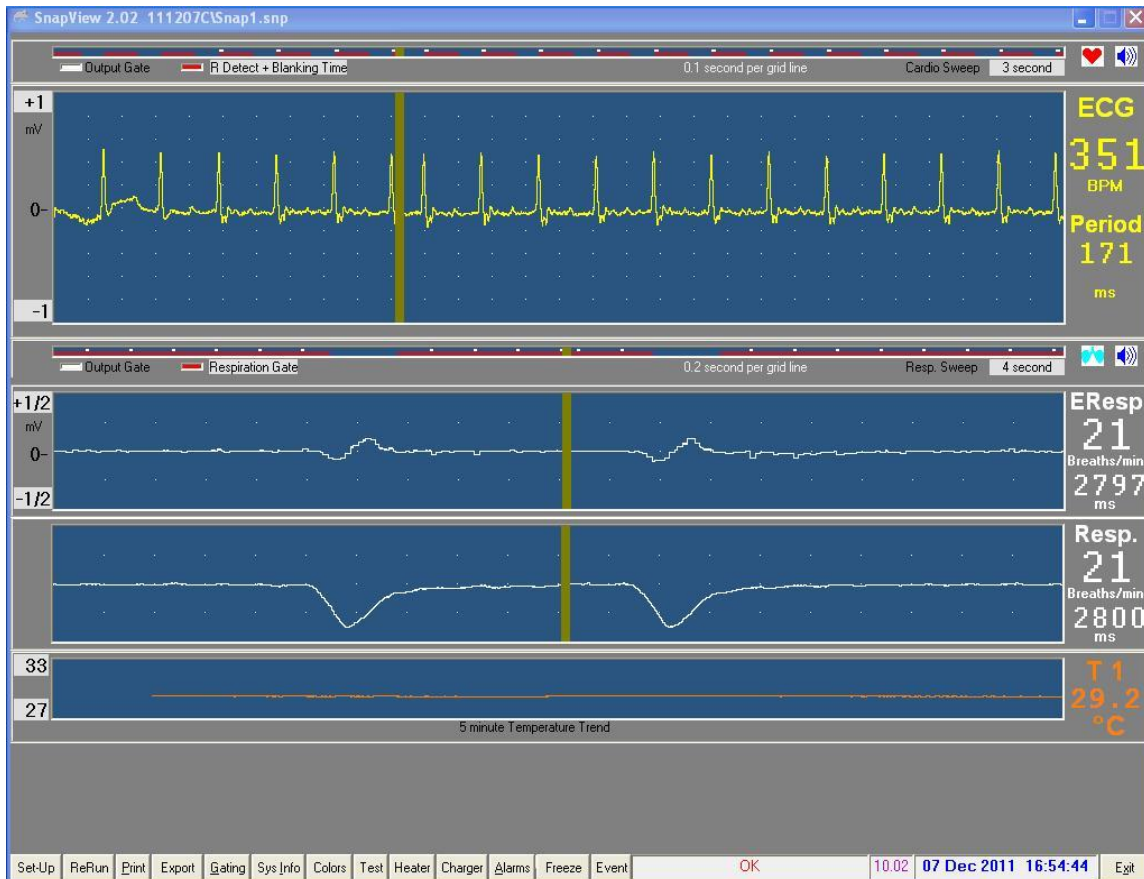


**Figure 4.6** Small animal monitoring software with gradient off

The practical solution to remove the baseline noise on the ECG waveform was to reduce the motion of the wire connecting the sensor on the mouse to the module outside the magnet room that was induced by gradient pulse. When both ECG cables were tightly taped down against animal holder to stabilize the cables, the baseline noise was reduced. A very visible case of this correction is shown in the very noisy baseline in Fig. 4.7 as compared to the improvement seen after securing the ECG wires, shown in Fig. 4.8. The difference between the baseline noise Figures 4.5 and Figure 4.7 is the length of TR that the R wave was triggered sooner or later based on different value of relaxation time.



**Figure 4.7** Baseline noise of ECG waveform with gradient on before fixing both ECG cables on holder.

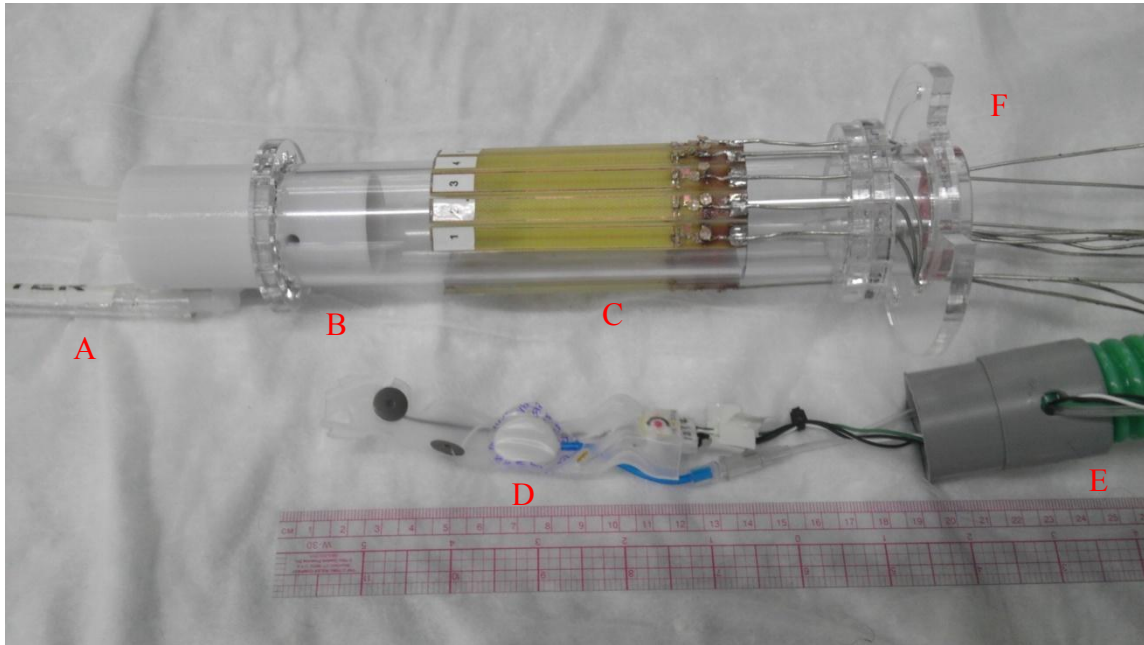


**Figure 4.8** Corrected baseline noise of ECG waveform with gradient on and ECG cables secured on holder .

#### 4.4 Small Animal Holders

To support delivering anesthesia gas to the animal, allowing for connecting and routing of gating sensors to the mouse, and supporting the RF coil, an animal holder was designed and manufactured in house. The isoflurane gas is delivered through an inlet and outlet port on the nose cone and warm air comes from the heater to the rear of the animal inside the holder. The outer diameter of the holder is 1.5 inches and contains an adaptor plate to center and lock onto the transmit birdcage as shown in Figure 4.9.





**Figure 4.9** Small animal holder with sensors—(A) anesthesia gas inlet and outlet, (B) nose cone from 3D printer, (C) main body of animal holder with array coils, (D) animal cradle with ECG, temperature, and respiratory sensors, (E) warm-air tubing, and (F) adaptor plate to connect with rat-size birdcage.

#### **4.5 Standard Operation Procedure of Anesthesia and Gating Setting**

After running *in vivo* experiments several times with veterinarians, the standard operating procedure for using the anesthesia system was written and can be found in APPENDIX I. It indicates proper oxygen pressure for gas flow with specific isoflurane percentages at different stages of the experiment. Control of the small animal gating system and the default settings are listed and explained in APPENDIX II to aid in improved pickup and triggering of the cardiac and respiratory cycle. Because of the diversity of physiological signals and conditions of different animals, fine adjustment of anesthesia and the gating system is required for every animal.

**CHAPTER V**  
**TAILORING PARALLEL IMAGING METHODOLOGY and HARDWARE FOR**  
***In Vivo* MOUSE MRI**

This chapter will cover the adaptation of the parallel imaging hardware described in CHAPTER III – specifically the array coils – to match the needs of mouse imaging. This includes the use of a smaller number of channels (ten instead of 64) in order to penetrate deeper into the mouse with larger elements as well as the concomitant modifications to manage the increased coil-to-coil coupling and bore size restrictions.

### **5.1 Introduction**

The mouse continues to grow in importance as the laboratory animal of choice for applications based on pharmacological or surgical interventions used in combination with or without genetic modifications [70]. Therefore, the need for noninvasive tools for characterizing disease progression or serial assessment of response to intervention follows, and MRI offers all of its traditional benefits over other imaging modalities with regard to contrast and versatility [71]. Depicting the small details of mouse morphology as compared to human, however, presents a challenge to the fundamental capabilities of MRI with regard to maintaining SNR in high-resolution imaging when the voxel size is small. Some of the SNR loss can be recovered through the use of dedicated high-field animal scanners and specialized RF coil design, but much of the signal loss must be



regained through time-consuming acquisition and averaging of data. Therefore, high-resolution MR imaging of mice is generally considered to take on the order of hours.

The use of array coils and accelerated imaging is a natural solution path to consider, particularly because multiple channel receivers are now ubiquitous and the benefits of parallel imaging have become apparent in the human and murine imaging arena in nearly all applications [14]. Indeed, a four-channel mouse spine array is available commercially (Mouse spine array; Rapid MR International, Columbus Ohio, USA; [72]), and parallel imaging of mice is a growing area of research. Two-channel work that focused on the challenges of cardiovascular MR imaging of multiple mice has been reported [18]. The eight-channel small animal coil array has been implemented on a clinical 3T scanner [73] and even a non-proton C13 MRI [74]. Also, the eight-channel mouse body arrays have been demonstrated on high-field 9.4T scanners [15]. Based on the needs of similar genomic and biomedical research on rats, the 16-channel rat body coil arrays have been introduced to the field on 7T MRI scanners [75]. Most recently, a 20-channel volume array for use in a clinical 3T system is reported [76]. In general, researchers realize the challenges associated with the miniaturization of the coils, including but not limited to maintaining sample noise dominance, sensitivity in the element-to-element decoupling process, and the lack of space for traditional hardware such as baluns and cable traps, active decoupling networks, and low-input impedance preamplifiers.

This chapter describes the 10-channel mouse array coils, transmit coils, and a modular 16-channel low-input impedance preamplifier board that constitute a compact

and straightforward approach to parallel imaging of mice. The element design 1) ensures that no coil-to-coil decoupling mechanism is needed other than the low-input impedance preamplifiers; 2) inherently decouples from a homogenous transmit field, eliminating the need for active decoupling; and 3) reduces, and in this case, eliminates the need for baluns and/or cable traps. The transmit coil design ensures an extremely uniform sensitivity pattern, and the 16-channel preamplifier board described is compact and modularized for straightforward use with any array coil. The SNR objective of mouse array is achieve equal or better SNR than mouse coil at the center of image.

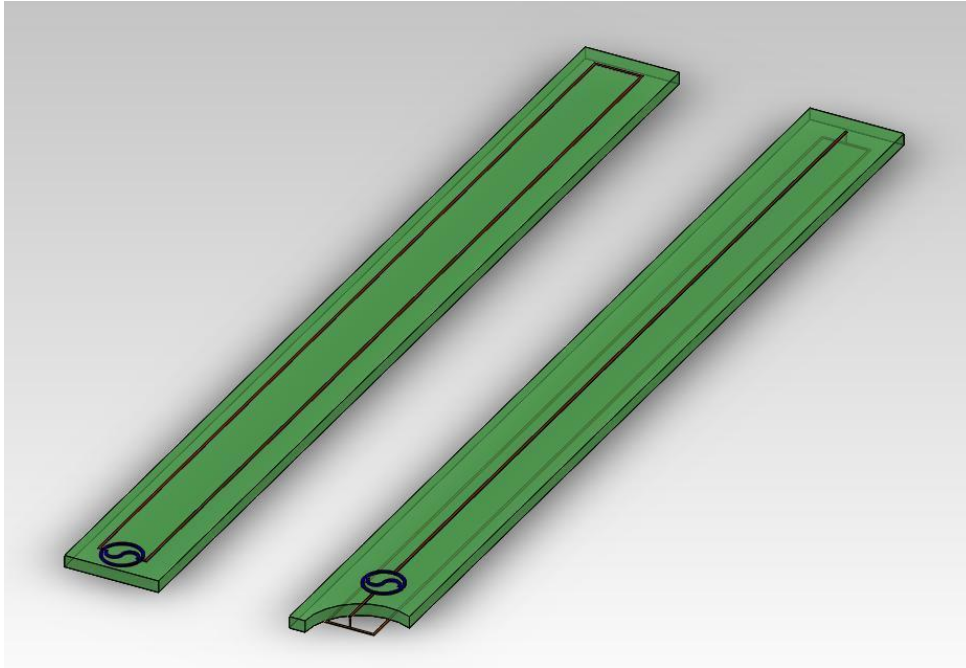
## **5.2 Ten-Channel Array Coil Design**

Each dual plane pair element was designed by PCB designing software EAGLE 5.11 and fabricated in-house by an LPKF C30 circuit board plotter. Each DPP coil was 7.4 mm by 7 cm on a standard FR-4 circuit board. A similar microarray structure is designed and constructed for highly parallel wide-field-of-view microscopy or transmit array coils [54, 69]. Similar human cardiac array coil design was chosen to perform top-to-bottom five-channel subarrays for murine magnetic resonance imaging [42]. The width of the DPP element was designed to be extended wider than a previous microarray used 2mm width in dual plane pair elements and wraps the elements outside of the 1.5-inch diameter animal holder. The length of the array was expected to cover the body of a standard-size mouse. The top side of the coil has only a signal trace and all of matching network and components were moved to back side of element facing outward from the

acrylic cylinder. A 15-pF capacitor was applied between back signal traces and ground to provide a homogeneous field pattern along the coil. The back capacitor acting as distributor capacitor makes element profile perform as Gaussian distribution above the element. The matching network was also located on the backside of the element that included two variable 6–25-pF capacitors (9702-6; Johanson Manufacturing Corporation, Boonton NJ, USA), a microstrip inductor rather than wired inductor to save space for mouse array and a 47-pF fixed value capacitor (A series, American Technical Ceramics, Huntington station NY, USA), which was parallel to the trimmer tuning capacitor. A T-type matching network (two variable capacitors and a 0.5 x 3.81-mm microstrip inductor) was chosen to resonate the coil at 200 MHz and decoupled with a low-input impedance preamplifier [77]. The semirigid coaxial cable functions as a phase shifter at 200 MHz to perform high impedance at coil end with low-input impedance preamplifier.

### **5.2.1 Advantages of Element Design for Compact-Volume Array Coil Construction**

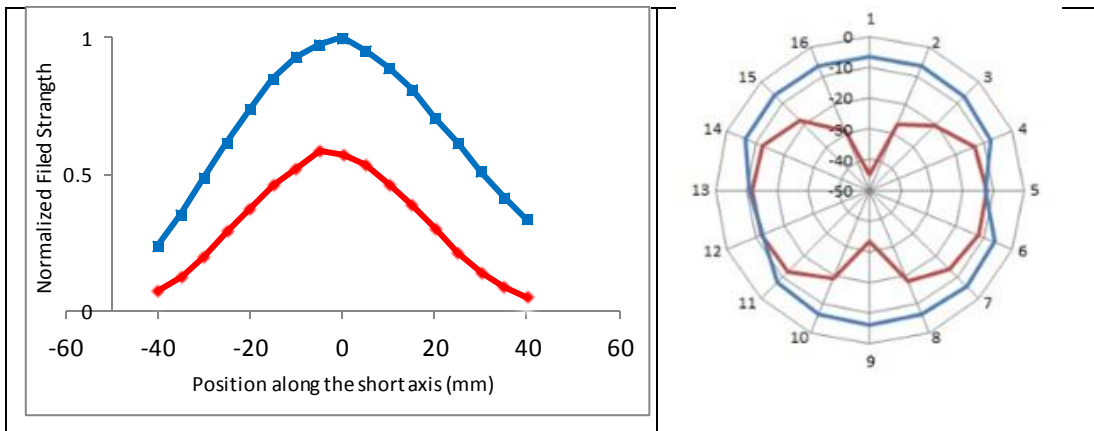
Due to the localized field pattern, there is no need for element-to-element decoupling other than the isolation preamplifiers. The DPP configuration and loop element is illustrated as Figure 5.1 and the field plots across the single-element DPP and loop are shown in Figure 5.2(A) where the intensity is normalized to the maximum value of a loop element. The DPP element showed a similar field pattern as the loop but in an orthogonal direction with respect to the field.



**Figure 5.1** DPP and loop element configuration—The left side is the loop structure and the right side is DPP element at both sides of the PCB.

The DPP element is also inherently decoupled from a homogenous transmit field due to the flux canceling geometry of the two halves [78]. The coupling  $S_{21}$  measurements between the transmitting linear birdcage coil and receiving array elements are made by a network analyzer on the bench as shown in Figure 5.2(B). Both coils are held against the animal holder with a specific rotation stage to measure the  $S_{21}$  value at different and specific rotation angles. The coupling plot illustrates the smallest coupling as with the DPP element on the top-to-bottom half of the five-channel element design. Specifically,  $S_{21}$  between the linear volume coil used for transmit and the DPP element used in the top-to-bottom half mouse array design has a maximum coupling value of -14.4 dB at position 11 within the volume coil. This is in contrast to a loop, which has -

6.6 dB at position 2. Figure 5.2.(B) is the  $S_{21}$  measurements between the transmit coil and a DPP element in 16 different positions corresponding to the transmit birdcage leg locations. To illustrate the improved decoupling of the DPP elements from the transmit field, the same measurements are shown using a conventional loop element. This eliminated the need for active detuning on the array. Back-to-back diodes (UM9989B; Microsemi, Irvine CA, USA) across each element are added for insurance to eliminate induced current on coil.



**FIG 5.2 (A)** Position vs. normalized field strength plot across the DPP and loop element. **(B)** Coupling measurement between transmitting and receiving elements. Number 1 to 16 denotes the position of 16 rings of transmitting birdcage coil. Radius distance represents the  $S_{21}$  coupling in dB. Blue represents the loop coil and red is DPP element.

The DPP element design reduces the need for cable traps or a balun, and in this case where the element is so small, eliminates the need of coil stability. The unbalanced feeds of the dual plane pair elements reduce the need for a high-impedance balun on the coaxial cable. The small size of DPP element with semirigid coaxial cable eliminates the use of a balun to stabilize the coil. In particular, the semirigid coaxial cable could be

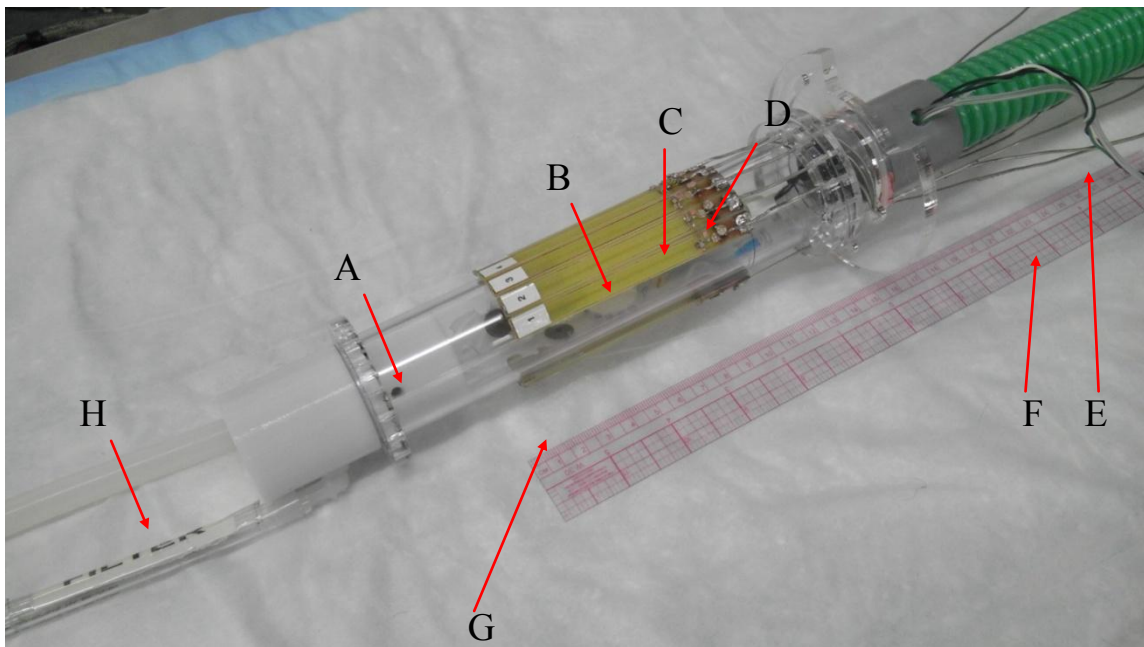
fixed inside the magnet to help stabilize the array. Eventually, copper tape is taped around the coaxial cable outside of birdcage to act as a balun for the DPP element but simply used to reduce coupling from volume coil not among arrays.

The Q value of the DPP element is measured by an Agilent E5071C Network Analyzer with voltage standing wave ratio (VSWR) measurement and a 2:1 bandwidth ratio. The Q value of the unloaded element is 80.3 and the Q value for a loaded element is 60.7. A 1.32 Q value ratio generally represents loss dominance by the coil noise. However, comparing similar DPP microarrays used to microscopy imaging, the Q value ratio of the mouse coil is actually much higher than the microarray value of 1.07, which indicates the mouse element couples more into the phantom. The Q value ratio of the coil indicates that sample loss is greater in the larger array and that copper loss from the coil would be less dominant. Larger Q value ratio represents element loaded more from adding sample resistance. The sample noise dominates copper loss giving the coil better SNR.

### **5.2.2 Array Construction and Configuration**

Ten DPP elements are assembled outside of the 1.5-inch OD acrylic cylinder. A photograph of the array coil is shown in Figure 5.3, including the array coils, components, and the animal holder with anesthesia units and gating sensors. The 10-channel DPP elements literally surround the outside of the animal holder and attach to a transparency which can slide backward and forward, together with the arrays to load mice into the animal holder. Because all 10-channel DPP coils are fabricated from

standard FR-4 rather than flexible circuit board material, all of the DPP element is not facing toward the center of the animal holder and wrapped around cylindrical acrylic concentrically. The display shows slightly different element coupling between neighboring coils and the adequate element to element decoupling is also presented, which is shown as a decoupling matrix later.

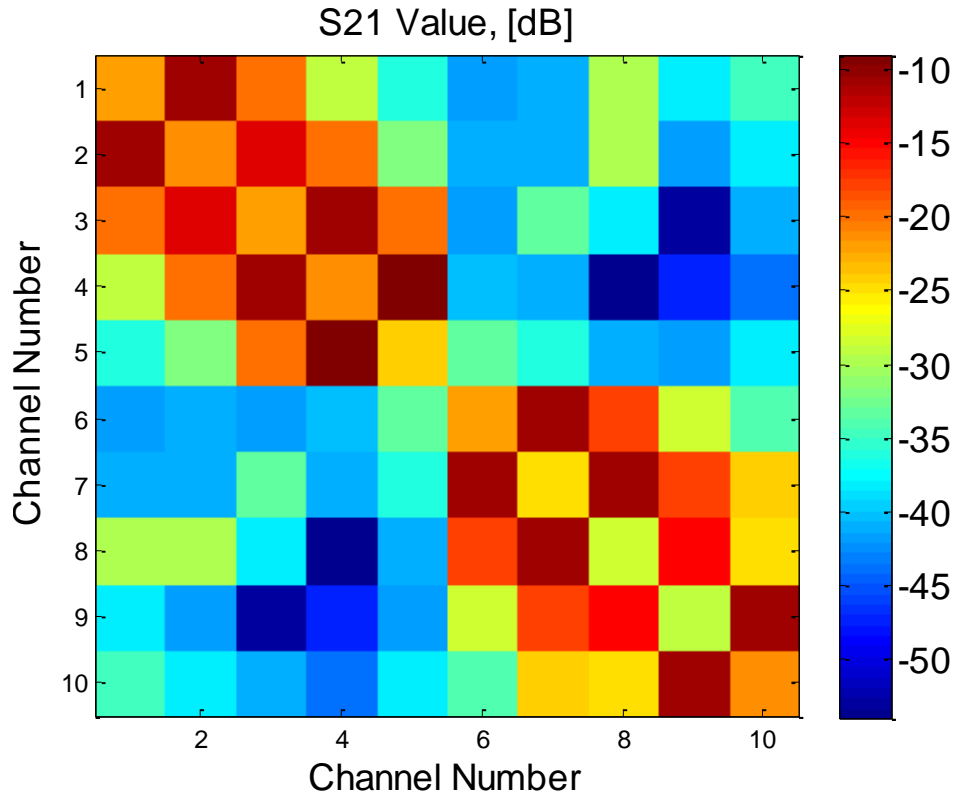


**FIG 5.3** Array configuration with animal holder—(A) 1.5-inch OD animal holder with nose cone inside and warm air tubing connection at the back. The nose cone will be applied with the anesthesia units; (B) Top five-channel DPP arrays; (C) ATC 15-pF back-distributed capacitors for a homogeneous field pattern; (D) Matching network; (E) Warm-air tubing; (F) Semirigid coaxial cable to the preamplifiers; (G) Small animal cradle with respiratory, temperature, and ECG sensors; (H) Inlet and outlet for the anesthesia gas

The array is connected to the preamp board and a 10 x 10 decoupling matrix is collected using S21 measurements obtained with the Agilent E5071C network analyzer. All of the measurements are averaged four times without the help of the low-input

impedance preamplifier and composed into a diagonal matrix based on electromagnetic reciprocity theory. The average nearest neighbor S21 value is -12.51 dB, with maximum decoupling of S21 = -9 dB and minimum of S21 = -15.1 dB. The average decoupling between next nearest neighbors is measured as S21 = -20.17 dB, with maximum decoupling of S21 = -18 dB and minimum decoupling of S21 = -25 dB. The crosstalk between the top and bottom five channels is all at least below -30 dB. The variability of the S21 value might come from the different element direction in space. Ten dual plane pair coils are manufactured on standard FR-4 PCB boards with solid flat surface but might not be concentrically wrapped around the cylindrical animal holder, and cause field interaction between adjacent channels might be different among the arrays. However, the average decoupling value of the nearest channel is sufficiently good to be -12.51 dB and definitely adequate decoupling with the help of low-input impedance preamplifiers. The decoupling S21 value is higher along the diagonal and shows two coupling groups as presented in Figure 5.4.

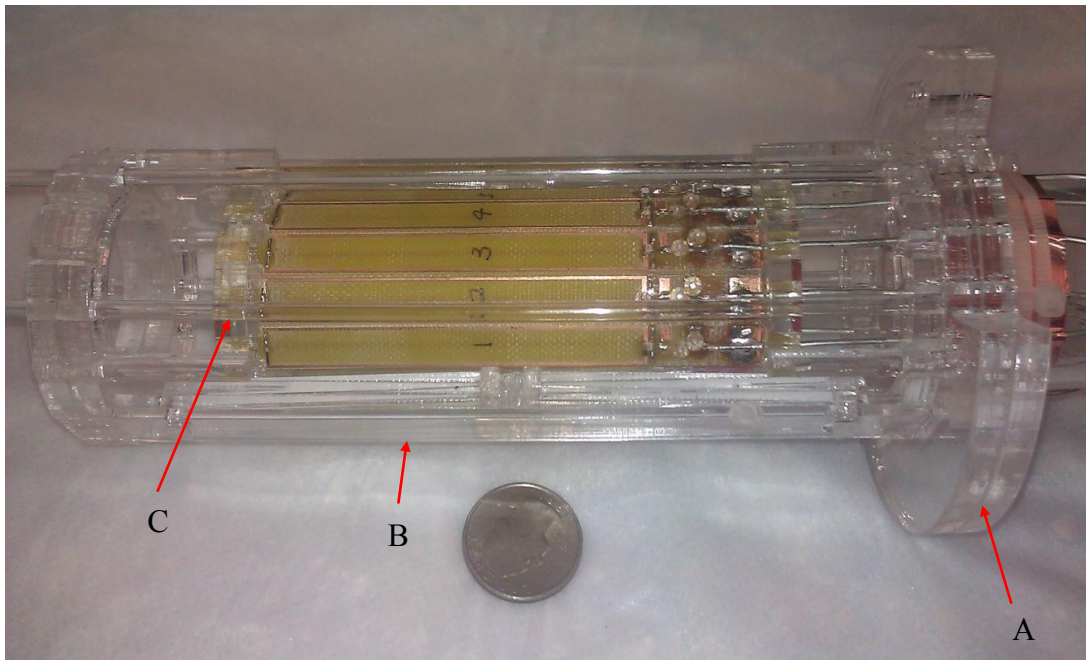




**FIG 5.4** Decoupling matrix of 10 channel dual plane pair elements. The color bar indicates the S21 value as decibels.

There is another coil holder have been made to change the spacing between top and bottom five subarrays. The coil physic dimensions of each element have also been modified to being plugged into the acrylic arc holder and the electric copper traces for RF current remains for the same performance as DPP element. The compressible mechanism could allow the user to adapt 10-channel mouse arrays tightly against the diverse animal shape and phantom. The RF coils holder could also center array and animal inside the transmitting linear birdcage with precise rotation angle and concentric position. The animal cradle with respiratory, ECG and temperature sensors could also been placed inside the holder for *in vivo* imaging purpose. The coils with holder are

posted as picture 5.5 below. The coil holder could be replaced easily to adapt to different dimension of DPP element that still mount on same squeezing mechanism.



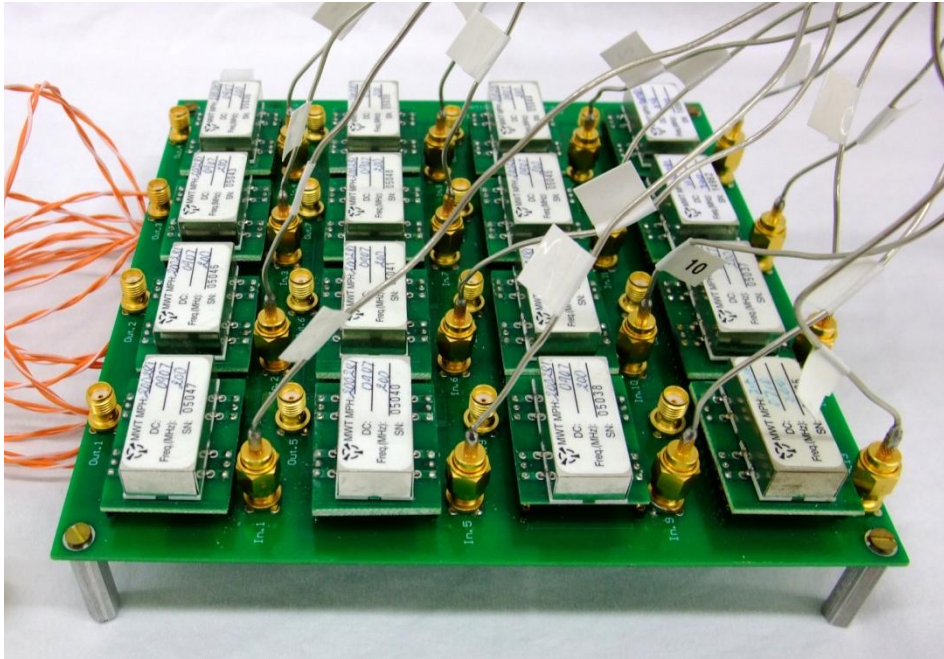
**FIG 5.5** An compressible animal holder are designed and constructed to hold the arrays with squeezing mechanism that adapt animal tightly against RF coil. (A) The ring shape plates could allocate holders with array inside the birdcage with precise rotation angle. (B) Squeezing mechanism helps each element adapt diverse animal shape. (C) Four rods locks the moving mechanism after all to stabilize the coil with holder.

### 5.3 Modular Low-Input Impedance Preamplifier Board

A 16-channel preamplifier board is also designed (drawn in EAGLE 5.11) and outsourced for manufacturing (two-layer board; PCBexpress/Sunstone Circuits, Mulino OR, USA). The circuit board layout is a mother-daughter board design to allow for switching the preamp modules quickly and SMB coaxial connections for any number of

RF coil array elements (up to 16). The low-input impedance preamplifiers (MPH-200281/P/N 01-61-020; Microwave Technology, Fremont CA, USA) provide near-zero impedance at the preamp side and transform the impedance through a matching network to high impedance at the coil side for eliminating induced currents in nearby elements. The low-input impedance preamplifiers provide 25~30 dB gain, 0.4 dB maximum noise figure, 20 dBm 1P3 and generally 2  $\Omega$  as low-input impedance at 200 MHz. The 16 channel preamplifier board (Figure 5.6) can support array systems up to 16 channels. A low-pass filter is applied on the DC source with an RF choke and a resettable thermistor PTC is used as a protection fuse on the preamplifier board that controlled the flowing current between 200 to 400 mA. Once the current is over current rating level, the electric resistance of PTC (PRG21BC4R7MM1RA; Murata Electronics North Americas, Inc, Smyrna GA, USA) will increase dramatically to thousands ohms to limit the current and protect the radiofrequency devices. The passive back-to-back diodes could be also applied across the input of preamplifier or at the end of transmission line to provide preamplifier protection and force a short circuit to high impedance the on coil end. Generally, the passive back-to-back diodes are applied across the tuning capacitors on the array element. However, the performance due to reducing the induced current is not added together by both the preamp decoupling and the passive detuned method. The preamplifier decoupling requires the matching network to perform a 50-ohm transmission line so that it acts as a high-impedance at coil end. So, the passively detuned diodes would not only shift the imaging mode from Larmor frequency but also loss the decoupling performance of preamplifier decoupling. So, the passive back-to-

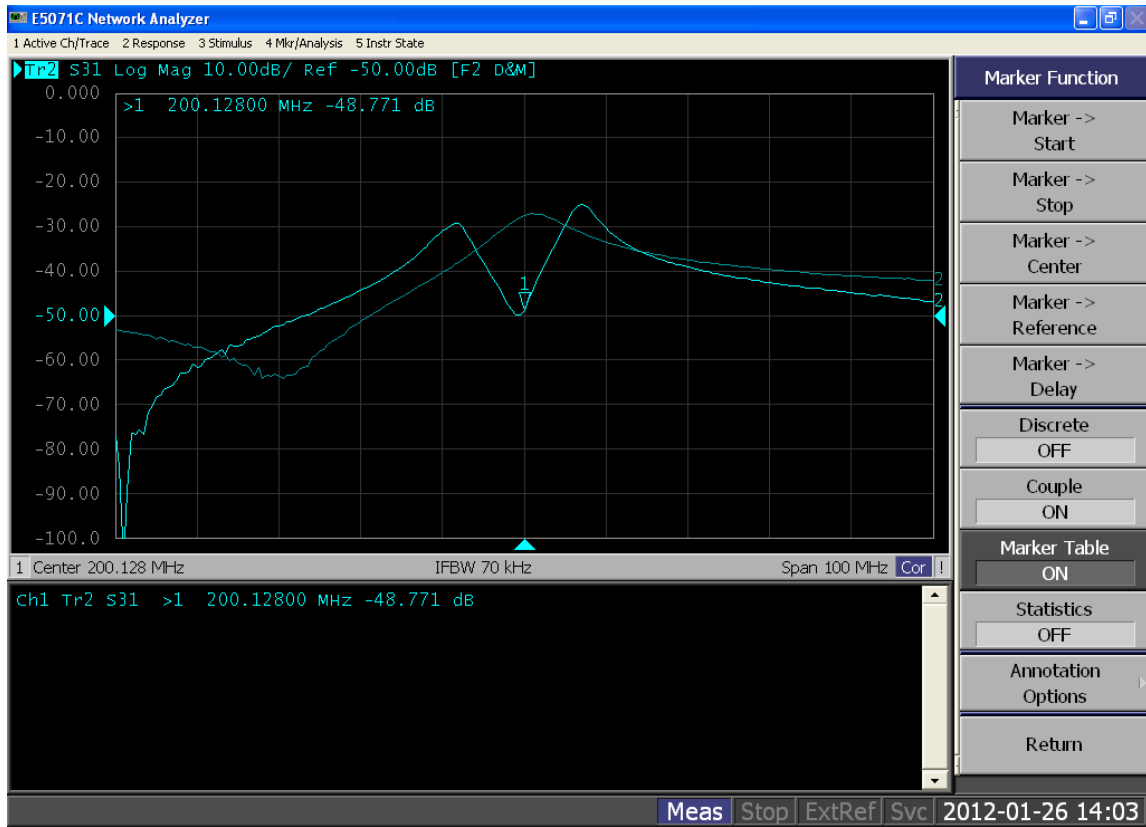
back diodes could be added across the preamplifier side of transmission line to force a truly short end and present high impedance at the coil end while the diodes are shorted by the induced current.



**FIG 5.6** 16 channel modular preamplifier board supports low-input impedance preamplifiers to provide high impedance on the coil end as a decoupling method and amplify the MR signal to the receivers. The SNA connectors with semirigid coaxial cable connect the I/O of the low-input preamplifiers. The RF arrays could also be replaced quickly by means of the semirigid cable with specific electrical phase length.

The performance of preamplifier decoupling is measured by double pickup loop with S parameter measurement on Network Analyzer. Initially, two channel loop arrays are built and constructed in house to demonstrate the isolation capabilities from low-input impedance preamplifier. The decreased field strength from double pickup loops between standard 50 ohm load node and low-input impedance preamplifier indicates the

decoupling for isolation on coil end. The decoupling value shown as Figure 5.7 decreases from -27 dB to -48.7 dB that provides -21.7 dB isolation at coil end.



**FIG 5.7** The decoupling value of low-input impedance preamplifier. The S31 drop from field strength of double pick up loop indicates the performance of preamplifier decoupling.

The 10-channel array decoupling from low-input impedance preamplifier has been measured on bench to demonstrate the coil isolation based on the double pickup loop measurement mentioned before. The values of preamplifier decoupling are channel by channel when the others nine elements are all connected to low-input impedance preamplifier units on board. The field strength between wideband 50 ohm calibration

load and low-input impedance preamplifiers are listed as Table 5.1. The decoupling value is calculated based on the field drop from the S21 measurement. All of the elements are well tuned to 200 MHz and matched to 50 ohm showing -20 dB at least in S11 measurement. The double pickup loop has been optimized overlapping area to have high isolation between each other. The averaging preamplifier decoupling value of 10 elements is -22 dB with 1.5 dB standard deviation.

**Table 5.1** Decoupling value of every element from low-input impedance preamplifier. Each value is S parameter measurement from network analyzer and the unit is decibel [dB].

<b>Channel #</b>	<b>1</b>	<b>2</b>	<b>3</b>	<b>4</b>	<b>5</b>
50 ohm load	-40.5	-38.6	-38.3	-39.4	-39.6
Preamplifier	-59.1	-59.7	-60.9	-63.1	-62.1
Decoupling	-18.6	-21.1	-22.6	-23.7	-22.5
<b>Channel #</b>	<b>6</b>	<b>7</b>	<b>8</b>	<b>9</b>	<b>10</b>
50 ohm load	-39.8	-38.3	-38.8	-36.3	-38.4
Preamplifier	-62	-59.3	-60.7	-57.5	-62.8
Decoupling	-22.2	-21	-21.9	-21.2	-24.4

Before the arrays imaging being made, the decoupling S21 parameters are measured between linear birdcage and every element. The 10-channel DPP mouse coils are placed inside transmitting linear birdcage. The S21 parameters are acquired between each channel and birdcage while the other coils are remained to connect to low-input

impedance for isolation purpose. The decoupling measurements are list as Table 5.2. The S21 values indicate the linear polarized field having higher coupling to parallel B1 field of coil element. Reversely, the S21 values present lower coupling when fields from linear birdcage and RF coil are orthogonal.

**Table 5.2** Decoupling S21 parameters between linear birdcage and 10 channel arrays

<b>Channel #</b>	<b>1</b>	<b>2</b>	<b>3</b>	<b>4</b>	<b>5</b>
<b>S21 value (dB)</b>	-17.6	-36.3	-34.9	-44.6	-20.6
<b>Channel #</b>	<b>6</b>	<b>7</b>	<b>8</b>	<b>9</b>	<b>10</b>
<b>S21 value (dB)</b>	-18.9	-45.7	-39	-34	-17.8

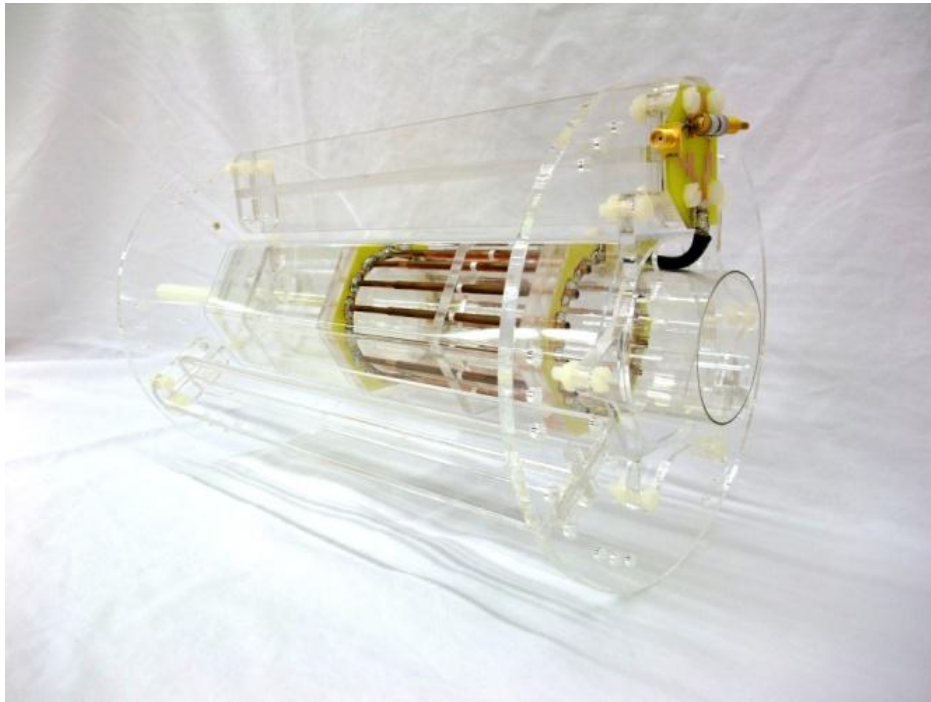
The induced current on each element from transmitting birdcage should be even smaller when all of the ten coils are all connected to isolation preamplifier at imaging. The isolation preamplifier would help element to reduce coupling and add up -20 dB isolation.

## **5.4 Transmit Coils**

### **5.4.1 Homogenous Transmit-Only Linear Coil for Parallel Imaging**

As mentioned previously, a particular need exists for a homogenous transmit coil to ensure that the DPP is decoupled during transmit – that is, that equal flux passes

through the two halves of the DPP. Figure 5.8 shows our transmit-only coil when the copper shielding (18  $\mu\text{m}$ , AC1820000R; DuPont Pyralux, Research Triangle Park, NC, USA) is removed. A 60-mm diameter, 16-rung, high pass birdcage is constructed using precise fabrication techniques and a symmetric “trombone” tuning design ([79], [80]).

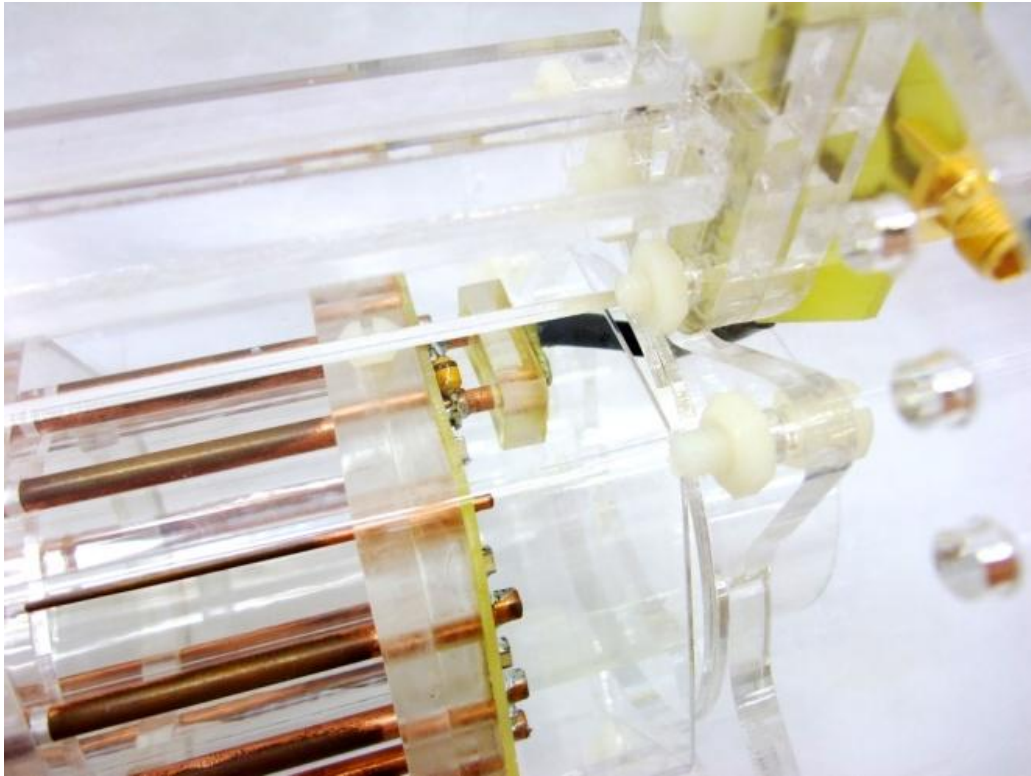


**FIG 5.8** The copper shielding of our linear transmit-only coil is removed to show the internal structure. The custom-made hexagonal former housed the 16-rung transmit trombone coil, including the frequency-tuning mechanism. The hexagonal former also served as the support of the copper shielding. The PETG tube (ID/OD: 2.438 in/2.5 in.; VisiPak, Arnold MO, USA) is installed inside of the transmit coil to prevent direct contact with specimens. The Nylon screw rod shown on the left side of the figure is used to tune the length of the rungs. The matching network shown on the right side of the figure is installed outside of the hexagonal form and at  $90^\circ$  to the main axis to reduce coupling to the receiving coil (not shown here).

Each length-adjustable rung is consisted of one fixed copper tube (ID/OD/length: 0.125 in/0.156 in/3.8 in.; K&S Engineering, Chicago IL, USA) and one mobile copper



tube (OD/length: 0.156 in/3.8 in.; K&S Engineering), which are coupled together. We carefully chose the inner diameters, the outer diameters, and the length to ensure constant contact among each pair of the fixed and the mobile rungs. These 16 fixed pipes and 16 mobile pipes are individually soldered onto two end rings made by LPKF. Each end ring is mechanically strengthened by two layers of laser-cut ¼-in.-thick acrylic sheets to maximize stability and alignment. To provide extra mechanical stability and to help generate repeatable results, an over-engineering approach is used. One extra laser-cut ¼-in.-thick acrylic sheet is installed on the fixed rungs approximately in the middle of the birdcage coil to provide extra support. To tune the frequency of our birdcage coil, a single nylon screw rod (1/2 in.-13) and two nylon nuts (1/2 in.-13) are used to fine tune the length of the rungs. To avoid the coupling induced by the matching network, the matching network is placed outside of the copper shielding. The matching network is directly connected into two rungs through RG-58 cable and a custom-made copper plug. This design of the copper plug allowed us to quickly switch between different types of matching networks and linear and quad-rapture modes with limited signal loss. The active detune network is placed on the end ring between the two legs of the custom-made copper plug as shown in Figure 5.9. A custom-made hexagonal acrylic former (3.6-in. OD) is used to house the transmit coil and served as support for the copper shielding. We chose to use the hexagonal form because it is easier to extend our design to multiple-specimen scanning in the future. The rat-size birdcage has shielding on the outside, which degrades the SNR but still provides a homogenous field the volume coil.

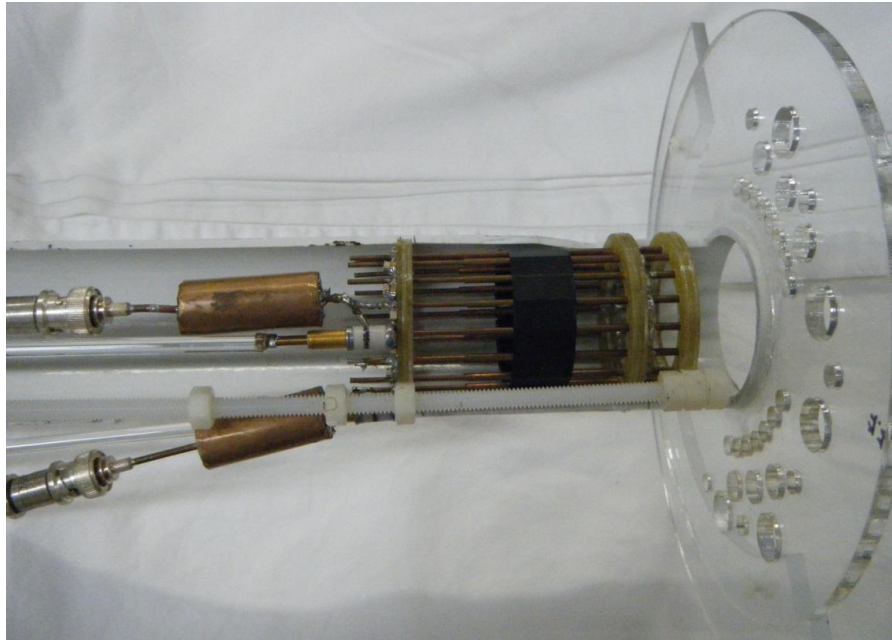


**FIG 5.9** The custom-made plug is made by two 1-in.-long copper tubes, which are the same as the ones used for the mobile pipes of the transmit coil, one small piece laser-cut  $\frac{1}{4}$ -in.-thick acrylic sheet, and one 1.5in. RG-58 cable. The openings of the two fixed copper tubes are mechanically treated to serve as the socket with a tight fitting. This design allowed us to quickly exchange different types of matching networks without sacrificing the transmit power.

#### **5.4.2 Description of Additional Volume Coils Constructed and Applications**

As a side note, during my study at Texas A&M University, several quad mode birdcages were built for different sizes of animals and applications. These birdcages were built to best fit the animal size and provide better sensitivity. Similarly, a quadrature mouse trombone birdcage (35-mm ID) has been constructed in the same way in house to compare SNR with the array coil imaging (as Figure 5.10). A sheep head size quadrature birdcage coil has also been manufactured as a volume coil at magnet 40 of the MRSL. The mouse- and rat-size coils both have adaptor plates for imaging at

different bore-size magnets (33 cm and 40 cm) at the MRSL. The homogeneity and SNR of the mouse coil has been tested and performs as well as the commercial Varian mouse coil.

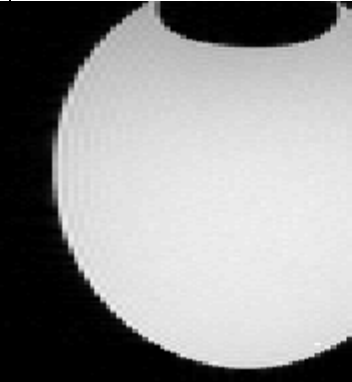
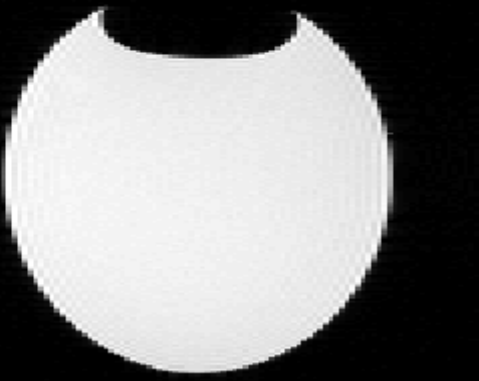




**Figure 5.10** Quad mode trombone birdcage for mice imaging

The SNR comparison between in house rat birdcage and commercial Varian coil are acquired as same imaging parameters setting and experiment criteria. The SNR is higher in sagittal view simply because the voxel size is smaller in transverse slice and the SNR reduce is proportion to voxel size increment as MRI theory. Both coils perform homogeneous field pattern at both view that is critical as volume coil characteristics and the in-house quadrature birdcage coil show even same SNR level as Varian coil in both

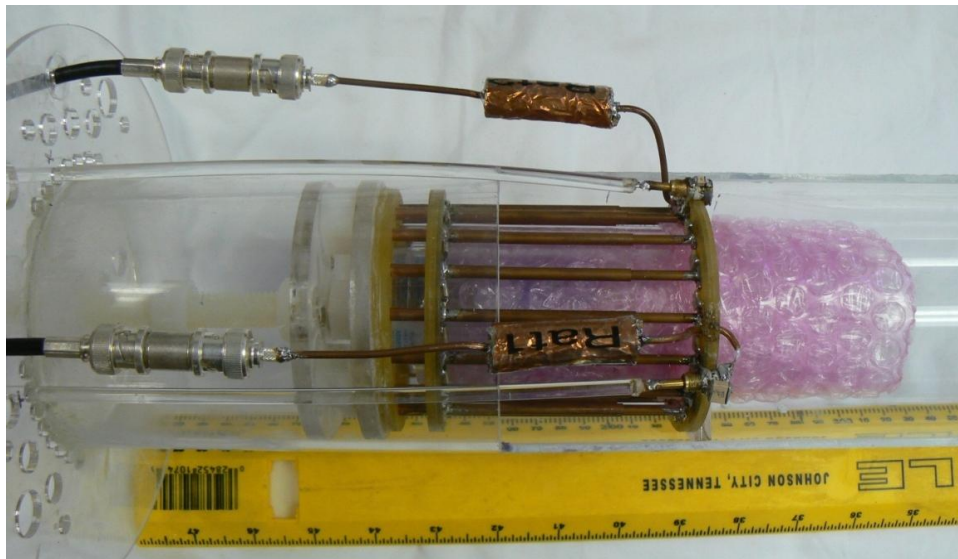
views. Both imaging and SNR analysis are posted in Table 5.3 to demonstrate coil performance.

**Table 5.3** SNR comparison between in house rat birdcages and commercial Varian coil.

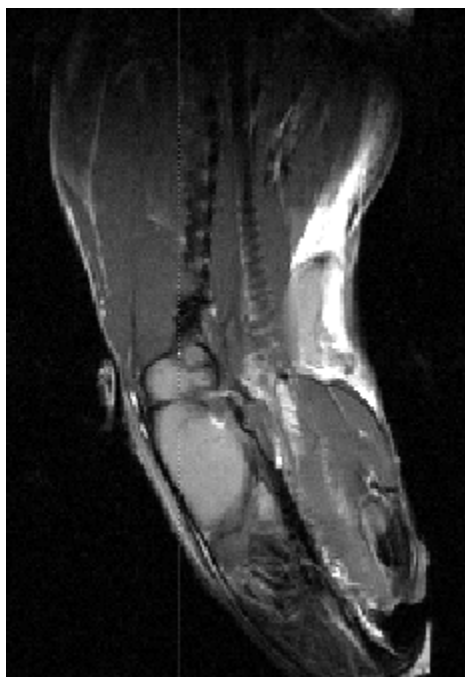
Coil	Varian Coil	In house Birdcage coil
Trans Imaging		
SNR	236.6	242.55
Sagittal Imaging		
SNR	638.1	643.6

The rat-size quadrature birdcage also provided another way for imaging different animal sizes. The 60 mm quadrature mode birdcage coil without RF shielding outside is shown in Figure 5.11. The different stage of ischemic stroke analysis on a rat is performed to demonstrate the capability and application of the rat coil. The sagittal

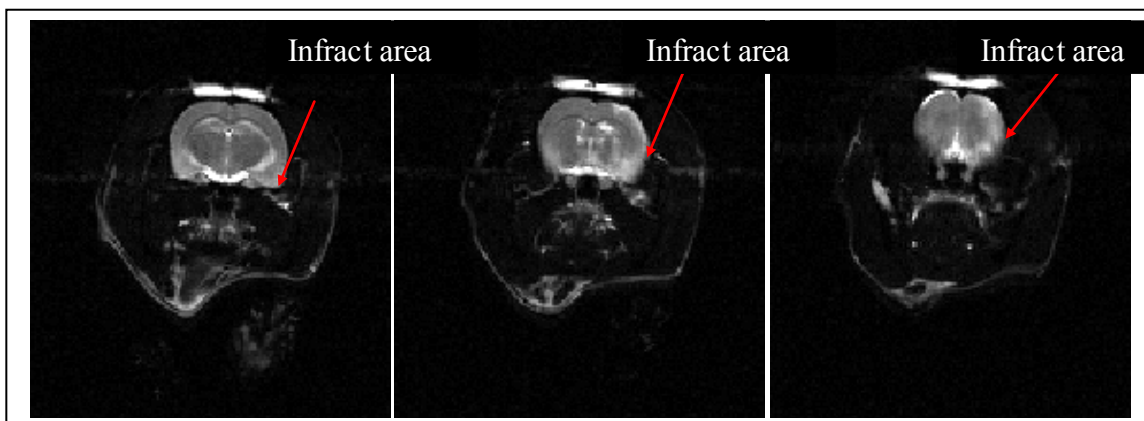
imaging as presented in Figure 5.12 is obtained to define slice planning on a rat brain for infracts area inside the rat's brain. Next, the multislice diffusion-weighted image set are obtained to display the infract area of ischemic stroke in the rat brain as shown in Figure 5.13. The diffusion-weighted imaging shows the brain structure based on the fluid movement from diffusion phenomena.



**Figure 5.11** The 60 mm quadrature mode birdcage for rat imaging applications.

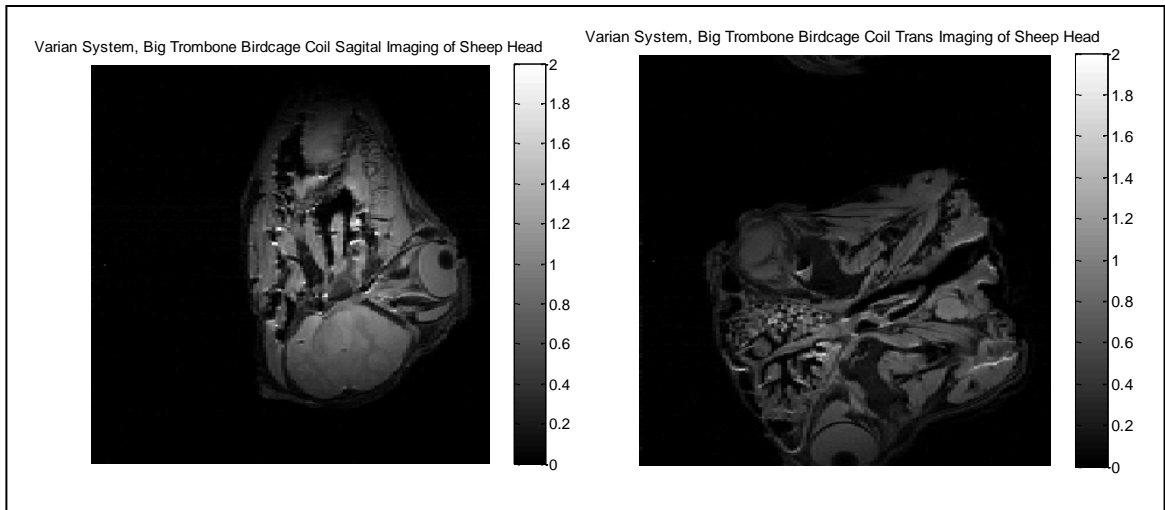


**Figure 5.12** A sagittal scan of a rat for brain slice planning.



**Figure 5.13** A multi-slice diffusion weighted imaging set of a rat brain.

Since the good homogeneity of the quadrature birdcage, the sheep head size high-pass birdcage was built as the same way to image large object.

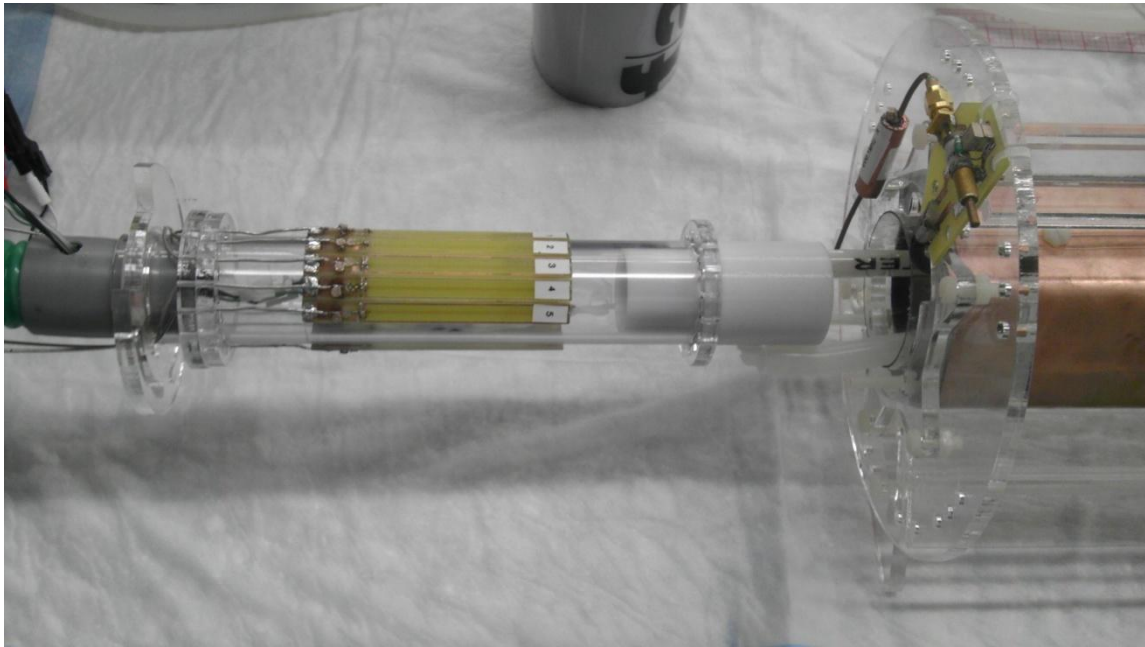


**Figure 5.14** A sagittal and transverse imaging sheep brain from 23.5cm birdcage coil.

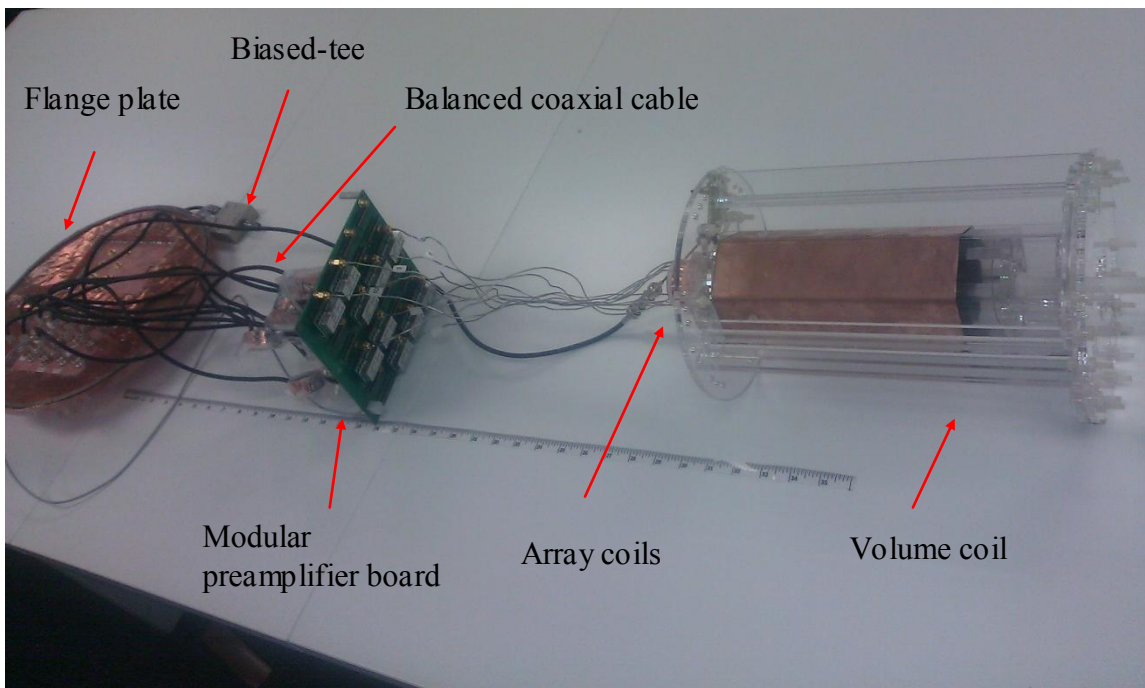
### 5.5 Compact Mouse Coil System Integration

Combining the RF arrays, birdcage coil, preamplifier board, animal holder with gating sensors, and anesthesia gas in the imaging setting are presented without loading an animal inside in Figure 5.15. The animal holder with array coils combined could slide into the volume coil smoothly and be concentric with the phantom, arrays, and birdcage. The animal holder is also able to rotate within 90 degrees and lock the holder on the birdcage for precise positioning and direction, even with a different experiment. The warming air is sent from behind and pushing anesthesia gas out through the nose cone at the front end of animal holder. The compressible animal holder and 10 channel embedded array coils are also perform iso-center inside the volume coil as Figure 5.16. The modular preamplifier board is connected to array and output echo through balanced coaxial cable to flange plate shielding of scanner.





**FIG 5.15** The image setting of compact RF arrays configuration with small-animal anesthesia and gating system.



**FIG 5.16** The image setting of compact RF arrays system with volume coil, RF array coils, modular preamplifier board, balanced coaxial cable, biased-tee for actively detuned volume coil and flange plate shielding with multiple RF adaptors for scanner.



## CHAPTER VI

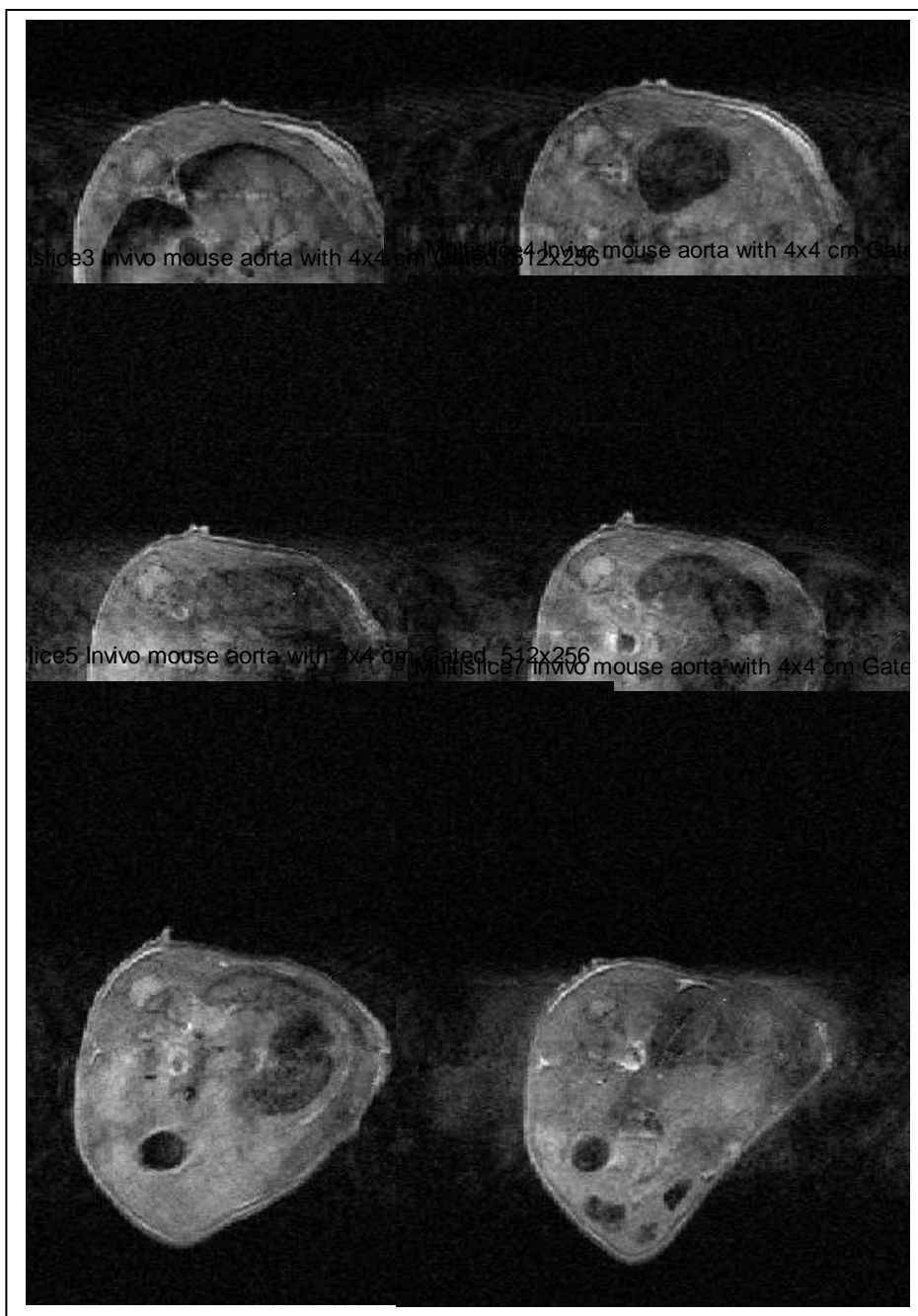
### INITIAL RESULT, CONCLUSION AND FUTURE WORK

This chapter presents the initial results and efforts in combining the animal-specific needs (anesthesia and gating) described in CHAPTER IV with the parallel imaging system tailored for mice described in the previous chapter. The effects of ECG and respiratory gating were investigated first with a volume coil and the effectiveness of the array coil configuration was first tested in single-channel mode on phantoms and euthanized mice. Based on this preliminary data, future work and design modifications are discussed and conclusions drawn.

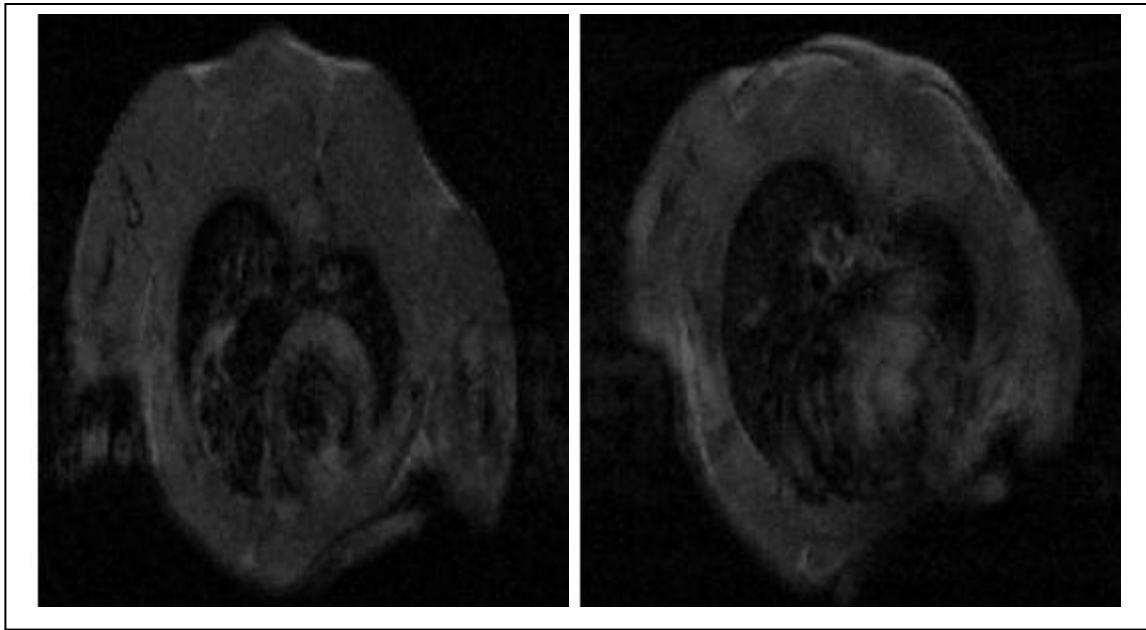
#### **6.1 *In vivo* Mouse Imaging with 35 mm Volume Coil**

As part of preliminary testing of the *in vivo* gating capabilities described in CHAPTER III, images with and without ECG gating and respiratory gating were acquired to demonstrate the influence of the respective motion artifacts on imaging quality. Figure 6.1 shows the multi-slice abdominal region of mouse suffering from respiratory motion, despite our original intuition that ECG gating alone was sufficient. *In vivo* imaging was performed to locate the abdominal aorta with ECG gating only and still suffered from respiratory motion artifacts. Figure 6.2 shows images with respiratory gating only and without ECG gating. The motion artifact appears clearly across the cardiac region without ECG gating. An ECG and respiratory gated image is shown in

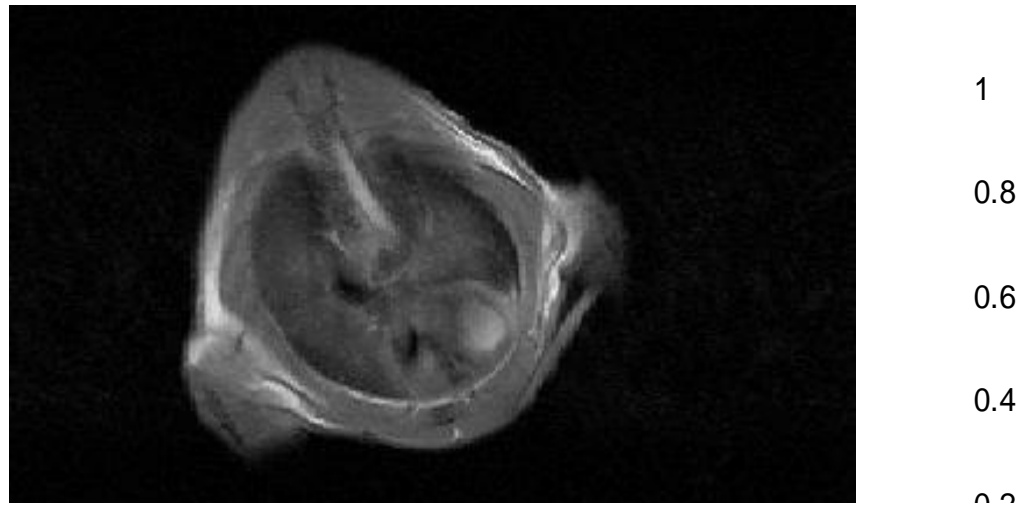
Figure 6.3, free from motion artifact. The motion artifact is seen in the phased encoding direction (the horizontal direction in Fig. 6.1). Generally, the motion artifact appears in the phase encoding direction. Because the acquisition window (digitalization) of frequency encoding is short compared to the overall phase encoding table, the body movement generally causes less motion distortion within the millisecond range. Since the data point in the phased encoding direction, however, was collected between the relaxation processes within a (relatively) long repetition time (TR), the body movement might shift within several hundreds of milliseconds or even a second to cause distortion in the phase encoding direction. Similar approaches have been published in instructional manuscripts as illustrated by the following paragraph: “Swapping Phase- and Frequency-Encoding Axes. If ghosting along the phase-encoding axis obscures a key structure, the phase- and frequency- encoding axes can be switched so that the artifact is perpendicularly redirected away from the key structure. This may change imaging time if the field of view (FOV) is rectangular.” [81, 82]



**FIG 6.1** ECG gated *in vivo* imaging without respiratory gating in the abdominal region of the mouse.



**FIG 6.2** Respiratory gated *in vivo* imaging without ECG gating in the cardiac region of mouse. Parameters are set for high resolution with thin slice thickness for fine cardiac structure with 1000/13.2 TR/TE, FOV 4x4 cm with matrix size 512x256, and slice thickness 0.3 mm with 2 mm imaging gap.

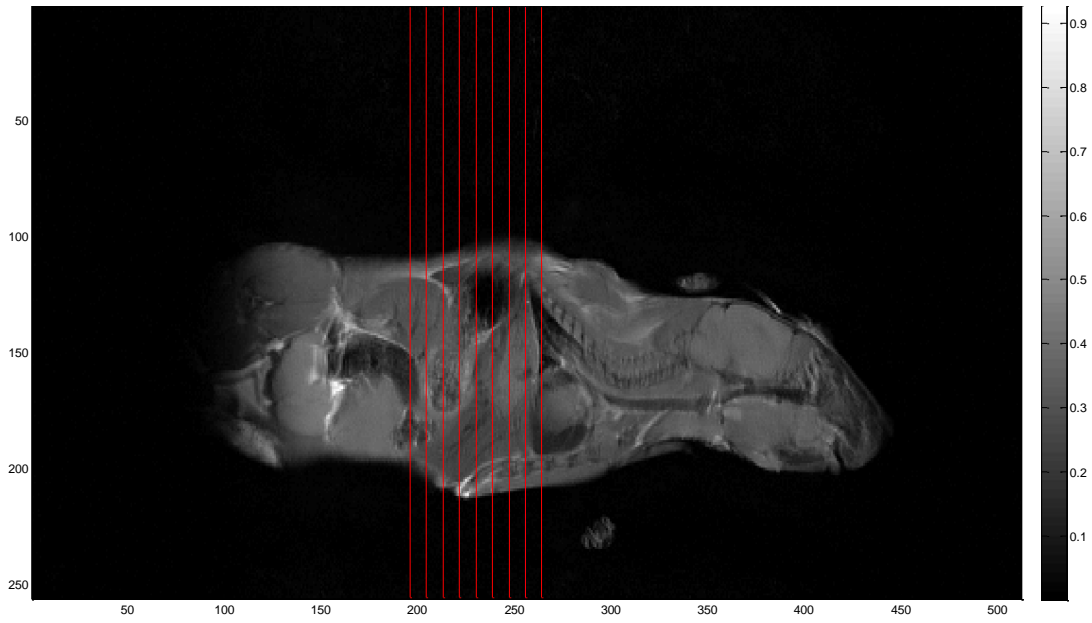


**Figure 6.3** An ECG and respiratory gating image of cardiac region shows free motion artifact.

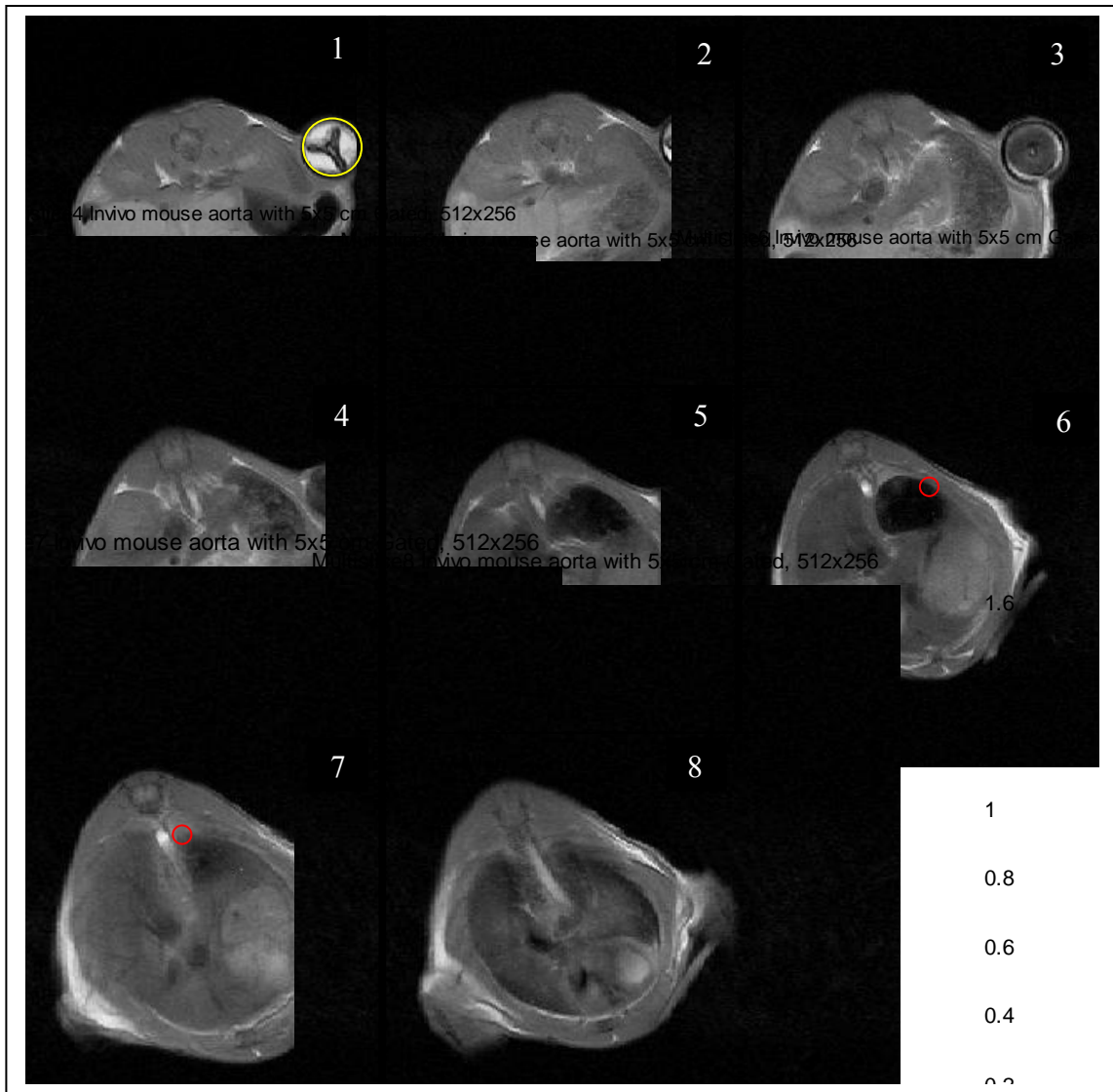
To obtain the geometric information regarding the abdominal aorta (the application of interest to our collaborator), the time span of each process in the SEMS

sequence is set up for a short echo time (TE =13 milliseconds) and high in-plane resolution . The ramp up time of the gradient (t<sub>ped</sub>) was shortened to decrease TE but increase the gradient strength.

The specific animal model developed by our collaborators was an Angiotensin- $\Pi$  (Ang -  $\Pi$ ) infused Apolipoprotein E (ApoE) -/- mouse model for studying the development of aortic aneurysms. The modified mouse was anesthetized by isoflurane during the scan. The imaging parameters were 1000/13.2 ms TR/TE,  $N_{\text{phase enc}} \times N_{\text{readout}} = 512 \times 256$  with 4 x 4-cm FOV, and 0.8-mm slice thickness with in-plane resolution 156  $\mu\text{m} \times 313 \mu\text{m}$ . The 90- and 180-degree RF pulse were shorted to 1 ms, with increased RF power to compensate for the reduced pulse width. The multi-slice setting was set to scan eight slices with a 2mm gap. The scan was gated to the ECG and respiratory signals from the mouse, eliminating motion artifacts. The sagittal slice (Figure 6.4) is displayed to show the slice planning of the multi-slice scan covering the area between the diaphragm and the top of the kidney. The multi-slice imaging set of *in vivo* abdominal scans are presented as Figure 6.5. The in-plane resolution of the axial imaging set was 98 x 98  $\mu\text{m}$  in the transverse slice direction. The picture 8 in Figure 6.5 covers the region just above the diaphragm that includes the cardiac structure, with no motion artifacts visible.



**Figure 6.4** A sagittal scan of a mouse for abdominal aorta slice planning

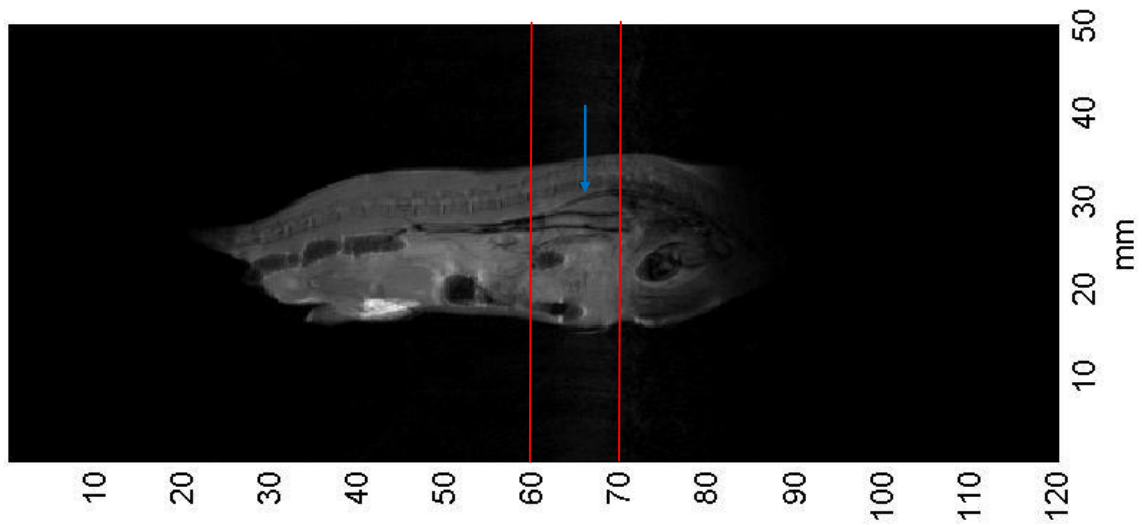


**Figure 6.5** *In vivo* multislice spin echo imaging for abdominal aorta with cardiac gating. The red circle indicates the abdominal aorta and the yellow circle indicates the pump to release medicine gradually into the mouse. The imaging gap is 2 mm with a slice thickness of 0.8mm.

Another imaging set was obtained, focusing on aorta imaging. The slices were a different axial offset but the same parameter settings. A sagittal image was acquired first to plan slice offsets by locating the abdominal aorta using a Matlab reconstruction shown

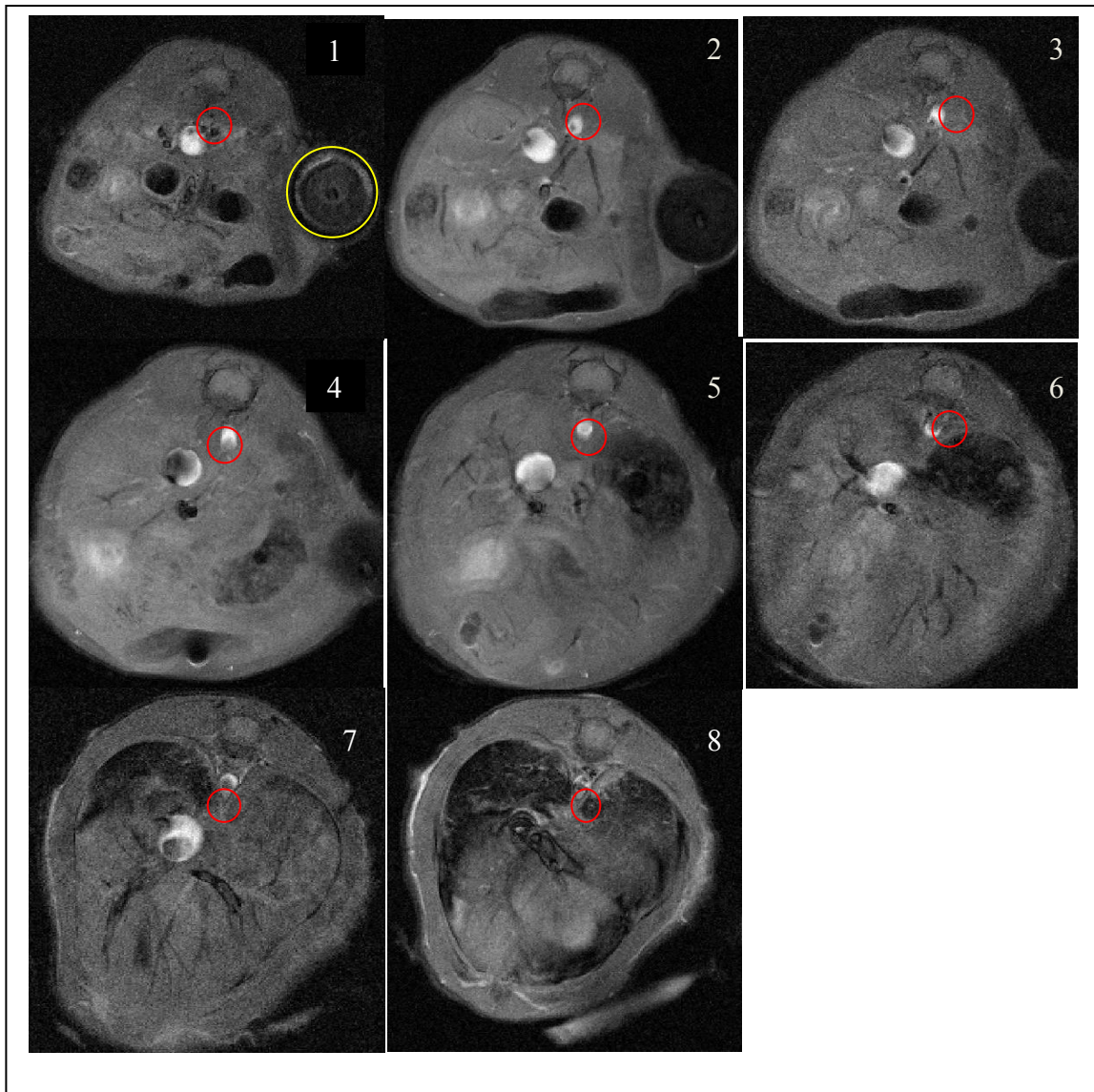
in Figure 6.6. The span between the red lines indicates the region of interest for the abdominal aorta study. The aneurysm region was predicted to be around 7 mm in length.

The axial slice offset in Figure 6.7 was 1 cm, and the imaging set was acquired with both ECG and respiratory gating signals as an external source to the scanner.



**Figure 6.6** Sagittal slice with cardiac gating to plane slice offsets. The red lines display the 1 cm imaging span to determine the abdominal aorta indicated by the blue arrow.





**Figure 6.7** Abdominal aorta with 1000/13.2 ms TR/TE, NEX = 4, 0.5-mm slice thickness, 36 x 24- cm FOV with 512 x 256 matrix size (resolution 70  $\mu$ m x 94  $\mu$ m), 100,000-Hz spectral width, and 5.12 ms acquisition time. The red circle indicates the abdominal aorta region and the yellow circle represents the pump-inducing aneurysm inside the mouse. The slice offset by imaging number is 0, 2, 2.5, 4, 6, 7.5, and 1 mm, which directs scanning from the kidney toward the diaphragm.

At the writing of this dissertation, array imaging has been accomplished on only a phantom and a euthanized mouse. This is because the array has not been used with


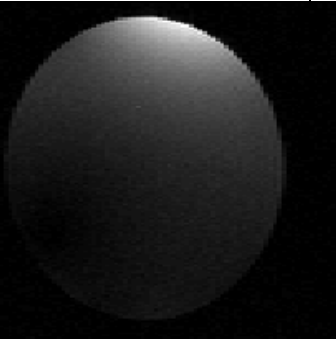
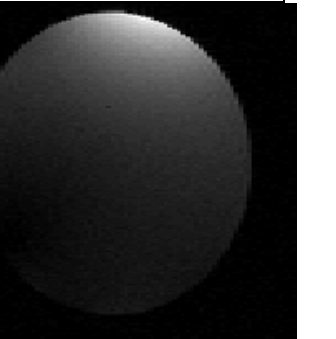
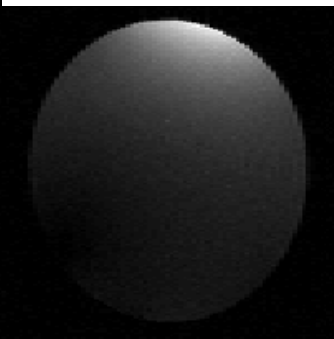
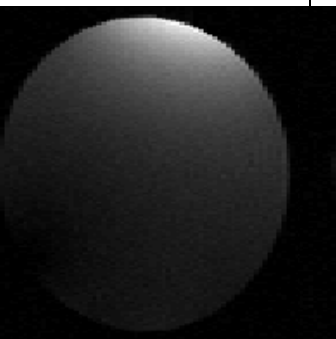
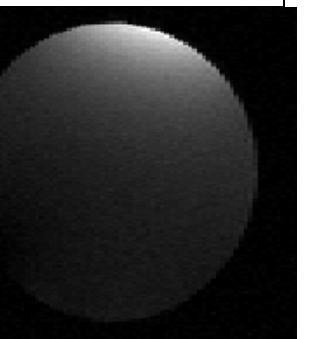
multiple receivers in a truly “parallel” acquisition. Each *in vivo* gated scan acquired above took approximately 25 minutes for 4 averages. Repeating this for each of the ten elements of the array would keep the animal under anesthesia for too long. Since this is the case, time limitations prevent imaging a live animal, as was accomplished above. The above results, however, clearly demonstrate the capability to acquire *in vivo* high resolution images of the mouse. The results below will demonstrate the imaging results from the array.

## **6.2 Ten-Channel DPP Arrays with Volume Coil Imaging**

A phantom was built consisting of 1 gram/liter copper sulfate and 2 gram/liter salt solution to mimic mouse loading and obtain an imaging profile of every element with a uniform phantom. The phantom was held concentrically within the birdcage coil by the animal holder to guarantee equal distance and potential imaging depth for every element. Multi-slice spin echo images were obtained to indicate an acceptable dual-plane pair imaging profile along the long axis of the element. Each image was 1 cm away from the adjacent image in order to cover the full imaging length of 6 cm along the 7-cm long DPP element. The reasonable imaging profile also indicates the proper back distributed capacitor value that affects the localization pattern of the dual plane pair element along the coil length. A set of multi-slice data from a single element is shown in Figure 6.8, illustrating the homogeneity along the long axis of the element. The outer two imaging

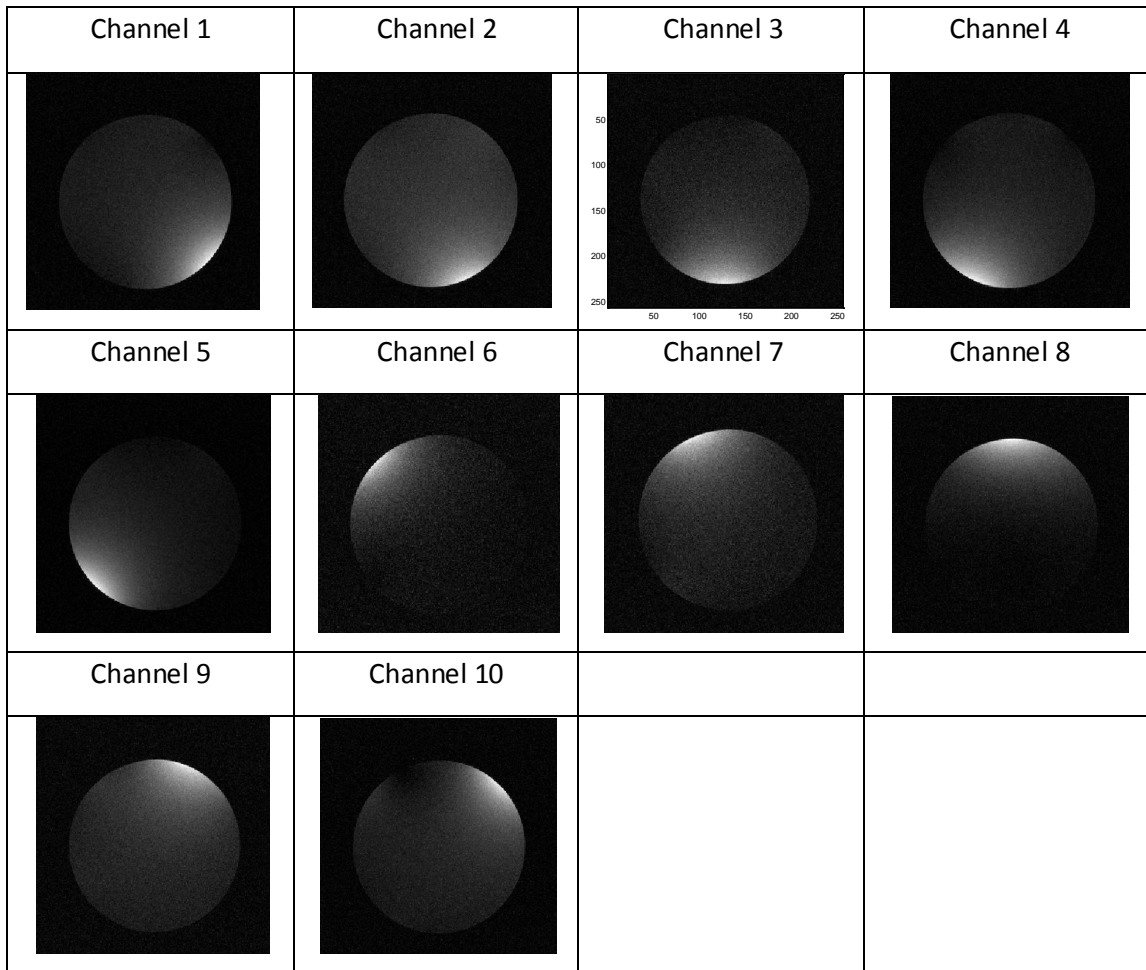
slices are out of the coil length and visible region so the SNR degrades significantly and is not chosen to be displayed

Individual axial images of every channel were also acquired to illustrate the localization of the imaging profile and decoupling provided by the low-input impedance preamplifiers. The axial images were all obtained with 1000/30 ms TR/TE,  $N_{\text{phase enc}} \times N_{\text{readout}} = 256 \times 256$  with a 4 x 4 cm FOV, 2 mm thickness, single scanning average, 5.12 ms acquisition time, and 50,000-Hz spectral width. The profiles were combined using sum-of-squares reconstruction method to reconstruct the full axial slice. Each profile image was calibrated and normalized by its maximum intensity to eliminate the different conditions of different tuning and matching ports, different cable attenuation loss, and noise level. The linear birdcage simultaneously obtained an axial slice image with the exact same parameters at the same slice offset to indicate the SNR improvement from the array coils and shows no coupling between the volume coil and arrays. If coupling exists between the array and volume coil, the array region would darken as over tipping occurred. In addition, the standard quadrature mouse birdcage coil, manufactured in house with a 35 mm inner diameter, was also used to compare the SNR with the mouse array design. The SNR was calculated as averaged signal intensity (signal area) divided by standard deviation of the noise region (corner area). The intensity value is averaged within every 3 x 3 pixel matrix. And, the noise region is selected at the corner of each image.

Offset (cm)	1	2	3
			
Offset (cm)	4	5	6
			

**FIG 6.8** A set of multislice spin-echo images along the coil length. The offset in the transverse direction is 1 cm span from the matching network toward long end of the coil. The imaging set indicates the coil profile along the frequency encoding direction.

The patterns from each of the 10 elements, shown in Figure 6.9, illustrate the localization and imaging depth of the elements. The 10 channel DPP elements are separated into 5 channel top-to-bottom subarrays. The phantom is precisely located at the center of the animal holder and birdcage coil such that each element should have an equal imaging depth. For cardiac imaging applications, the animal holder could be even thinner to allow increased imaging penetration depth.

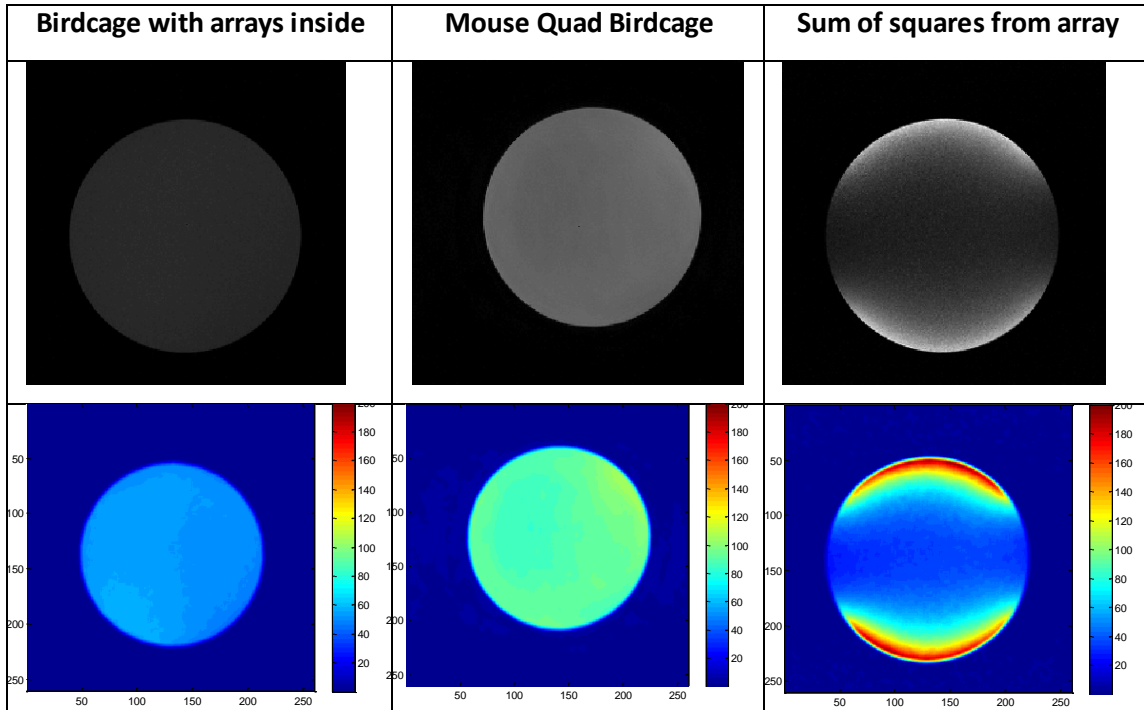


**FIG 6.9** This image set represents the field pattern and localization of every coil as cylindrical arrays.

The sum of squares reconstruction from the element profiles as compared to the volume coil with regard to SNR is shown in Figure 6.10. The center region of the reconstructed image from the 10-channel array displays 70% of the rat-size volume coil imaging intensity. Our SNR map is calculated as averaged imaging intensity divided by standard deviation of noise region. The averaged intensity is using convolution to average 3 x 3 pixels as the signal level, and the edge of the circle is averaging with the noise level within the 3x3 pixels that actually reduce our maximum SNR value. So, the

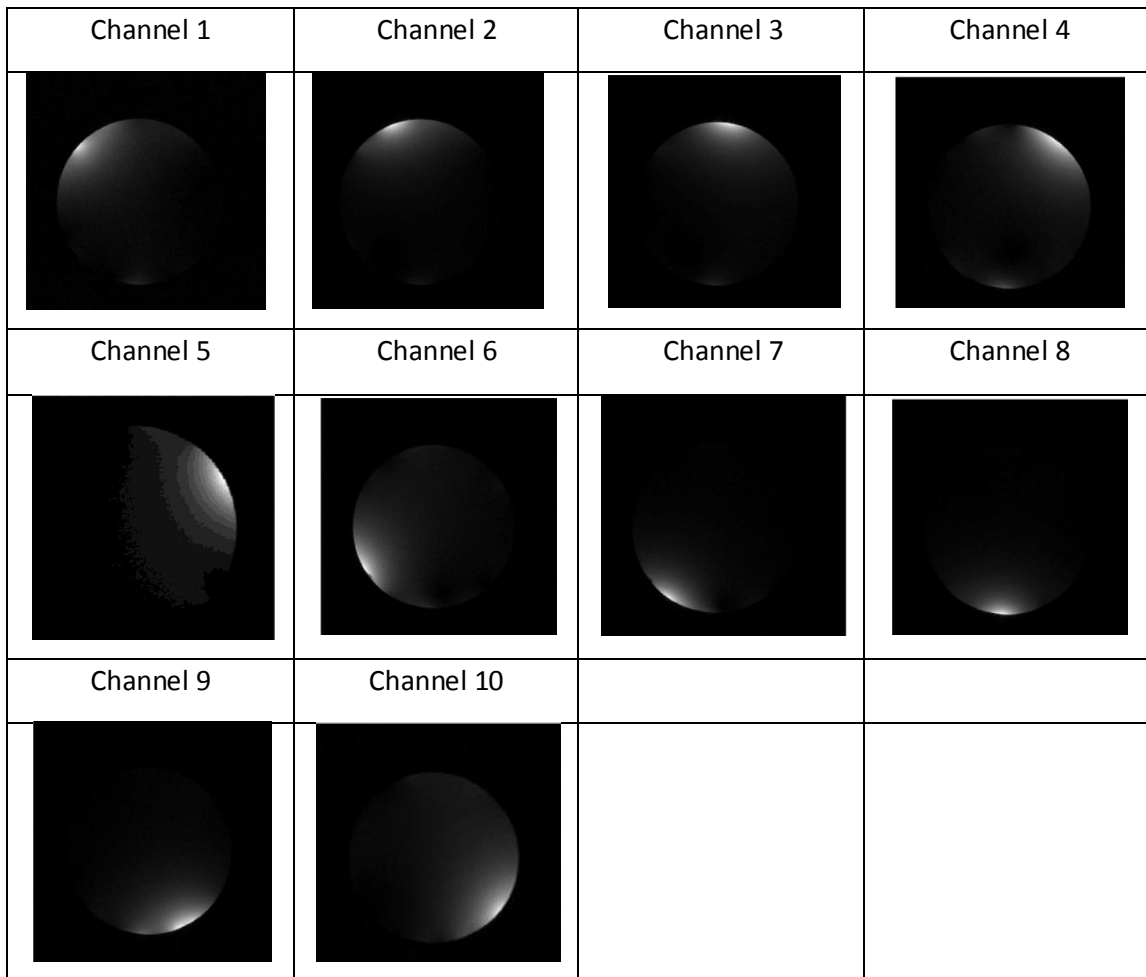
SNR level is a ramp up from the noise region across the edge of circle toward the center. Without averaging the 3 x 3 pixels region as intensity, the SNR could be higher by simply dividing intensity of every pixel with standard deviation of noise. Meanwhile, the birdcage intensity evaluated by the same SNR calculation is supposed to be accurate and has not been found to present a problem for indicating the actual performance. Because the birdcage profile is homogeneous, every pixel should have same intensity level. Generally, there is no difference when evaluating birdcage sensitivity based on the pixel at the center or the edge.

The homogeneity of the rat-size volume-coil image shown in Fig. 6.10 also demonstrated the lack of coupling between the array coils and the transmit birdcage coil while the array coils were inside. Both mouse and rat size volume coil imaging are presented with the same colorbar scaling as the sum of square reconstruction imaging for clear sensitivity demonstration. The sum of square imaging demonstrates the expected decay of the imaging profile towards the center, with SNR gains over the 3.5cm mouse coil only on the perimeter of the phantom.



**FIG 6.10** The birdcage images as reference indicate the higher SNR from the sum-of-square of 10-channel array imaging. The top row is the original images and SNR maps in bottom row show the same color bar level to display intensity difference among the imaging modalities. The corner number of each volume coil indicates average SNR at the center of images. The same number in array imaging presents maximum SNR value.

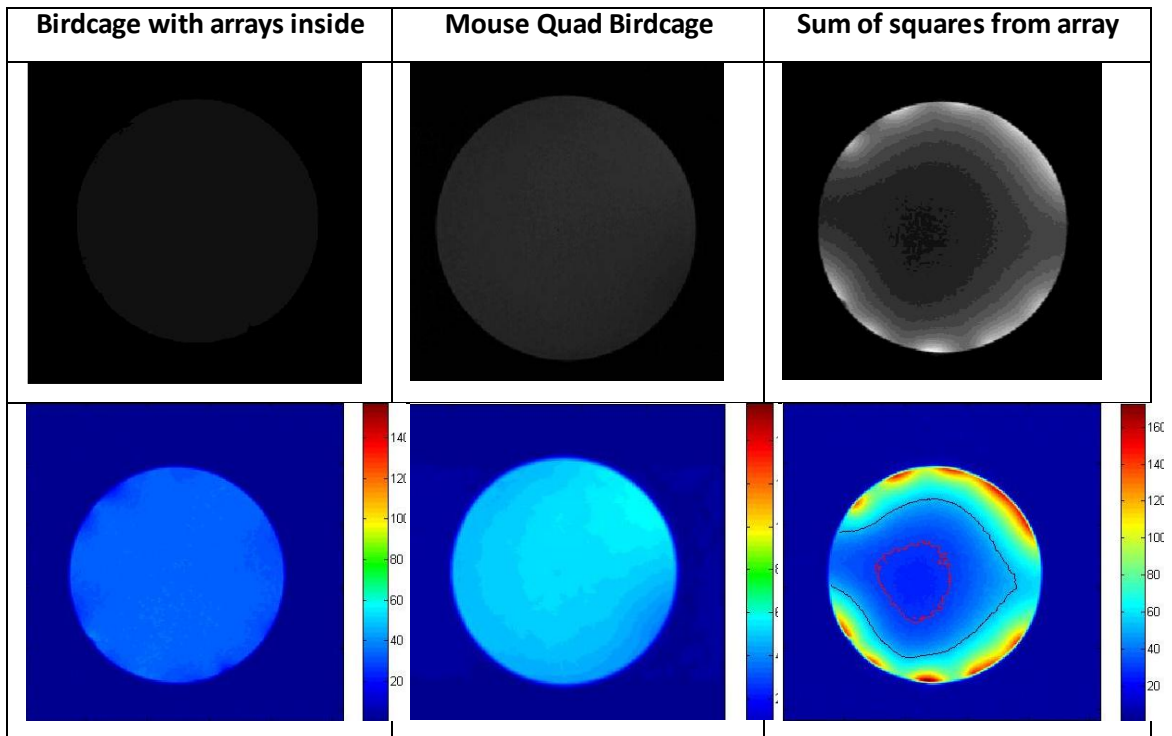
Because the array element was almost one coil width away from the phantom (acrylic tubing thickness plus phantom holder), the imaging depth could be improved by placing the element closer to the phantom. Therefore, a “compressible array” configuration was constructed to tightly fit the coil elements against diverse animal shapes and different sizes of phantoms. This was discussed in CHAPTER V. The profiles from the compressible array were acquired in the same way as the cylindrical array to study the imaging depth and sensitivity region. The profiles are shown in Figure 6.11.



**FIG 6.11** This image set represents the field pattern and localization of every coil of the compressible array elements.

The sum of squares reconstructed image was obtained from the profiles to demonstrate the sensitivity gains in the region of interest. The sensitivities of the volume coils and array are shown in Fig. 6.12.





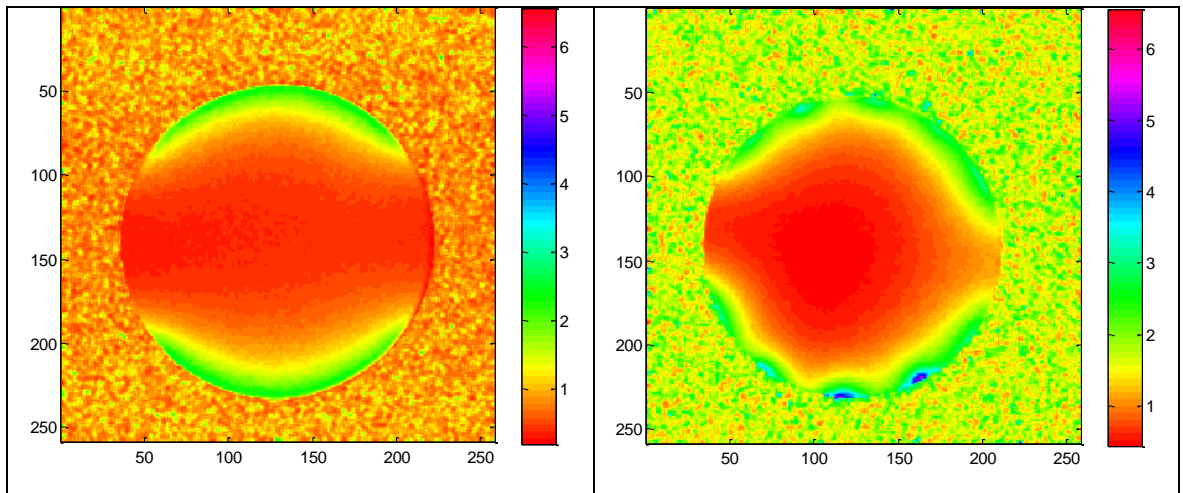
**FIG 6.12** The birdcage images as reference indicate the higher SNR from the sum-of-square of 10-channel array imaging. The top row is the original images in gray scale and SNR maps in bottom row show the same color bar level with array image to display intensity difference among the imaging modalities.

Figure 6.12 also includes an “SNR gains” map. The red line in the SNR map of the sum of squares image represents the threshold of any sensitivity gain as compared to the rat size volume coil. i.e. the sum of squares reconstructed array images show higher sensitivity than the rat size volume coil outside of the red line. The center region of array imaging still remained 87% of the rat size volume coil. The black line in the SNR map of the sum of squares image represents the sensitivity threshold as compared to the mouse 35 mm quad mode birdcage coil. Most parameters were held constant between the cylindrical array imaging and the compressible array imaging; however, the analog

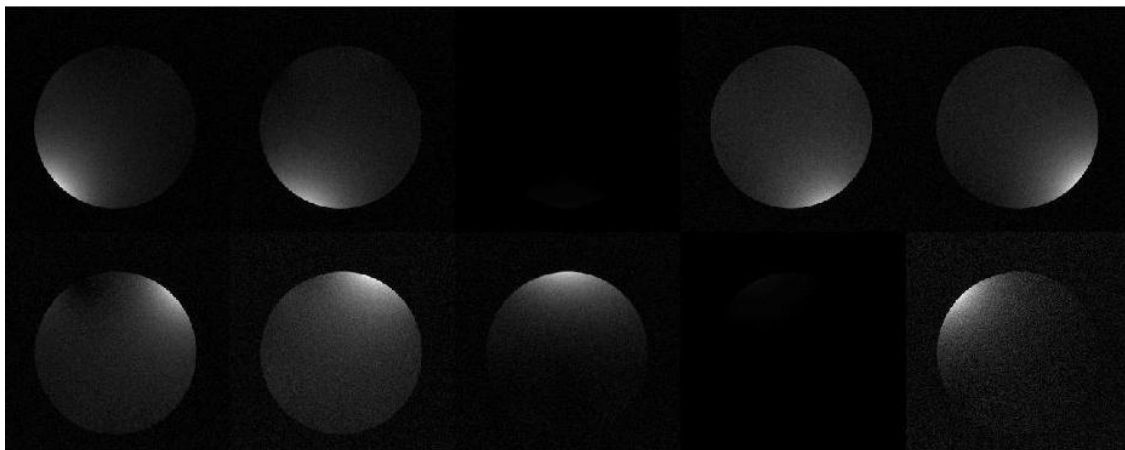
receiver gain and, most notably, the phantom was changed between the two different array configurations. A comparison of the sensitivities between the cylindrical array and compressed array is shown in Fig. 6.13. The carbon sulfate solution in the phantom evaporated with time and generated bubble to unload the array element as dynamic shifting load. So, a new phantom was made to uniformly load the new compressible array coils. Still, it is possible to see that while there was some improvement in sensitivity from the compressible array as compared to the cylindrical array, the image is non-uniform and did not provide the increase in imaging depth that was expected, even after accounting for the change of phantoms. These negative and unexpected results will be discussed further below.

It is worth noting that the Q value ratio of unloaded/loaded elements was 1.3 and therefore still indicates copper loss dominance rather than sample loss in the bench measurement. The implications of this affect the region of sensitivity over which there will be gains over a volume coil. Normally, with sample loss dominated elements, one would not expect an “SNR cost” at the center of the sample over using a volume coil. With copper loss dominated elements, we saw gains only on the perimeter. Additionally, the phantom size of the compressible array is 0.1 inch wider in diameter than the cylindrical array setting, possibly accounting for some of the lack of improvement seen. Importantly, there was immense element-to-element variability in sensitivity due to coil instability – a problem that in retrospect played a larger role than expected and needs to be remedied before further testing. This element-to-element variability is shown in Fig. 6.14. It is potentially caused by hand component assembly, in-house element

manufacturing, and attenuation due to different cable lengths. The reconstruction method therefore added to the perceived lack of sensitivity gain: in a quest to create the most uniform field pattern in the face of such non-uniform sensitivities in the reconstructed image, the field profile was normalized to generate uniformity at the expense of SNR.



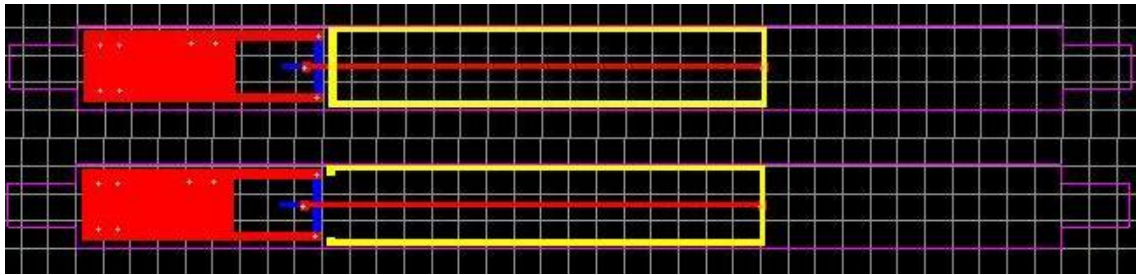
**FIG 6.13** Gain of SNR map as cylindrical array and compressible array against mouse birdcage coil.



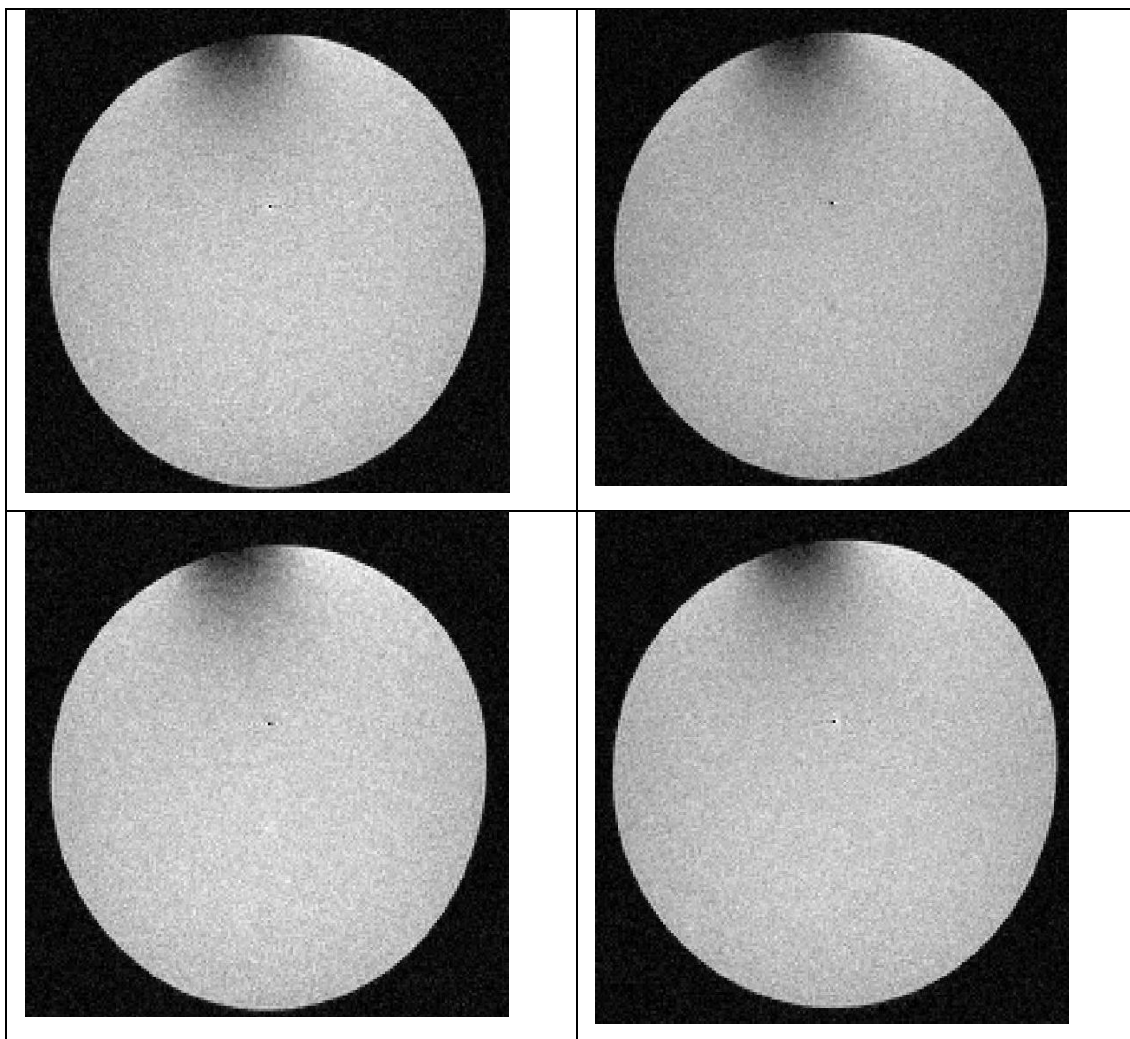
**FIG 6.14** Original profile slice before applying normalization indicate the immense element variation between channels.

Another source of inhomogeneity might have been overtipping due to array coil coupling to the transmit coil. While theoretically the DPP element should be immune to this, any asymmetries in construction will cause issues with the theory and these elements were etched in-house and populated by hand. In addition, since the elements were compressed directly onto the phantom, slight coupling would be more evident than in the cylindrical case where the elements were removed from the phantom.

Efforts have also been made to understand the loop mode effect in the DPP element. The backside of the DPP element creates a rectangular loop without any capacitors on it, but might still suffer from induced flux from the transmitting field. The circuit view of loop structure in DPP element and loop opened case were both showed in Figure 6.15 to illustrate the possible induced current path on coil. A single DPP element without any capacitors or coaxial cables populated on a board acting entirely open circuited at 200 MHz was attached right against the phantom to be imaged. Figure 6.16 indicates a coupling issue, though not definitely from the loop mode of the DPP element during transmit. To test, just a loop opened in the DPP element as bottom of Figure 6.15 was imaged in the same fashion.

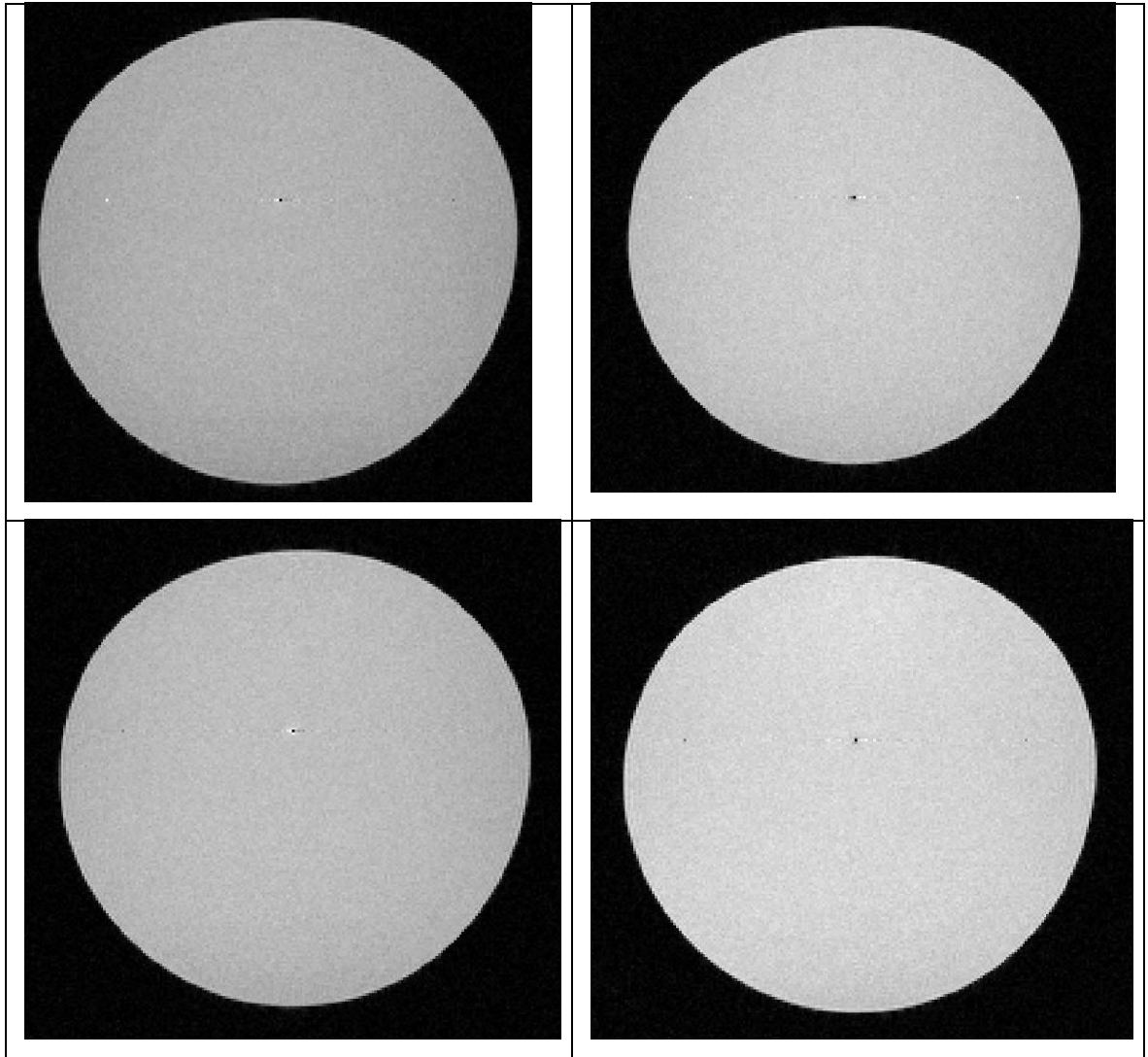


**Fig 6.15** The top DPP element indicated the yellow loop structure might induce transmit power and bottom DPP element represent the loop opened to avoid induced power.



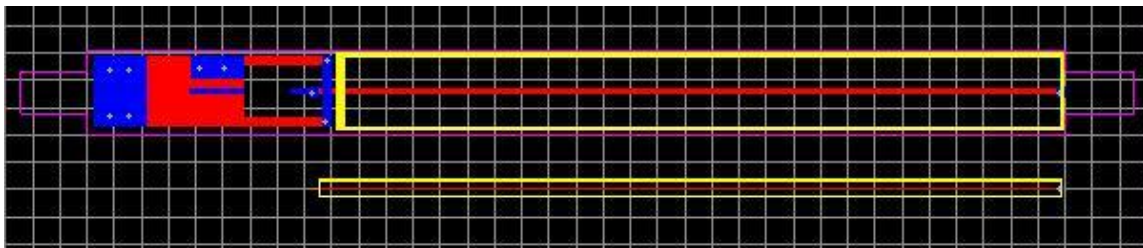
**Fig 6.16** Transmitting and receiving from birdcage with original DPP element inside. The images were obtained from spin-echo multislice imaging set with 1 cm slice offset in axial.

As a final test, figure 6.17 then displays the DPP element with loop structure open attached right against the phantom, confirming the homogeneity with the loop mode not present, but the element present.



**Fig 6.17** Transmitting and receiving from birdcage with DPP element inside as loop structure opened. These axial images were obtained from spin-echo multislice imaging set with 1 cm slice offset.

The loop mode effects of the DPP element generates some induced current on the element during transmit and was seen to be eliminated after breaking the loop structure without any capacitors/components populated on coil. Because shorting the loop mode in previous versions of the DPP design was enough to shift it out of the range of interest around 200MHz, we did not expect this issue. However, the change in size of the element caused this unexpected result. After expanding the DPP element from the microarray (8 cm long x 2mm wide) into the larger and wider mouse element (7.4 mm by 7 cm), the coupling issue from the loop structure presented itself and should be avoided to reduce coupling from transmit coil. Figure 6.18 demonstrate the physical loop size difference between microarray and mouse element that potential induced much more power by more symmetry rectangular shape and loop size. The loop mode effect also explains the surprisingly inadequate element-to-element decoupling provided by the low-input impedance preamplifiers. Performing active detuning on the DPP element since the detuning circuit would also detune the loop mode. It would however, be costly in space and complexity.

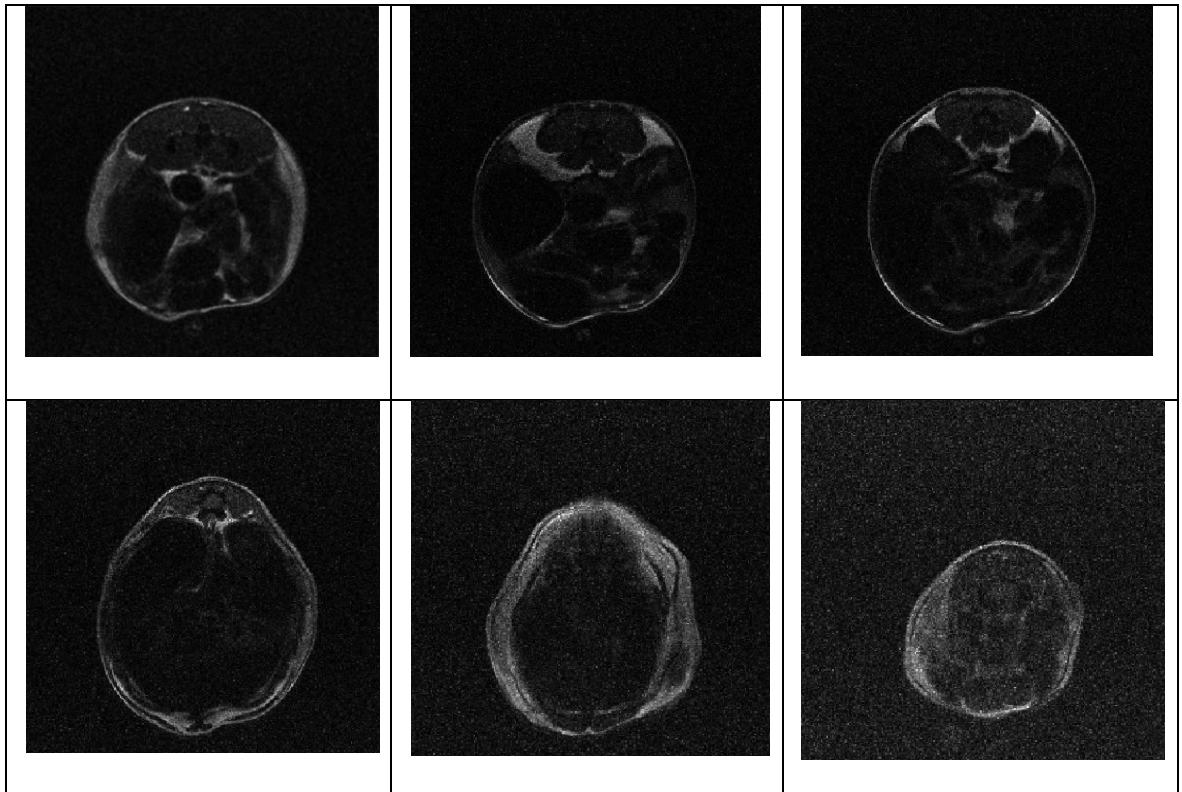


**Fig 6.18** DPP element with loop structure indicated as yellow rectangular demonstrated the loop mode issue exaggerated from microarray into mouse element design.

### 6.3 Euthanized Mouse Imaging with Array

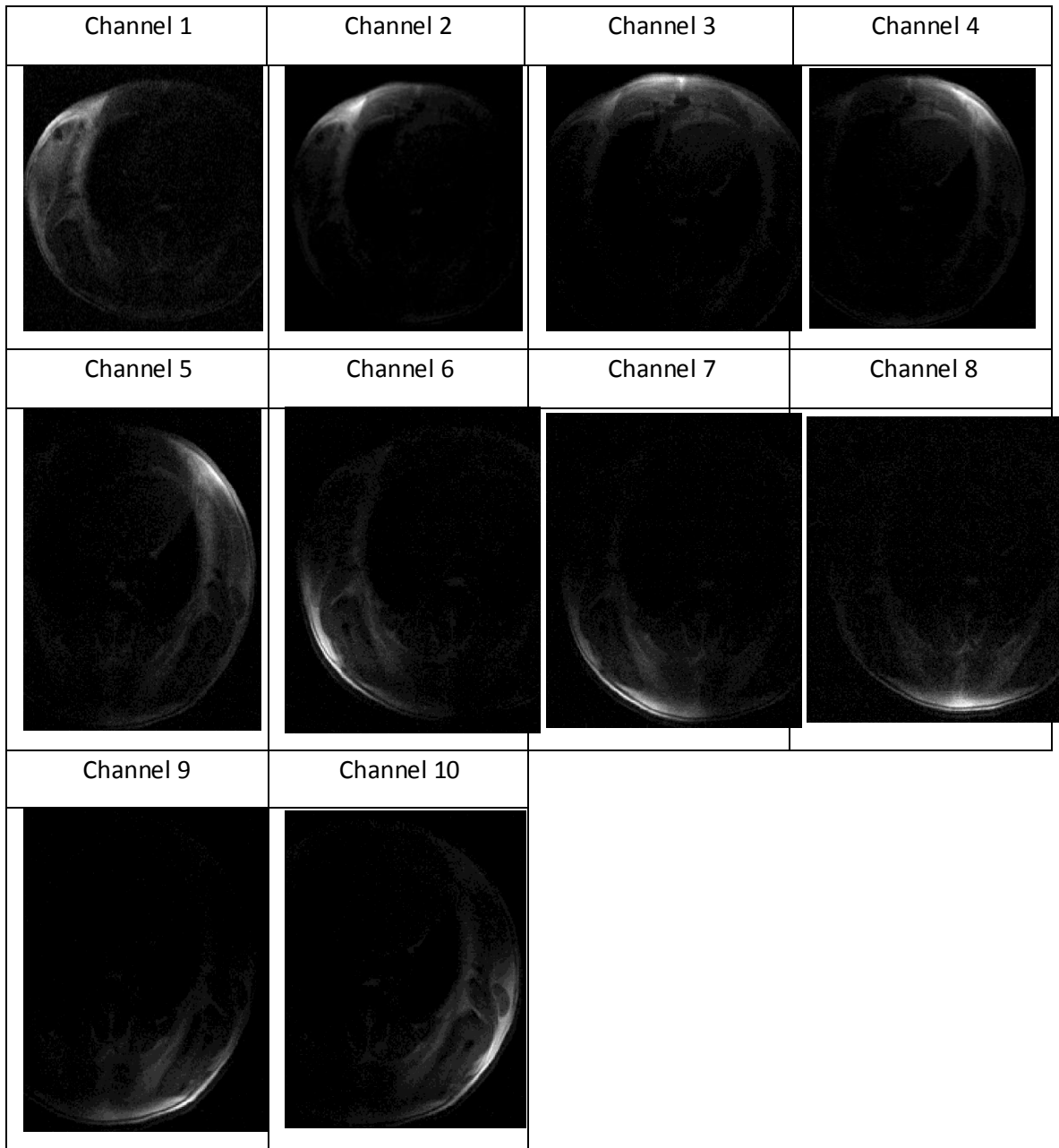
Despite being the process of working out issues with the array, we felt it was important to begin viewing any sensitivity benefits on the mouse anatomy itself. Euthanized mouse images were acquired by the 10-channel cylindrical array to demonstrate the compact RF array system for mouse imaging as shown in Figure 6.19. The imaging parameters were 1000/30 ms TR/TE,  $N_{\text{phase enc}} \times N_{\text{readout}} = 256 \times 256$  with 4 x 4-cm FOV, thickness of 2 mm with one average, 5.12 ms acquisition time, and 50,000 Hz spectral width. The multi-slice SEMS sequence was applied to scan between the diaphragm and kidney for the abdominal aorta. The array position is closer to the one side of the birdcage end-ring structure, so the SNR degradation fades away along the multi-slice number. The maximum RF field is built up at the center of the birdcage and decays toward both sides of the end-ring structure.





**FIG 6.19** Cylindrical 10-channel array imaging is obtained with 1000/30 TR/TE, 256 x 256 with 4 x 4cm FOV, and 2-mm thickness.

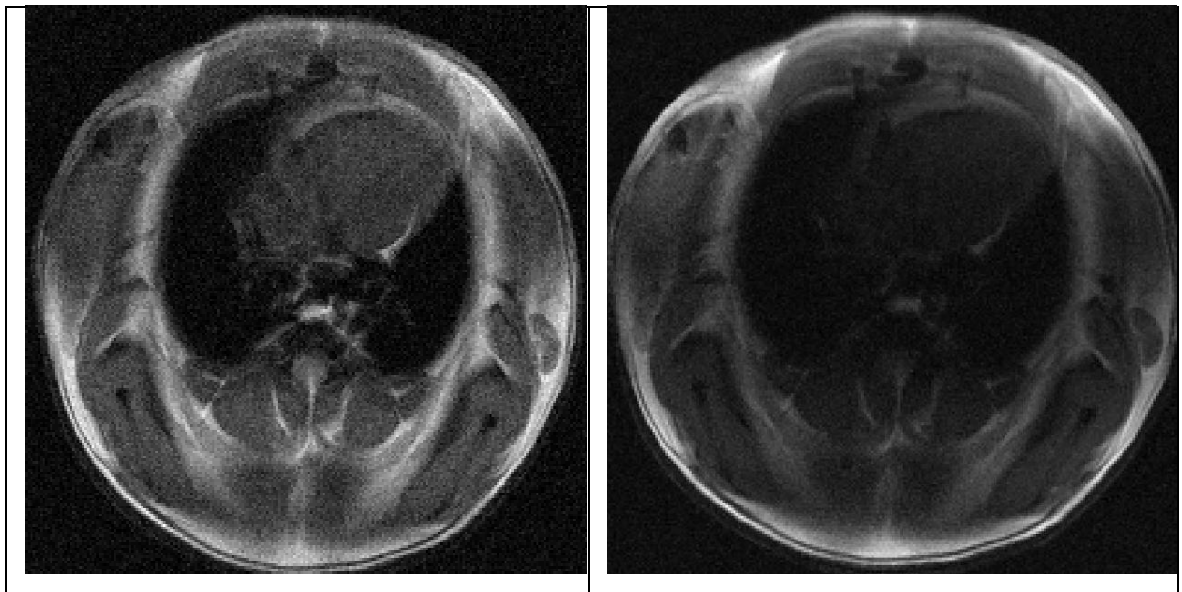
The procedure was repeated with the compressible 10 channel DPP array Figure 6.20 shows array profiles from every element for the mouse imaging with the compressible DPP arrays. The tune/match of all 10 channel DPP elements was fine adjusted to the mouse loading before the experiment to maintain the best RF signal and decoupling and try for more uniform images than was accomplished on phantoms. As seen in Fig. 6.20, uniformity between elements was indeed improved from the phantom imaging.



**FIG 6.20** Compressible 10-channel array imaging profiles are obtained with 1000/30 TR/TE, 256 x 256 with 3 x 3cm FOV, and 2-mm thickness.

Sum of squares reconstruction was applied to the 10 channel array profiles of mice to demonstrate the potential *in vivo* mouse imaging capability. Figure 6.21 presents

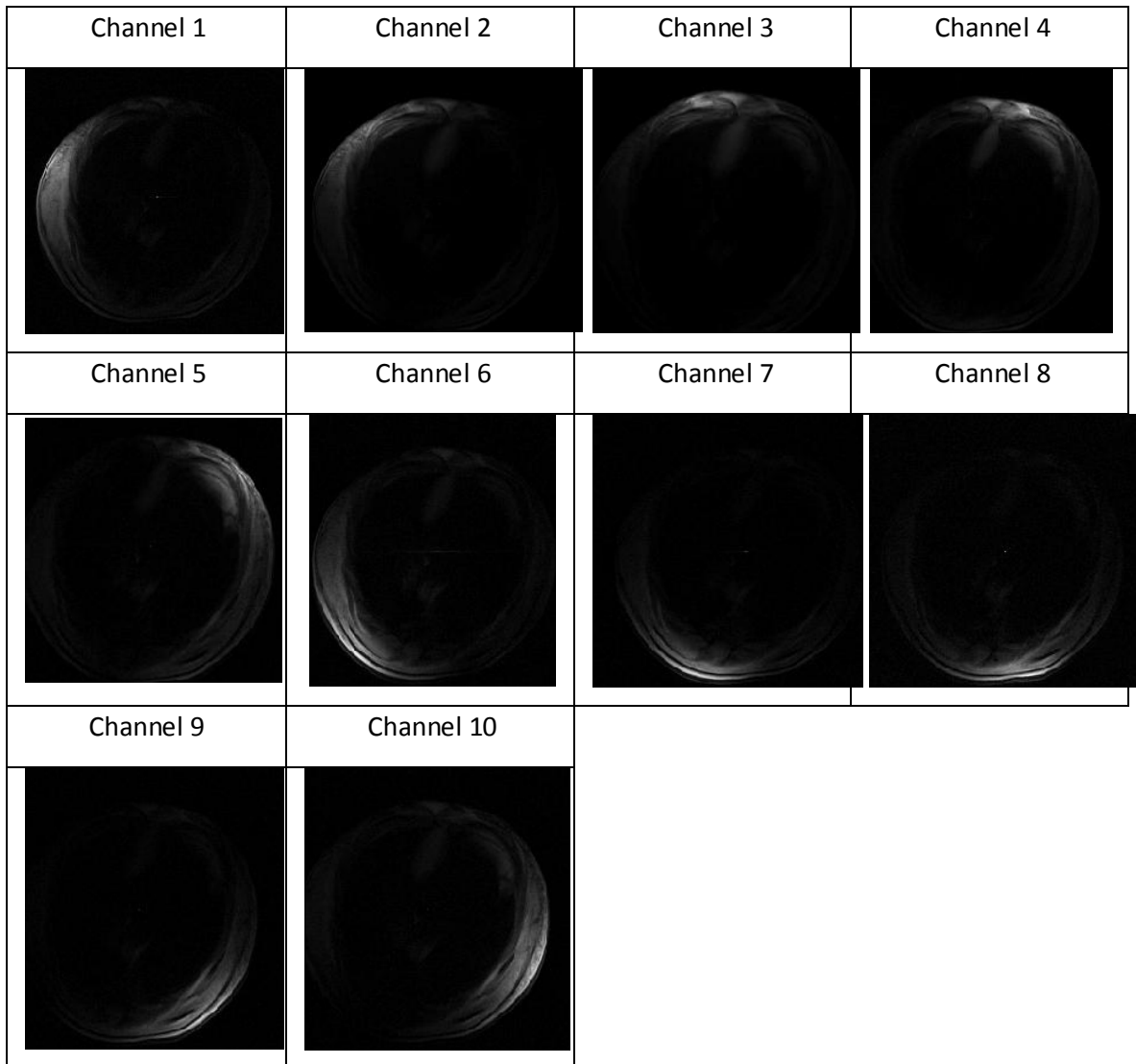
the SOS reconstructed image comparison with the rat size volume coil. The imaging with the euthanized mouse was intended to evaluate the initial capability of imaging the murine anatomy. Two chamber cardiac structure is clearly visible. Additionally, the inferior vena cava region behind spine is within 1 cm imaging depth, a region in which the 10 channel array has some advantage in sensitivity over the volume coil. Both images were averaged three times to reduce noise interference and all other parameters were the same also. As expected, the sensitivity is localized close to the perimeter of the mouse body.



**FIG 6.21** Left: Volume coil imaging with NEX = 3. Right: Reconstructed SOS imaging with NEX = 3. FOV = 3 x 3 cm with 26x256 points, 1000/30 msec TR/TE.

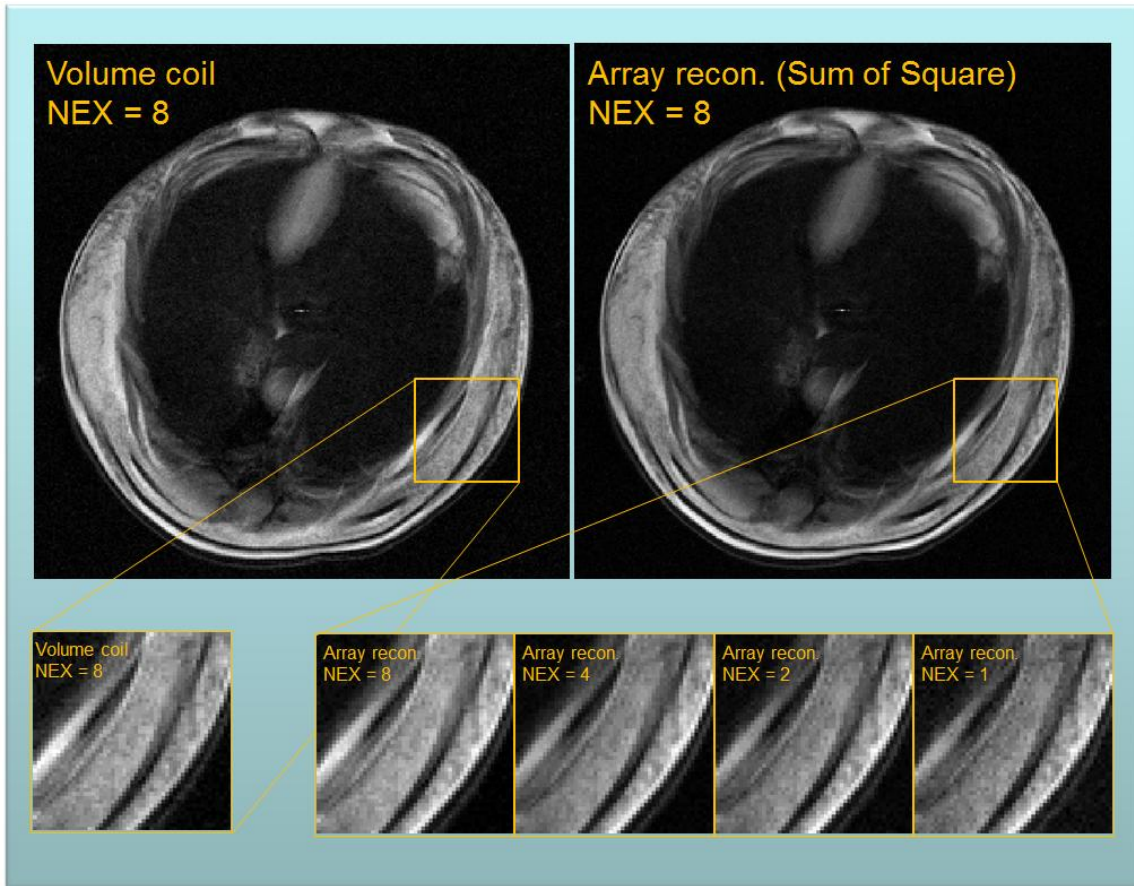
The number of averages was increased to eight in order to observe the data in higher SNR conditions. The single channel profile images from a euthanized mouse are

shown in Figure 6.22. Every channel's profile has been averaged eight times to increase the SNR. Every channel shows localized pattern without any coupling to adjacent channel.



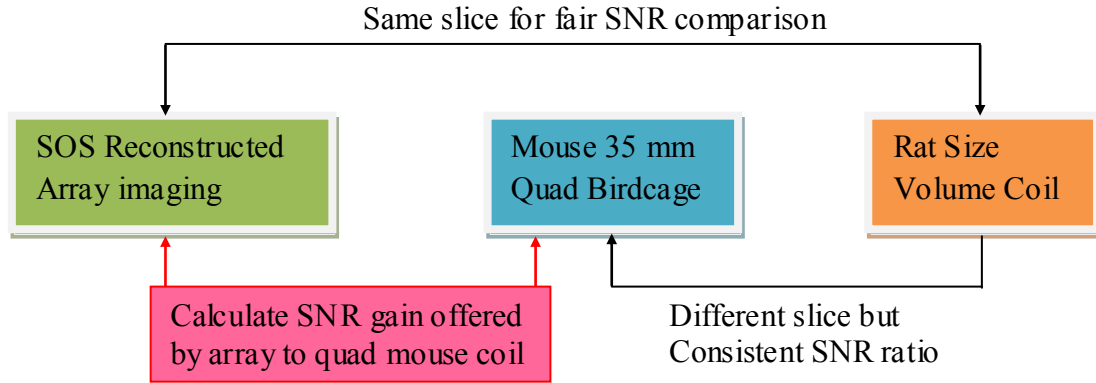
**FIG 6.22** Single channel profile images of 10 DPP elements as compressible arrays from an euthanized mouse. Average number is eight. The ten profile indicate the sensitivity benefits of euthanized mouse from array element.

Sum-of-squares reconstruction was applied to reconstruct the image from the array profiles. The comparison between the transmit volume coil and sum-of-squares reconstructed image is shown in Figure 6.23. In addition to this comparison, however, the improvement over the standard mouse 35 mm mouse coil is more meaningful. The sensitivity comparison between the array and rat coil was straightforward, as the images were acquired at the same time and same position or slice offset. The array does not fit into the 35mm mouse coil, and therefore an indirect method was applied to compare the SNR map with same slice offset. Both array and 35 mm mouse coil are designed to allocate the animal tightly inside the devices to have best imaging performance for each design strategy. The indirect approach assumes the SNR ratio remains constant between the rat volume coil and mouse coil based on their nature homogeneous field strength under same imaging parameter, as measured in a phantom.



**FIG 6.23** Comparison of the transmit volume coil image and the sum-of-square image from the array. The intensity of the sum-of-square image was normalized to the intensity of the volume coil image for visualization.

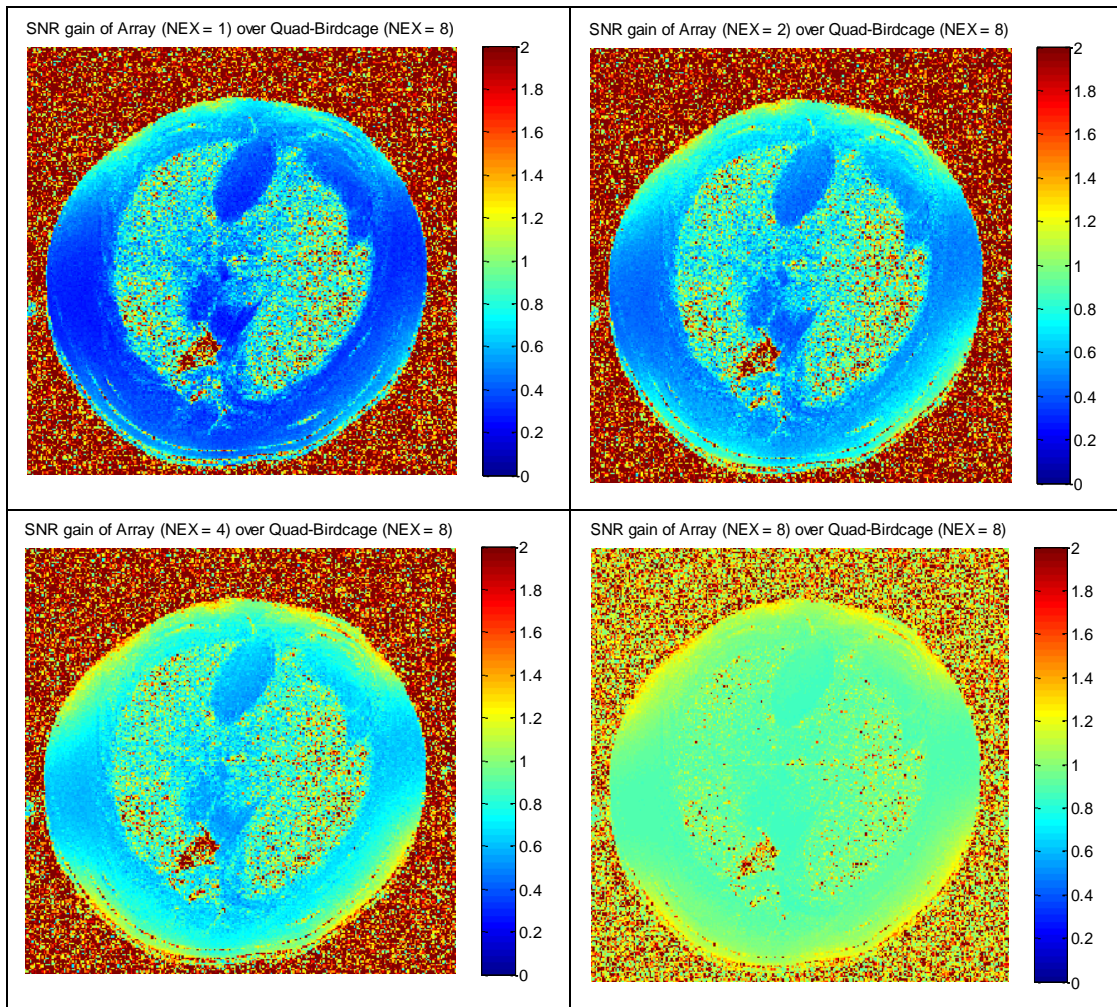
The classic characteristic of birdcage coil is a homogeneous field pattern in transverse slice[83]. In addition, the field strength stays the same around the center of the coil with different slice offsets in the z direction. The field only drops off close to the end ring at edge of the birdcage coil. Therefore, the SNR ratio between the 35mm mouse coil to the rat sized volume coil is valid in order to obtain the SNR relationship between mouse coil to the array reconstructed image. The method of indirect method is shown in Figure 6.24.



**FIG 6.24** Illustration of indirect method to obtain the map of SNR gain between compressible arrays reconstructed image and quad mode mouse birdcage image.

The map of SNR gain between the 35mm mouse coil and the reconstructed image from the compressible array coil is shown in Figure 6.25. The colorbar of the SNR gain represents the higher SNR as red and lower as blue. The NEX equal to one or two averages array images shows lower SNR as compared to the mouse birdcage. However, the green region representing equal SNR to the mouse coil is deeper into mouse body as NEX goes to eight averages. The number of average promotes the SNR of both volume coil and single channel DPP element. However, the SOS reconstructed image takes SNR improvement from every single element to compose array image that demonstrate the advantage of using average. Additionally, the number of averages provided us the information about the desired level of SNR improvement to perform adequate SNR at the center over mouse coil. The number of averages is directly useful information for future element design to increase sensitivity.





**FIG 6.25** The map of SNR gain offered by the array coil as compared to a 35 mm quad mode birdcage mouse coil. Sum-of-squares reconstruction was used with NEX = 1, 2, 4, 8 for the array and compared to NEX = 8 with the mouse coil.



## **6.4 Limitations and Future Work**

### **6.4.1 *In vivo* Experiments**

Additional *in vivo* experiments should include evaluating the sequence parameters with different trigger delays and parameters to show varying contrast. In addition, following the changes made in the element design and array construction recommended below, *in vivo* mouse imaging with arrays should be implemented using multiple receiver channels in order to actually demonstrate acceleration.

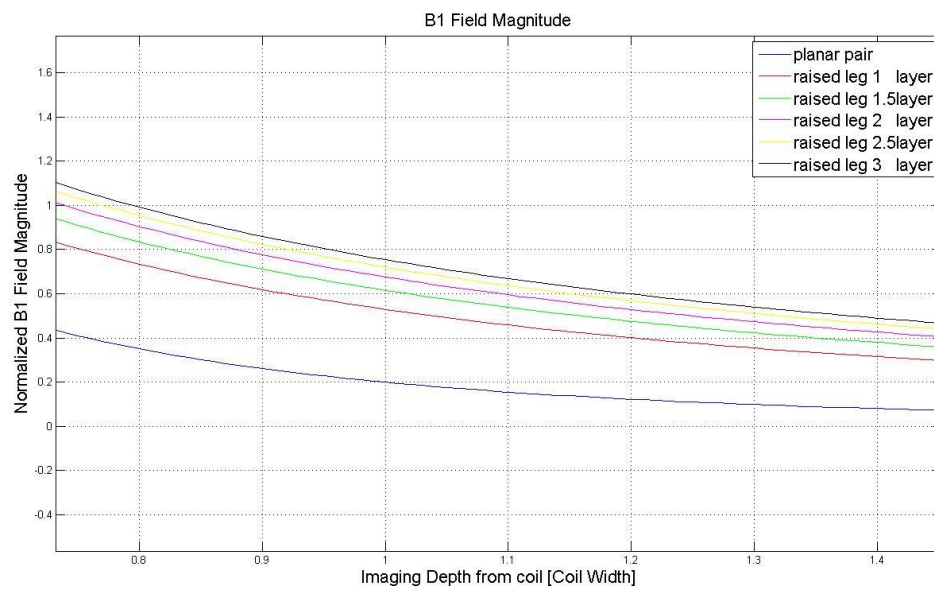
### **6.4.2 Element Design for Different Coil Length**

Different sizes of DPP elements could be considered and produced to have higher SNR and imaging depth. For instance, shorter DPP elements might reduce the coil resistance and copper loss for better SNR. The reduced length DPP element could cover the cardiac region at least but sacrifice body imaging capabilities covering whole mouse length.

### **6.4.3 Changing Distance between Signal Trace and Ground Leg of DPP Element**

The imaging depth of the DPP element is constrained because the nature of the field drops off at distance due to field cancellation from the current of the ground legs on either side. However, the DPP element provides good sensitivity profile within one coil width imaging depth. A multilayer DPP element with the ground legs further from the signal trace could extend the sensitivity map deeper but also carries the burden of having

stronger element-to-element coupling. A quasi-static simulation based on Biot-Savart law simulates the sensitivity improvement obtained from moving ground traces to the other side of different thicknesses of standard FR-4 layers. Figure 6.26 indicates the potential sensitivity improvement from the array element design to image deeper. Based on the coil dimension, the center of mouse would be presented at 1.4 coil widths separation. The sensitivity improvement from one layer DPP to three layers DPP element could be up to 47%.



**FIG 6.26** Quasi-static simulation on different thickness of DPP element.

#### **6.4.4 Tuning and Matching Network**

Changing the tune/match board design would be another way to reduce radiation loss and coupling through the matching network. To increase stability in particular, the board should be incorporated into the outsourced elements, discussed below.

#### **6.4.5 Element Outsourcing for Better Stability**

In industrial PCB fabrication, four to six FR-4 layers is standard and available, though mostly used in complicated motherboard manufacturing. The DPP element on standard FR-4 should be outsourced for fabrication for better element stability that will potentially contribute to better element-to-element uniformity.

#### **6.4.6 Better RF Connection on Preamplifier Board and Additional Functions**

The preamplifier board could be reorganized to have more stable RF connection with semi-rigid coaxial cables. The non-magnetic SMB or straight plug connectors for semi-rigid from Radiall would be a better choice than SMA for the constant plug in/out that is necessary. The 16 channel modular preamplifier board should be also modified for support DC source for multiple reasons with arrays. The active detuning circuit for transmit could be located on the preamplifier board. The pin-diode driver circuit could be easily combined into the preamplifier to trigger with the blanking signal from scanner and output adequate current to actively detune the array if needed. Varactor tuning would be another option to help detuning the array elements since any induced current/voltage would shift the varactor capacitance to detune. If this was done,

mounting 16 channel digital tuning circuits on the preamplifier board would also be an option. Active detuning would support decoupling of the elements from the volume coil and therefore the element dimension could be larger to have better Q value ratio and we could use loops if desired.

#### **6.4.7 Better Actively Detuned of Linear Birdcage**

The linear rat-size birdcage should also be actively detuned on multiple rungs rather than on the single end ring circuit. The inhomogeneities seen in the array imaging could partially have come from the volume coil where the rungs are very close to the array element and additional detuning circuitry on the transmit coil will help with this.

### **6.5 Conclusion**

In conclusion, this work has presented the foundational steps towards implementing accelerated *in vivo* mouse imaging in a small bore high field scanner. Artifact-free *in vivo* imaging with cardiac gating has been performed on the 4.7 Tesla/40 cm bore scanner in the MRSL. Even with imperfect performance, the initial design of a compact parallel imaging system for mice has provided experience in integrating all of the necessary components together for successful parallel imaging of live animals in a small bore system. This particular work presented a unique strategy using element designs to avoid space-consuming active detuning and baluns on the array elements. The 16 channel preamplifier board will play a key role in the future by providing the

flexibility to use different types of array elements for specific imaging. The *in vivo* imaging and gating system has been set up on the 4.7 Tesla / 40 cm bore to operate with other imaging coils and parallel imaging hardware and anesthesia can now be provided in the scanner for animals from mouse to rabbit size. Together, these components represent the foundational level tools to continue research in *in vivo* parallel imaging of small animals in the lab.

## REFERENCES

- [1] P. Carmeliet and D. Collen, "Transgenic mouse models in angiogenesis and cardiovascular disease," *The Journal of Pathology*, vol. 190, pp. 387-405, 2000.
- [2] F. Wiesmann, M. Szimtenings, A. Frydrychowicz, R. Illinger, A. Hunecke, E. Rommel, S. Neubauer, and A. Haase, "High-resolution MRI with cardiac and respiratory gating allows for accurate in vivo atherosclerotic plaque visualization in the murine aortic arch," *Magnetic Resonance in Medicine*, vol. 50, pp. 69-74, 2003.
- [3] F. H. Epstein, "MR in mouse models of cardiac disease," *NMR in Biomedicine*, vol. 20, pp. 238-255, May 2007.
- [4] T. A. M. Kaandorp, H. J. Lamb, E. E. van der Wall, A. de Roos, and J. J. Bax, "Cardiovascular MR to access myocardial viability in chronic ischaemic LV dysfunction," *Heart*, vol. 91, pp. 1359-1365, October 1, 2005 2005.
- [5] S. Ding, S. D. Wolff, and F. H. Epstein, "Improved coverage in dynamic contrast-enhanced cardiac MRI using interleaved gradient-echo EPI," *Magnetic Resonance in Medicine*, vol. 39, pp. 514-519, 1998.
- [6] A. P. Chen, R. E. Hurd, M. A. Schroeder, A. Z. Lau, Y.-p. Gu, W. W. Lam, J. Barry, J. Tropp, and C. H. Cunningham, "Simultaneous investigation of cardiac pyruvate dehydrogenase flux, Krebs cycle metabolism and pH, using hyperpolarized [1,2-<sup>13</sup>C<sub>2</sub>]pyruvate in vivo," *NMR in Biomedicine*, vol. 25, pp. 305-311, 2012.
- [7] T. Niendorf and D. Sodickson, "Highly accelerated cardiovascular MR imaging using many channel technology: concepts and clinical applications," *European Radiology*, vol. 18, pp. 87-102, 2008.
- [8] M. P. McDougall and S. M. Wright, "64-channel array coil for single echo acquisition magnetic resonance imaging," *Magnetic Resonance in Medicine*, vol. 54, pp. 386-392, 2005.

- [9] M. P. McDougall and S. M. Wright, "Initial results in wide-field 3D microscopy using parallel imaging," in *4th IEEE International Symposium on Biomedical Imaging*, Washington, D.C. USA, 2007, pp. 1072-1075.
- [10] A. Feintuch, Y. H. Zhu, J. Bishop, L. Davidson, J. Dazai, B. G. Bruneau, and R. M. Henkelman, "4D cardiac MRI in the mouse," *NMR in Biomedicine*, vol. 20, pp. 360-365, May 2007.
- [11] F. Franco, S. K. Dubois, R. M. Peshock, and R. V. Shoet, "Magnetic resonance imaging accurately estimates LV mass in a transgenic mouse model of cardiac hypertrophy," *American Journal of Physiology-Heart and Circulatory Physiology*, vol. 274, pp. H679-H683, Feb 1998.
- [12] V. Herold, P. Morchel, C. Faber, E. Rommel, A. Haase, and P. M. Jakob, "In vivo quantitative three-dimensional motion mapping of the murine myocardium with PC-MRI at 17.6 T," *Magnetic Resonance in Medicine*, vol. 55, pp. 1058-1064, May 2006.
- [13] V. Mor-Avi, L. Sugeng, L. Weinert, P. MacEneaney, E. G. Caiani, R. Koch, I. S. Salgo, and R. M. Lang, "Fast measurement of left ventricular mass with real-time three-dimensional echocardiography: comparison with magnetic resonance imaging," *Circulation*, vol. 110, pp. 1814-1818, September 28, 2004 2004.
- [14] J. E. Schneider, T. Lanz, H. Barnes, D. Medway, L. A. Stork, C. A. Lygate, S. Smart, M. A. Griswold, and S. Neubauer, "Ultra-fast and accurate assessment of cardiac function in rats using accelerated MRI at 9.4 Tesla," *Magnetic Resonance in Medicine*, vol. 59, pp. 636-641, 2008.
- [15] T. Lanz, M. Müller, H. Barnes, S. Neubauer, and J. E. Schneider, "A high-throughput eight-channel probe head for murine MRI at 9.4 T," *Magnetic Resonance in Medicine*, vol. 64, pp. 80-87, 2010.
- [16] B. W. Keil, Lawrence; Wiggins, Graham; Triantafyllou, Christina; Meise, Florian M.; Klose, Klaus Jochen; Heverhagen, Johannes T., "20-channel mouse phased-array coil for clinical 3 Tesla MRI scanner," in *Proceedings of the 16th Annual Meeting of the ISMRM*, Toronto, 2008.

- [17] K. V. Mogatadakala, J. A. Bankson, and P. A. Narayana, "Three-element phased-array coil for imaging of rat spinal cord at 7T," *Magnetic Resonance in Medicine*, vol. 60, pp. 1498-1505, Dec 2008.
- [18] M. S. Ramirez, E. Esparza-Coss, and J. A. Bankson, "Multiple-mouse MRI with multiple arrays of receive coils," *Magnetic Resonance in Medicine*, vol. 63, pp. 803-810, Mar 2010.
- [19] K. Feng, M. P. McDougall, and S. M. Wright, "Transmit / receive single echo imaging," in *Proceedings of the 19th Annual Meeting of the ISMRM*, Montreal, Quebec CANADA, 2011.
- [20] K. Feng, N. Hollingsworth, M. McDougall, and S. Wright, "A 64-channel transmitter for investigating parallel transmit MRI," *IEEE Transactions on Biomedical Engineering*, vol. PP, pp. 1-1, 2012.
- [21] A. Haase, "Snapshot flash mri. applications to t1, t2, and chemical-shift imaging," *Magnetic Resonance in Medicine*, vol. 13, pp. 77-89, 1990.
- [22] P. Mansfield, "Multi-planar image formation using NMR spin echoes," *Journal of Physics C: Solid State Physics*, vol. 10, p. L55, 1977.
- [23] M. K. Stehling, R. Turner, and P. Mansfield, "Echo-planar imaging: magnetic resonance imaging in a fraction of a second," *Science*, vol. 254, pp. 43-50, October 4, 1991 1991.
- [24] S. Warach, J. Gaa, B. Siewert, P. Wielopolski, and R. R. Edelman, "Acute human stroke studied by whole brain echo planar diffusion-weighted magnetic resonance imaging," *Annals of Neurology*, vol. 37, pp. 231-241, 1995.
- [25] R. Bammer, S. L. Keeling, M. Augustin, K. P. Pruessmann, R. Wolf, R. Stollberger, H.-P. Hartung, and F. Fazekas, "Improved diffusion-weighted single-shot echo-planar imaging (EPI) in stroke using sensitivity encoding (SENSE)," *Magnetic Resonance in Medicine*, vol. 46, pp. 548-554, 2001.
- [26] T. Sugahara, Y. Korogi, M. Kochi, I. Ikushima, Y. Shigematu, T. Hirai, T. Okuda, L. Liang, Y. Ge, Y. Komohara, Y. Ushio, and M. Takahashi, "Usefulness



of diffusion-weighted MRI with echo-planar technique in the evaluation of cellularity in gliomas," *Journal of Magnetic Resonance Imaging*, vol. 9, pp. 53-60, 1999.

- [27] S. Warach, J. F. Dashe, and R. R. Edelman, "Clinical outcome in ischemic stroke predicted by early diffusion-weighted and perfusion magnetic resonance pmaging: a preliminary analysis," *J Cereb Blood Flow Metab*, vol. 16, pp. 53-59, 1996.
- [28] F. Q. Ye, J. J. Pekar, P. Jezzard, J. Duyn, J. A. Frank, and A. C. McLaughlin, "Perfusion imaging of the human brain at 1.5 T using a single-shot EPI spin tagging approach," *Magnetic Resonance in Medicine*, vol. 36, pp. 219-224, 1996.
- [29] M. K. Stehling, N. G. Holzknecht, G. Laub, D. Böhm, A. von Smekal, and M. Reiser, "Single-shot t1-and t2-weighted magnetic resonance imaging of the heart with black blood: preliminary experience," *Magnetic Resonance Materials in Physics, Biology and Medicine*, vol. 4, pp. 231-240, 1996.
- [30] S. Ogawa, T. M. Lee, A. R. Kay, and D. W. Tank, "Brain magnetic resonance imaging with contrast dependent on blood oxygenation," *Proceedings of the National Academy of Sciences*, vol. 87, pp. 9868-9872, December 1, 1990 1990.
- [31] S. Ogawa, D. W. Tank, R. Menon, J. M. Ellermann, S. G. Kim, H. Merkle, and K. Ugurbil, "Intrinsic signal changes accompanying sensory stimulation: functional brain mapping with magnetic resonance imaging," *Proceedings of the National Academy of Sciences*, vol. 89, pp. 5951-5955, July 1, 1992 1992.
- [32] B. Biswal, F. Zerrin Yetkin, V. M. Haughton, and J. S. Hyde, "Functional connectivity in the motor cortex of resting human brain using echo-planar MRI," *Magnetic Resonance in Medicine*, vol. 34, pp. 537-541, 1995.
- [33] P. A. Bandettini, A. Jesmanowicz, E. C. Wong, and J. S. Hyde, "Processing strategies for time-course data sets in functional MRI of the human brain," *Magnetic Resonance in Medicine*, vol. 30, pp. 161-173, 1993.
- [34] A. Kami, G. Meyer, P. Jezzard, M. M. Adams, R. Turner, and L. G. Ungerleider, "Functional MRI evidence for adult motor cortex plasticity during motor skill learning," *Nature*, vol. 377, pp. 155-158, 1995.

- [35] K. J. Friston, P. Jezzard, and R. Turner, "Analysis of functional MRI time-series," *Human Brain Mapping*, vol. 1, pp. 153-171, 1994.
- [36] J. Reilly, "Peripheral nerve stimulation by induced electric currents: Exposure to time-varying magnetic fields," *Medical and Biological Engineering and Computing*, vol. 27, pp. 101-110, 1989.
- [37] J. S. Hyde, A. Jesmanowicz, T. M. Grist, W. Froncisz, and J. B. Kneeland, "Quadrature detection surface coil," *Magnetic Resonance in Medicine*, vol. 4, pp. 179-184, 1987.
- [38] M. Hutchinson and U. Raff, "Fast MRI data acquisition using multiple detectors," *Magnetic Resonance in Medicine*, vol. 6, pp. 87-91, 1988.
- [39] S. M. Wright, R. L. Magin, and J. R. Kelton, "Arrays of mutually coupled receiver coils: Theory and application," *Magnetic Resonance in Medicine*, vol. 17, pp. 252-268, 1991.
- [40] S. M. Wright, "Bilateral MR imaging with switched mutually coupled receiver coils," *Radiology*, vol. 170, p. 249, 1989.
- [41] P. B. Roemer, W. A. Edelstein, C. E. Hayes, S. P. Souza, and O. M. Mueller, "The NMR phased-array," *Magnetic Resonance in Medicine*, vol. 16, pp. 192-225, 1990.
- [42] M. Schmitt, A. Potthast, D. E. Sosnovik, J. R. Polimeni, G. C. Wiggins, C. Triantafyllou, and L. L. Wald, "A 128-channel receive-only cardiac coil for highly accelerated cardiac MRI at 3 tesla," *Magnetic Resonance in Medicine*, vol. 59, pp. 1431-1439, Jun 2008.
- [43] C. J. Hardy, R. O. Giaquinto, J. E. Piel, K. W. Rohling, L. Marinelli, D. J. Blezek, E. W. Fiveland, R. D. Darrow, and T. K. F. Foo, "128-Channel body MRI with a flexible high-density receiver-coil array," *Journal of Magnetic Resonance Imaging*, vol. 28, pp. 1219-1225, 2008.

- [44] G. C. Wiggins, J. R. Polimeni, A. Potthast, M. Schmitt, V. Alagappan, and L. L. Wald, "96-Channel receive-only head coil for 3 tesla: Design optimization and evaluation," *Magnetic Resonance in Medicine*, vol. 62, pp. 754-762, 2009.
- [45] G. C. Wiggins, C. Triantafyllou, A. Potthast, A. Reykowski, M. Nittka, and L. L. Wald, "32-Channel 3 tesla receive-only phased-array head coil with soccer-ball element geometry," *Magnetic Resonance in Medicine*, vol. 56, pp. 216-223, 2006.
- [46] C. J. Hardy, H. E. Cline, R. O. Giaquinto, T. Niendorf, A. K. Grant, and D. K. Sodickson, "32-element receiver-coil array for cardiac imaging," *Magnetic Resonance in Medicine*, vol. 55, pp. 1142-1149, 2006.
- [47] C. Triantafyllou, J. R. Polimeni, and L. L. Wald, "Physiological noise and signal-to-noise ratio in fMRI with multi-channel array coils," *NeuroImage*, vol. 55, pp. 597-606, 2011.
- [48] Z. Wang, J. Wang, T. J. Connick, G. S. Wetmore, and J. A. Detre, "Continuous ASL (CASL) perfusion MRI with an array coil and parallel imaging at 3T," *Magnetic Resonance in Medicine*, vol. 54, pp. 732-737, 2005.
- [49] D. G. Brown, M. P. McDougall, and S. M. Wright, "Receiver design for parallel imaging with large arrays," in *Proceedings of the 10th Annual Meeting of the ISMRM*, Honolulu, HI USA, 2002, p. 863.
- [50] M. P. McDougall and S. M. Wright, "Investigation of coil phase compensation in 3D imaging at very high acceleration factors," *Journal of Magnetic Resonance Imaging*, vol. 25, pp. 1305-1311, 2007.
- [51] M. P. McDougall and S. M. Wright, "A Parallel imaging approach to wide-field MR microscopy," *Magnetic Resonance in Medicine*, pp. n/a-n/a, 2011.
- [52] M. P. McDougall and S. M. Wright, "Phase compensation in single echo acquisition imaging," *Engineering in Medicine and Biology Magazine, IEEE*, vol. 24, pp. 17-22, 2005.

- [53] K. Feng, M. P. McDougall, and S. M. Wright, "Simple digital tuning system for large array coils," in *Proceedings of the 15th Annual Meeting of the ISMRM*, Berlin, Germany, 2007.
- [54] C.-W. Chang, K. L. Moody, and M. P. McDougall, "An improved element design for 64-channel planar imaging," *Concepts in Magnetic Resonance Part B: Magnetic Resonance Engineering*, vol. 39B, pp. 159-165, 2011.
- [55] D. Kwiat, S. Einav, and G. Navon, "A decoupled coil detector array for fast image acquisition in magnetic resonance imaging," *Medical Physics*, vol. 18, pp. 251-265, 1991.
- [56] J. Carlson, "An algorithm for NMR imaging reconstruction based on multiple RF receiver coils. ," *Journal of Magnetic Resonance*, vol. 74, pp. 376-380, 1987.
- [57] D. K. Sodickson, "Spatial encoding using multiple RF coils: SMASH imaging and parallel MRI," in *Methods in Biomedical Magnetic Resonance Imaging and Spectroscopy*, I. R. Young, Ed., ed: John Wiley & Sons 2000, pp. 239-250.
- [58] S. M. Wright, M. P. McDougall, and D. G. Brown, "Single echo acquisition of MR images using RF coil arrays," in *Proceedings of the Second Joint EMBS/BMES Conference*, Houston, TX USA, 2002, pp. 1181-1182.
- [59] S. M. Wright and M. P. McDougall, "Single echo acquisition MRI using RF encoding," *NMR Biomedicine*, vol. 22, pp. 982-93, Nov 2009.
- [60] S. M. Wright, M. P. McDougall, and N. Yallapragada, "Rapid flow imaging using single echo acquisition MRI," in *Proceedings of the 13th Annual Meeting of the ISMRM*, Miami, FL USA, 2005, p. 289.
- [61] S. M. Wright, M. P. McDougall, and N. Yallapragada, "Ultra-fast MR velocity measurement using spin-tagging and single-echo acquisition (SEA) imaging," in *Proceedings of the 14th Annual Meeting of the ISMRM*, Seattle, WA USA, 2006, p. 203.

- [62] J. Bosshard, N. Yallapragada, M. McDougall, and S. Wright, "High speed MR elastography using SEA imaging," in *Proceedings 16th Scientific Meeting of the ISMRM*, Toronto, 2008, p. 831.
- [63] S. Wright and M. McDougall, "MR imaging at sub-millisecond frame rates," in *Proceedings 17th Scientific Meeting of the ISMRM*, Honolulu, 2009, p. 259.
- [64] M. A. Griswold, P. M. Jakob, M. Nittka, J. W. Goldfarb, and A. Haase, "Partially parallel imaging with localized sensitivities (PILS)," *Magnetic Resonance in Medicine*, vol. 44, pp. 602-609, 2000.
- [65] M. P. McDougall and S. M. Wright, "Initial results in wide-field-of-view 3D MR microscopy using parallel imaging," in *Biomedical Imaging: From Nano to Macro, 2007. ISBI 2007. 4th IEEE International Symposium on*, 2007, pp. 1072-1075.
- [66] M. P. McDougall, S. M. Wright, N. Yallapragada, I. Steele-Russell, and M. Russell, "Rapid large field-of-view microscopy using parallel imaging," in *Proceedings of the 14th Annual Meeting of the ISMRM*, Seattle, WA USA, 2006, p. 2448.
- [67] S. M. Wright, M. P. McDougall, K. Kurpad, and D. G. Brown, "Parallel imaging: system design and limitations," in *Proceedings of the 2004 IEEE International Symposium on Biomedical Imaging: From Nano to Macro, Arlington VA, USA.*, 2004, pp. 1200-1203 Vol. 2.
- [68] S. M. Wright, M. P. McDougall, F. Ke, N. A. Hollingsworth, J. C. Bosshard, and C. Chieh-Wei, "Highly parallel transmit/receive systems for dynamic MRI," in *Engineering in Medicine and Biology Society, 2009. EMBC 2009. Annual International Conference of the IEEE*, 2009, pp. 4053-4056.
- [69] M. P. McDougall, J. M. Knight, E. E. Eigenbrodt, S. M. Wright, and C.-W. Chang, "A simple approach to overcoming mutual coupling effects in some transmit array coils for magnetic resonance imaging," in *Engineering in Medicine and Biology Society, 2008. EMBS 2008. 30th Annual International Conference of the IEEE*, 2008, pp. 2043-2046.

- [70] C. J. Goergen, K. N. Barr, D. T. Huynh, J. R. Eastham-Anderson, G. Choi, M. Hedehus, R. L. Dalman, A. J. Connolly, C. A. Taylor, P. S. Tsao, and J. M. Greve, "In vivo quantification of murine aortic cyclic strain, motion, and curvature: Implications for abdominal aortic aneurysm growth," *Journal of Magnetic Resonance Imaging*, vol. 32, pp. 847-858.
- [71] "Frontmatter," in *Standards of Mouse Model Phenotyping*, ed: Wiley-VCH Verlag GmbH, 2008, pp. i-xxvi.
- [72] D. Gareis, T. Wichmann, T. Lanz, G. Melkus, M. Horn, and P. M. Jakob, "Mouse MRI using phased-array coils," *NMR in Biomedicine*, vol. 20, pp. 326-334, 2007.
- [73] O. Dietrich, T. Lanz, H. M. Reinl, B. Frank, M. Peller, M. F. Reiser, and S. O. Schoenberg, "Parallel imaging of mice on a clinical 3-telsa MRI system with a dedicated 8-channel small-animal coil array," in *Proceedings of the 15th Annual Meeting of the ISMRM*, Berlin, Germany, 2007, p. 1759.
- [74] J.-X. WANG, N. Tian, F. J. Robb, A. P. Chen, L. Friesen-Waldner, B. K. Rutt, and C. A. McKenzie, "An 8-channel coil array for small animal  $^{13}\text{C}$  MR imaging," in *Proceedings of the 18th Annual Meeting of the ISMRM*, Stockholm, Sweden, 2010, p. 1489.
- [75] M. Tabbert, M. Motz, M. Lopez, E. Pfrommer, and S. Junge, "A 16-channel rat-body array coil with an integrated birdcage transmitter at 7T," in *Proceedings of the 17th Annual Meeting of the ISMRM*, Honolulu, USA, 2010, p. 4735.
- [76] B. Keil, G. C. Wiggins, C. Triantafyllou, L. L. Wald, F. M. Meise, L. M. Schreiber, K. J. Klose, and J. T. Heverhagen, "A 20-channel receive-only mouse array coil for a 3 T clinical MRI system," *Magnetic Resonance in Medicine*, vol. 66, pp. 582-593, 2011.
- [77] A. Reykowski, S. M. Wright, and J. R. Porter, "Design of matching networks for low noise preamplifiers," *Magnetic Resonance in Medicine*, vol. 33, pp. 848-852, 1995.
- [78] K. L. Moody, N. A. Hollingsworth, J.-F. Nielsen, D. Noll, S. M. Wright, and M. P. McDougall, "RF transparent array for testing multi-channel transmit systems,"

in *Proceedings of the 18th Annual Meeting of the ISMRM*, Stockholm, Sweden, 2010.

- [79] Y. Xu and P. Tang, "Easy fabrication of a tunable high-pass birdcage resonator," *Magnetic Resonance in Medicine*, vol. 38, pp. 168-172, 1997.
  
- [80] M. P. McDougall, S. M. Wright, and D. G. Brown, "A low-pass trombone birdcage coil with broad tuning range," in *Proceedings of the 9th Annual Meeting of the ISMRM*, Glasgow, Scotland, UK, 2001, p. 18.
  
- [81] R. K. Yang, C. G. Roth, R. J. Ward, J. O. deJesus, and D. G. Mitchell, "Optimizing abdominal MR imaging: approaches to common problems1," *Radiographics*, vol. 30, pp. 185-199, January 1, 2010 2010.
  
- [82] L. Arena, H. T. Morehouse, and J. Safir, "MR imaging artifacts that simulate disease: how to recognize and eliminate them," *Radiographics*, vol. 15, pp. 1373-1394, November 1, 1995 1995.
  
- [83] J. M. Jin, Book: *Electromagnetic Analysis and Design in Magnetic Resonance Imaging*: ISBN: 0-8493-9693-X, Boca Raton : CRC Press, 1999.

## APPENDIX I

### Preparation

- Separate the components of the animal holder and leave only the mouse sled on the surgical bed
- Turn on the scanner and confirm that the software and pulse sequence is ready for use.
- Turn on the air heater and assign a temperature on the PC-SAM software

### Turn on Small Animal Gating System

- Turn on the extension cable power switch at the gating table
- Turn on the laptop at the console
- Turn on the monitor power for viewing the SA software next to the shielded room
- Turn on the software, PC-SAM, and SA gating icon on the desktop of the SA notebook
- Check the optic cable connection between the following modules

ECG/TEMP module to the control module

Respiratory module to the control module

Serial cable from the control module to the laptop

Gating BNX coaxial from the control module to EXT TRG port at the back of the scanner

Confirm that the battery is connected to the ECG/TEMP module and the battery capacity is displayed by the software on the monitor



### **At the Animal Preparation Table**

- Turn on the water circulation warming system. Set the temperature to 42 degree C
- Check the connection at the output of the EZ vaporizer. First, we connect the quick connector to flow the gas to the knock-down chamber
- Check the isoflurane level of both vaporizers and confirm that the levels are above marked line.
- Set the iso flurane percentage to 0
- Turn the flow meter of the evaporator (on preparation table) to fully open and use this as a flow indicator. Totally rely on the oxygen tank regulator to control the flow (2.5 liter/minute). Turn on the oxygen tank against the laboratory fence and limit the pressure to 2.5 liter/minute
- Confirm that the gas is flowing out of the knock-out chamber
- Set the iso flurane percentage to 4%
- Place the animal in the chamber and wait

### **Animal on the Surgical Bed**

- When the animal is down, switch the tubing at the quick connector of the output port of the EZ vaporizer from knock-down chamber to surgical bed
- Open the chamber lid and move the animal to the heated surgical bed
- Unplug the gas stopper
- Turn the evaporator to 2 to 2.5%

- Remove the animal's fur for the ECG sensor between the chest
- Put the electrical pad on the ECG sensor of the mouse sled for better signal picked up and mount the mouse sled on the animal
- Use head fixture Velcro to hold the mouse head position if needed
- Respiratory sensor is on the mouse sled but don't push animal too hard against respiratory pillow
- Temperature sensor is on the mouse sled where is very close to the animal body. There is no need to have invasive measurement as manual request.
- Switch the gas tubing at the quick connector of the output of the EZ vaporizer from surgical bed to shielded room
- Place the holder with the mouse sled on the surgical bed or lift the surgical bed higher and slide it on the surgical bed
- Place the mouse with the sled into the animal holder
- Maintain the animal's position by holding the teeth into the hole of the gas tubing
- Lock the screw on the tubing and mark it in blue
- Move animal together with animal holder and mouse sled into the shielding room

#### **Use Vetland Vaporizer in the Shielded Room**

- Take the animal with holder into shielded room
- Mount the hot-air tubing on the holder
- Connect the ECG, temperature, and respiratory sensor cables and plug in the air warming tubing to the end of the animal holder

- Tape down the ECG/Temp cable outside of the holder to prevent the induced gradient noise
- Turn the isoflurane percentage to 0% on the Vetland vaporizer on the anesthesia cart
- Turn on the nonmagnetic oxygen tank under the anesthesia cart
- Check that the flow meter on the right side of the Vetland vaporizer is in the range of 0.25 to 0.5 LPM for a single mouse.
- Turn the isoflurane percentage to 2%
- Disconnect the gas tubing from the EZ vaporizer at the inlet of the animal holder
- Quickly slide the animal holder through the animal birdcage coil
- Confirm that the isoflurane exits the tubing and then connect the gas tubing at the quick connector of the animal holder from Vetland vaporizer
- Connect the tubing at the gas outlet of the animal holder to the scavenging filter
- Make certain that the ECG and respiratory signals look normal at the monitor next to the console
- Move the Vetland cart in the shielded room next to the bore
- Send the animal with the holder and coil into the magnet
- Turn off the water circulation system
- Turn off the oxygen tank against the fence
- Turn off the EZ vaporizer

- Confirm that the ECG signal is between 300 to 500 BPM (beats/min) and maintain body temperature above 29 degrees Celsius

## APPENDIX II

### Threshold Setting of Small Animal Gating System

We can right click the ECG waveform and the threshold setting window will pop up on the laptop. Then, we can change these threshold parameters to obtain the best-fit trigger for the ECG waveform. Because the diversity of animal activity provides different ECG waveforms, we need to set up these threshold parameters to best fit each animal.

There are several critical parameters to be addressed, including:

**R-Detect Blanking Period:** Manual choose \_\_\_\_\_ msec

The value is determined by the R-wave periods that we can set to be smaller but not too small; otherwise, a false trigger might occur quickly after the R-wave pulse. This procedure is very useful for the false trigger. If we detect a false R-wave, the system will not send out the trigger in the blanking period; therefore, we should set the value shorter than the ECG period. When the blanking period is off, the expected R-wave should come in soon and trigger the scanner.

### **Wave feature Detection**

Positive slope: \_\_\_ Samples = 6.7 ms, \_\_\_ uV minimum

Negative Slope: \_\_\_ Samples = 4.4 ms, \_\_\_ uV minimum

Let us assume we have the R-wave as a triangle signal. The positive slope corresponds to the ramp-up time we assign for the peak detection. We can input the number of samples in the positive and negative slopes that the software will transfer to the ramp-up time based on the sampling rate (6.7/4/4 ms). We should observe the R-wave on the graph and estimate the ramp-up time based on the grid span (10 or 100 ms per time grid based on the graph scale). If you have larger ramp-up time of the R-wave, you can assign larger sample points so that the software will not pick up the noise slope easily. The number of sample points should be different based on the different ECG waveforms from each animal.

We can follow same rule on the negative slope that observes the ramp-down time of R wave and assign the slope number. The system detects the R-wave from the positive slope and determines the trigger time on the end of the negative slope. The constant ramp-down time generally makes every trigger occur at the same R-wave amplitude. At the end of negative slope detection, the system will generate the trigger.

The amplitude should be addressed properly too because the baseline of the ECG is interfered with by movement, respiration, or any kind of vibration.

The trigger level should avoid the noise level but not be too large because the ECG signal might occasionally have small peaks or the baseline drops due to respiration.

## **Detection Threshold**

Auto: Maximum \_\_\_ uV

The maximum peak value should most definitely be larger than the R-wave amplitude.

Also, we need to set the detection threshold value larger than the R-wave.